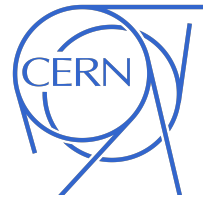




TECHNISCHE
UNIVERSITÄT
WIEN
Vienna University of Technology



DIPLOMARBEIT

Cherenkov Fibers for Beam Loss Monitoring at the CLIC Two Beam Module

Ausgeführt am Institut für
Atomphysik
der Technischen Universität Wien

Unter der Anleitung von
Univ. Prof. Dr. Christian Fabjan

und der Mitbetreuung von
Dr. Eva Barbara Holzer

durch

Jacobus Willem van Hoorne

Matrikelnummer: 0543017

Seepark HI 5/1 - 7121 - Weiden am See

CERN-THESIS-2012-112
28/06/2012



Wien, Juni 2012

Unterschrift des Studenten

Unterschrift des Betreuers

Acknowledgements

First and foremost I want to thank Prof. Chris Fabjan who, since my first stay at CERN in 2010, has not only been continuously supporting me, but also always encouraging me to take up greater challenges. Moreover, it were in particular his enthusiastic lectures that awakened my interest in particle physics and detectors.

Secondly, I have to thank my CERN supervisor Barbara Holzer for giving me the great opportunity to work with her on a very interesting subject. Her trust, and on the other hand the scrutinization of all the details of my work were of great help. Furthermore I want to specially thank Bernd Dehning for his advice and suggestions throughout my whole thesis. I also want to express my gratitude to Thibaut Lefevre for his support from the beginning and his many explanations on small details of CLIC.

I am indepted to all of my colleagues from the CERN BE-BI-BL section, but most of all to Sophie Mallows for her untiring help in many respects. Without her, this thesis would not have been possible in this extent. Other special thanks go to Ewald Effinger and William Vigano for their much appreciated help on electronics and all the other personal and professional issues discussed during the many coffee breaks. I want to thank Christoph Kurfürst for all his advice during the beam tests that helped to improve my setup.

Furthermore I want to thank the HEPHY BelleII SVD group, who let me participate in their beam time. In particular, I have to thank Annekathrin Frankenberger, who helped to improve my measurements with her cooling system.

Finally, major thanks go to my family and Marlene, who have have always supported and put their trust in me.

Abstract

The Compact Linear Collider (CLIC) study is a feasibility study aiming at a nominal center of mass energy of 3 TeV and is based on normal conducting travelling-wave accelerating structures, operating at very high field gradients of 100 MV/m. Such high fields require high peak power and hence a novel power source, the CLIC two beam system, has been developed, in which a high intensity, low energy drive beam (DB) supplies energy to a high energy, low intensity main beam (MB). At the Two Beam Modules (TBM), which compose the 2×21 km long CLIC main linac, a protection against beam losses resulting from badly controlled beams is necessary and particularly challenging, since the beam power of both main beam (14 MW) and drive beam (70 MW) is impressive. To avoid operational downtimes and severe damages to machine components, a general Machine Protection System (MPS) scheme has been developed. The Beam Loss Monitoring (BLM) system is a key element of the CLIC machine protection system. Its main role will be to detect potentially dangerous beam instabilities and prevent subsequent injection into the main beam linac and drive beam decelerators. In terms of cost and the required number of channels, Cherenkov fibers are a promising option for the BLM system along the CLIC main linac.

Cherenkov fibers are based on the idea of using optical fibers as a Cherenkov light radiator. After its production, a fraction of the Cherenkov light is trapped and guided to a photodetector at one end of the fiber by means of total reflection. This thesis presents a detailed study on the features of the technology of Cherenkov fibers and relates them to the requirements of the BLMs for the CLIC TBMs.

The work of pre-existing studies [28, 46, 48] was extended to an analytical model that provides a tool to calculate the number of photons reaching the photodetector and their propagation velocities along the fiber as a function of various properties of the fiber and the crossing particle.

Measurements to verify the model, using a multimode optical fiber irradiated at a high-momentum proton test beam have been carried out. Light yields as a function of fiber diameter, and the angle between the beam and the fiber axes are presented.

Using the Monte Carlo code FLUKA [3, 4], simulations on decisive beam loss scenarios for the CLIC TBM were performed. The simulated particle showers were used as an input for the developed model in order to study the sensitivity, the required dynamic range, the achievable longitudinal resolution of the loss location, and the ability to distinguish losses originating from either beam of the TBMs.

Finally the limitations on the attainable longitudinal resolution of the loss location with respect to multi-bunch trains as used in CLIC are discussed.

Kurzfassung

Die Compact Linear Collider (CLIC) Studie ist eine Machbarkeitsstudie zu einem Linearbeschleuniger mit einer nominellen Schwerpunkstenergie von 3 TeV, basierend auf normalleitenden Beschleunigungskavitäten, welche mit sehr hohen Feldgradienten von 100 MV/m operieren. Diese hohen Felder erfordern eine hohe Spitzenleistung, und daher wurde ein neues Energieversorgungskonzept, das CLIC Zwei-Beam-System, entwickelt, in dem ein hochintensiver Strahl mit geringer Teilchenenergie, der Drive-Beam (DB), Energie bereitstellt für den Main-Beam (MB), einen hochenergetischen Teilchentrahl mit geringer Intensität. Entlang der Zwei-Beam-Module (TBM), aus denen der 2×21 km lange Linearbeschleuniger zusammengesetzt ist, ist ein Schutz vor Strahlverlusten besonders notwendig und herausfordernd, da die Strahlleistung sowohl des Main-Beams (14 MW), als auch des Drive-Beams (70 MW) imposant ist. Um ernste Schäden an Maschinenkomponenten und Betriebsunterbrechungen zu vermeiden, wurde ein generelles Maschinenschutzsystem (MPS) entwickelt. Das Beam-Loss-Monitoring (BLM) System ist ein Schlüsselement dieses CLIC-Maschinenschutzsystems, dessen Hauptaufgabe es ist, potentiell gefährliche Strahlinstabilitäten zu erfassen und eine nachfolgende Injektion des Strahls in den MB-Linearbeschleuniger oder die DB-Entschleuniger zu vermeiden. Im Hinblick auf Kosten und die erforderliche Anzahl von Auslesekanälen stellen Cherenkov-Fiber eine vielversprechende Option für das BLM-System entlang des CLIC Linearbeschleunigers dar.

Cherenkov-Fiber basieren auf der Idee, optische Fiber als Cherenkovlicht-Radiatoren zu verwenden. Ein Teil des Cherenkovlichts bleibt nach seiner Entsehung in der Fiber enthalten und wird zu einem Photodetektor an einem Ende der Fiber geleitet. Diese Arbeit präsentiert eine detaillierte Studie zur Technologie von Cherenkov-Fibern und setzt diese in Relation zu den Anforderungen an das BLM System für die CLIC TBMs.

Die Arbeit von bereits existierenden Studien [28, 46, 48] wurde erweitert zu einem analytischen Modell. Dieses bietet ein Tool, die Anzahl der den Photodetektor erreichenden Photonen, in Abhängigkeit verschiedener Eigenschaften der Fiber und der geladenen Teilchen, zu berechnen. Weiters bietet es die Möglichkeit, die Ausbreitungsgeschwindigkeit jedes einzelnen, in die Fiber eingekoppelten, Photons zu berechnen.

Anhand von Messungen mit optischen Multimode-Fasern, welche in einem hochenergetischen Protonen-Teststrahl bestrahlt wurden, konnte das Modell verifiziert werden. Ergebnisse für die Lichtausbeute als Funktion des Faserdurchmessers und des Winkels zwischen dem Teilchenstrahl und der Achse der Faser werden vorgestellt.

Unter Verwendung des Monte-Carlo-Codes FLUKA [3, 4] wurden Simulationen für wichtige Strahlverlustszenarien an den CLIC-TBMs durchgeführt. Die simulierten Teilchenschauer wurden als Input für das entwickelte Modell verwendet um die Empfindlichkeit, den erforderlichen Dynamikbereich, die erzielbare longitudinale Auflösung des Verlustortes und die Möglichkeit, Verluste beider Strahlen an den TBMs zu unterscheiden, zu untersuchen.

Zuletzt wird die Limitierung der erzielbaren longitudinalen Auflösung des Verlustortes in Verbindung mit Multi-Bunch-Zügen, wie sie im CLIC verwendet werden, diskutiert.

Contents

1	Introduction	11
2	Beam Loss Monitoring	15
2.1	Loss Classes	15
2.2	Principles of Loss Detection	15
2.3	Considerations for the Selection of a BLM	16
3	CLIC - the Compact Linear Collider	19
3.1	CLIC Layout	21
3.2	Machine Protection System	23
3.2.1	Beam Power and Destructive Capacity	24
3.2.2	Failure Types	25
3.2.3	Protection Strategies	26
3.2.4	Operational Scenarios	27
3.3	Beam Loss Monitoring System for the TBM	27
3.3.1	System Sensitivity	28
3.3.2	Dynamic Range	28
3.3.3	Signal Resolution	29
3.3.4	Spatial Resolution	29
3.3.5	Temporal Resolution	30
3.3.6	Location Dependence	30
3.3.7	Radiation Hardness	30
3.3.8	Considered Technologies	31
3.4	CTF3 - the CLIC Test Facility	32
3.4.1	Two Beam Test Stand	32
3.4.2	Test Beam Line	32
4	Optical Fiber Waveguides and Photo Detectors	35
4.1	Optical Fiber Waveguides	35
4.1.1	Ray Theory	38
4.1.2	Attenuation	39
4.1.3	Dispersion	41
4.2	Radiation Effects in Optical Fibers	42
4.2.1	Radiation Hardness	44
4.3	Photo Detectors	48

4.3.1	Photo Multiplier Tube (PMT)	48
4.3.1.1	Main Characteristics	51
4.3.2	Silicon Photo Multiplier (SiPM)	52
4.3.2.1	Main Characteristics	55
5	Cherenkov Fibers	59
5.1	Cherenkov Effect	59
5.2	Cherenkov Effect in Optical Fibers	62
5.2.1	Model	63
5.2.1.1	Light yield	63
5.2.1.2	Trapping probability	63
5.2.1.3	Attenuation	70
5.2.1.4	Photon detection efficiency	71
5.2.1.5	Coupling efficiency	73
5.2.1.6	Fiber diameter dependency of light yield	73
5.2.1.7	Dispersion and photon propagation velocities	74
5.3	FLUKA Simulations	75
6	Verification Measurements	79
6.1	Angular Dependency of the Cherenkov Light Yield	79
6.1.1	First Beam Test	79
6.1.2	Second Beam Test	85
6.1.3	Results	88
6.2	Dependency of the Light Yield on the Fiber Diameter	89
6.2.1	Results	90
7	Cherenkov Fibers BLM for the CLIC Two Beam Modules	95
7.1	Considerations on the TBM Radiation Levels	98
7.2	Simulation of Beam Losses in the CLIC Two Beam Modules	98
7.2.1	Quantitative Determination of the Photon Yield	100
7.3	Longitudinal Resolution for Single-bunch Losses	106
7.4	Longitudinal Resolution for Multi-bunch Losses	112
8	Conclusion and Outlook	119
	Bibliography	121

1 Introduction

Most of the currently known phenomena of particle physics are described by the standard model of particle physics (SM), which has been developed since the second half of the last century. It comprises the unified theory of electroweak interaction and the theory of quantum chromodynamics [1] and thus describes three elementary forces - the electromagnetical force, the weak force, and the strong force. The fourth known elementary force - gravitation - is not described by the SM as its strength is many orders of magnitude smaller compared to the other three.

Within the SM, matter consists of fundamental fermionic particles - quarks and leptons. They are believed to be elementary and are all massive, however, the masses of neutrinos remain unknown. Both quarks and leptons are grouped into three 'families' or 'generations'. Although searches for a fourth generation are ongoing, experimental results on the width of the Z^0 -resonance from LEP indicate that there are exactly three generations of neutrinos and therefore generations of fermions [1]. A list of the fermions and their properties is given Table 1.1. To all fermions there exist corresponding anti-fermions with equal mass, but opposite electrical, weak or color charge.

	Generation			el. charge	color	weak isospin
	1	2	3			
Leptons	ν_e	ν_μ	ν_τ	0	-	1/2
	e	μ	τ	-1		
Quarks	u	c	t	+2/3	r, g, b	1/2
	d	s	b	-1/3		

Table 1.1: List of leptons and quarks with their properties. The electrical charge is given in terms of the elementary charge ($1.602 \cdot 10^{-19}$ C) [1].

The fundamental forces described by the SM are all mediated via the exchange of force carrier particles - vector gauge bosons - of which a list is given in Table 1.2. While the photon does not carry the charge of the electromagnetic force, the W/Z bosons carry weak charge and the gluons carry color charge and therefore, they each also couple to each other. Each interaction can be described by the corresponding Feynman diagram, in which energy, momentum, angular momentum, electric charge, color, the number of baryons (i.e. three quark bound states) and the number of leptons is conserved [1].

Force	Particle(s)	Name	Charge	Mass
Electromagnetical	γ	Photon	electric	0
Strong	g	Gluon	color	0
Weak	W^\pm, Z^0	W/Z Boson	weak	$\simeq 100$ GeV

Table 1.2: A list of the three fundamental forces with the exchange particles and their properties. The exact masses of the W^\pm, Z^0 bosons are 80.42 and 91.18 GeV, respectively [1].

In the 20th century the standard model has seen great success in explaining the behaviour of the fundamental forces and in predicting new particles. This success can be emphasized by the prediction of a third generation of quarks in 1973 by Kobayashi and Maskawa and the subsequent discoveries of the b and t quark in 1977 and 1995, respectively. One major problem within the SM, however, is the origin of masses. The pure gauge theory of the electroweak interactions does not allow mass terms. The SM-solution to this problem is electroweak symmetry breaking, which introduces the Higgs field that generates the particle masses via its coupling.

Despite the great success of the SM, it is evident that a more fundamental theory must exist. For example, astrophysical observations show that the matter described by the SM sums only up to about 5% of the total energy content of the universe. Of the rest of the energy in the universe, approximately a quarter is attributed to dark matter, the remaining part is attributed to dark energy, yet for both the SM provides no candidate. Further hints on the incompleteness are given by theoretical issues associated with the explanation of the observed particle masses and their hierarchy.

With the startup of the Large Hadron Collider (LHC) at CERN, experimental particle physics has started to explore new energy regions. The Higgs boson - the fluctuation of the Higgs field - should, if it exists, be within reach of the LHC. Also popular extensions of the SM, like supersymmetry (SUSY), are likely to show evidence. But whatever will be observed at the LHC, the precision of the measurements of a hadron collider is intrinsically limited due to the fact that the colliding particles are not elementary. Which of the constituents of the protons - quarks and gluons - will interact cannot be controlled.

An electron-positron collider would allow collisions with well defined initial states. Technologically, an electron-positron collider which exceeds previously reached energies has to be constructed as a linear accelerator. The most powerful linear collider currently under development is CLIC - the Compact Linear Collider. It aims at a nominal center of mass energy of 3 TeV and is based on normal conducting traveling-wave accelerating structures, operating at very high electric field gradients of 100 MV/m. Such high fields require high peak power and hence a novel power source, the CLIC two beam system, in which a high intensity, low energy drive beam supplies energy to a high energy, low intensity main beam, has been developed.

At the Two-Beam Modules (TBM), which compose the 2×21 km long CLIC main linac, a protection against beam losses resulting from badly controlled beams is necessary and

particularly challenging and important, since the beam power of both main beam (14 MW) and drive beam (70 MW) is impressive. Therefore, in order to ensure safe beam operation, to avoid operational downtimes and to avoid severe damages, a general machine protection system (MPS) scheme has been developed. The beam loss monitoring (BLM) system is a key element of the CLIC machine protection system.

In the CLIC conceptual design report (CDR) [9], ionization chambers, similar to the ones used for BLM at the LHC, are specified as the baseline choice of BLM system for the CLIC TBMs. However, the total number of such localized BLMs required is currently estimated to be in the range of 50.000. To reduce the number of channels and the cost, alternative technologies are investigated. Within this context, BLMs with a linear, extended sensor that is spanned in parallel to the beam lines are promising candidates.

This work focusses on the option of the technology of Cherenkov fibers, which is based on the idea of using optical fibers, placed in parallel to the accelerator, as a Cherenkov light radiator. After its production, a fraction of the Cherenkov light is trapped and guided to a photodetector at one end of the fiber by means of total reflection.

Chapter 2 gives an introduction to the principles of beam loss detection and explains the necessity of BLMs as part of the accelerator MPS. Furthermore, general aspects on the design of a BLM system are presented.

Chapter 3 is an introduction to the Compact Linear Collider study. Besides the basic ideas of the CLIC layout, the CLIC Machine Protection System and the requirements on the Beam Loss Monitoring system for the CLIC Two Beam Modules, as in particular the radiation hardness, sensitivity, dynamic range, and the achievable spatial resolution are explained in detail.

Chapter 4 discusses the principles of the main parts of a Cherenkov fiber BLM: the optical fiber as the Cherenkov radiator and the photodetector. For fibers, among an explanation of the possibilities to describe the propagation of light within an optical waveguide, the focus is laid on radiation effects and resistivity. Regarding the photodetectors, classical Photo Multiplier Tubes (PMT) are compared to the relatively new type of Silicon Photomultipliers (SiPM).

Chapter 5 describes the Cherenkov effect in optical fibers and is devoted to the development of an analytical model that provides a tool to calculate the Cherenkov light signal in a fiber for any simulated particle shower. Among the number of photons reaching the photodetector, also their propagation velocities along the fiber can be calculated as a function of various properties of the fiber and the crossing particles. The results of the model related to the dependency of the light yield on the angle between the beam and the fiber axis are presented and compared to results of dedicated FLUKA [3, 4] simulations.

Chapter 6 presents measurements for the verification of the developed model using a multimode optical fiber irradiated at a high-momentum proton test beam. The results on the Cherenkov light yield as a function of fiber diameter, and the angle between the beam and

the fiber axes are shown.

In Chapter 7, the considerations and results from the previous chapters are related to the specifics and requirements of the CLIC TBMs. After a discussion of the impact of the radiation levels in the CLIC tunnel on the practical use of Cherenkov fibers, simulations on decisive beam loss scenarios using the Monte Carlo code FLUKA are presented. The resulting simulated particle showers are used as an input for the developed model in order to study the sensitivity, the required dynamic range, the achievable longitudinal resolution of the loss location, and the ability to distinguish losses originating from either beam of the TBM. Finally the limitations on the attainable longitudinal resolution of the loss location with respect to multi-bunch trains as used in CLIC are discussed.

In the last Chapter, the conclusions of this work are stated.

2 Beam Loss Monitoring

Beam loss monitors (BLM) are an important part of the machine protection systems of particle accelerators and are used to minimise losses to protect the environment and equipment of the accelerator from radiation damage. Furthermore they can serve as a sensitive tool for beam diagnostics, i.e. the localisation and study of the kind of losses.

A detailed understanding of the beam loss mechanisms and the related processes which make a beam loss detectable by monitors are crucial. The type and design of the monitor used has always to be adjusted according to the specific requirements of the machine it has to protect. A general introduction to beam loss monitoring can be found in [2].

2.1 Loss Classes

Beam losses can be divided into two different classes:

1. Irregular, uncontrolled beam losses with a fast rise time.

Beam losses with fast rise times are mainly the result of a misaligned beam or a defect in the accelerator components. Examples are trips of the radio frequency (RF) cavities or fast vacuum deterioration. These losses have to be kept below a certain level by the machine protection system (MPS) to avoid serious damage of machine components. However, sometimes irregular losses have to be tolerated even at high levels during machine studies or commissioning. Post mortem analysis of loss events is helpful to understand the failure conditions.

2. Regular, controlled beam losses with a slow rise time.

Regular losses are typically not avoidable. They might occur continuously during operation and limit the transport efficiency of the beam. Examples are residual gas scattering, instabilities, beam-beam interactions, etc. These losses have to be kept below a certain level by to keep activation low enough for hands-on maintenance, or environmental protection.

2.2 Principles of Loss Detection

A typical BLM is mounted outside the vacuum chamber. As a result, the monitor observes the shower caused by the lost particles interacting with the material of the vacuum chamber walls or of the magnets and other machine components. In case of a beam loss, a BLM would ideally establish the number of lost particles in a certain position and time interval.

Therefore, the signal from the BLM should be proportional to the number of lost particles. This proportionality (or efficiency ϵ) in terms of signal/lost particle depends on the type of BLM, the position of the BLM with respect to the beam, the exact loss position and impact angle, the type of the lost particles, and the intervening materials. Moreover, it depends on the momentum of the lost particles, which may vary by a large ratio during the acceleration cycle. In general, it is hard to measure or to calculate the exact efficiency of BLMs around an accelerator. Therefore, the usual way of calibration and defining the overall efficiency ϵ is to use Monte Carlo codes such as FLUKA [3, 4] or Geant 4. With the help of these codes, the particle loss at a particular location can be simulated based on the complete geometry of the beam line components near the BLM, as well as the corresponding magnetic and electrical fields of the accelerator and the BLM itself. The amount of beam loss at a certain location is then defined as

$$N = \frac{S}{\epsilon} \quad (2.1)$$

where N is the number of lost particles, S the BLM signal and ϵ is the BLM efficiency. Finally, for machine protection tasks, the number of lost particles must be put in perspective with certain thresholds representing loss levels that are dangerous for the machine.

The most common method to observe the interaction of charged particles with the sensitive detector medium is to measure:

- Ionization charge,
- Secondary emission current,
- Fluorescence light or
- Cherenkov light.

2.3 Considerations for the Selection of a BLM

There are two main aspects, which have to be considered for the design of a beam loss monitor system [2]:

1. Type of loss monitor.

Typical beam loss monitors detect beam losses by measurement of secondary ionizing radiation produced by lost beam in real-time. The specification for acceptable beam losses and the minimum required sensitivity defines the dynamic range of the BLMs for the protection tasks. Additional sensitivity combined with a larger dynamic range extends the utilization of BLM systems for diagnostic purposes. Furthermore, it has to be sufficiently radiation hard in order to be suitable for the accelerator environment. Besides the ability to determine the amount of lost beam, it would ideally also resolve the time structure of the loss and its spatial distribution.

For electron accelerators, the produced secondary radiation consists mainly of electromagnetic particles (electron-, positron- and gamma- shower). The ionizing capability of the charged shower particles is utilized as the signal source of beam loss monitors.

As a summary, the consideration of the following parameters is important to design an appropriate monitor type for a particular beam loss application:

- Cost - incl. electronics channels
- Radiation hardness - material
- Sensitivity
- Dynamic range
- Temporal resolution (\leftrightarrow longitudinal resolution)
- Spatial resolution
- Signal resolution (magnitude)
- Physical size - positioning
- Reliability, maintainability, robustness
- Type of output - current or pulse
- Signal source
- Ease of calibration - online calibration
- System end-to-end online tests
- Uniformity of calibration - unit to unit
- Calibration drift due to aging, radiation damage, outgassing, etc.
- Ability to distinguish from unwanted radiation - e.g. synchrotron radiation
- Spatial uniformity of coverage - e.g. in long tunnel, directionality
- Instantaneous dynamic range vs. switched gain dynamic range
- Response to excessively high radiation levels

Due to this long list of considerations many different types of loss monitors exist, each having their own advantages and disadvantages. Common options for beam loss monitors include:

- Short and long ionization chambers
- Photomultipliers with scintillators or Cherenkov radiators - including optical fibers
- PIN Diodes
- Secondary emission multiplier-tubes
- Microcalorimeters
- Compton Diodes

2. Positioning of the Loss Monitor.

The loss of a high-energy particle in the wall of a beam pipe results in a shower of particles. The signal of a loss detector will be the highest, if it is located at the maximum

of the shower. Monte Carlo simulations can be used to find the optimum locations for the monitors, as well as to calibrate the monitors in terms of lost particles/signal at the given location.

The spatial distribution of the shower depends on the energy of the lost particle and on the geometry of the beam line components. Therefore, the spatial distribution of lost particles has to be studied in advance to place the monitors at the right position. Moreover, this means, that an understanding of the loss mechanism and dynamics in the accelerator is necessary to predict the typical positions of losses. Due to the many different possible scenarios for beam losses, commonly generic cases have to be defined for the simulations.

3 CLIC - the Compact Linear Collider

The powerful particle accelerator to date, the Large Hadron Collider (LHC) [5] at CERN, is built to provide an extensive programme of physics at a new high-energy frontier over the coming years. Since the first collisions in 2010, the LHC has been probing a new, unmatched energy region. Thereby, it should above all confirm or refute the existence of the Higgs boson of the Standard Model of particle physics (SM) and will explore the possibilities for physics beyond the Standard Model (BSM), such as supersymmetry (SUSY), extra dimensions and new gauge bosons. The discovery potential is large and will set the direction for possible future high-energy colliders. Nevertheless what will be observed at the LHC, the precision of the measurements at a hadron collider is intrinsically limited due to the fact that the colliding particles - protons - are not elementary. Which of the constituents of the colliding protons - quarks or gluons - will eventually interact cannot be controlled. A lepton collider would allow collisions with well defined initial states.

The highest centre-of-mass energy in electron-positron collisions so far – 209 GeV – was reached at the Large Electron Positron collider (LEP) [6] at CERN. In a circular collider, such as LEP, the energy is limited by synchrotron radiation. The energy radiated per turn, ΔE_{sync} , scales with the radius R , the particle rest mass m_0 and the particle energy E

$$\Delta E_{sync} \propto \frac{E^4}{R \cdot m_0^4} \quad (3.1)$$

ΔE_{sync} increases with the fourth power of the energy of the circulating beam. The energy lost in this way needs to be replaced by a powerful RF acceleration system. In LEP, for example, each beam lost about 3 % of its energy on each turn and the biggest superconducting RF system built so far was just enough to keep the beam at its nominal energy. Therefore, a storage ring is not an option for an e^+e^- collider operating at an energy significantly above that of LEP, as the amount of RF power required to keep the beam circulating becomes prohibitive. Two alternatives are being explored:

1. The use of muons which have a mass 207 times larger than electrons.

The feasibility of muon colliders is being studied and critical challenges addressed. In particular, those are the limited muon lifetime (2 ms in the laboratory frame) and their production in large emittances, requiring novel cooling methods.

2. The use of e^+e^- linear colliders to avoid the bending of particle trajectories.

Their basic principle is that two linear accelerators face each other, one accelerating electrons, the other positrons and the two beams of particles collide head on.

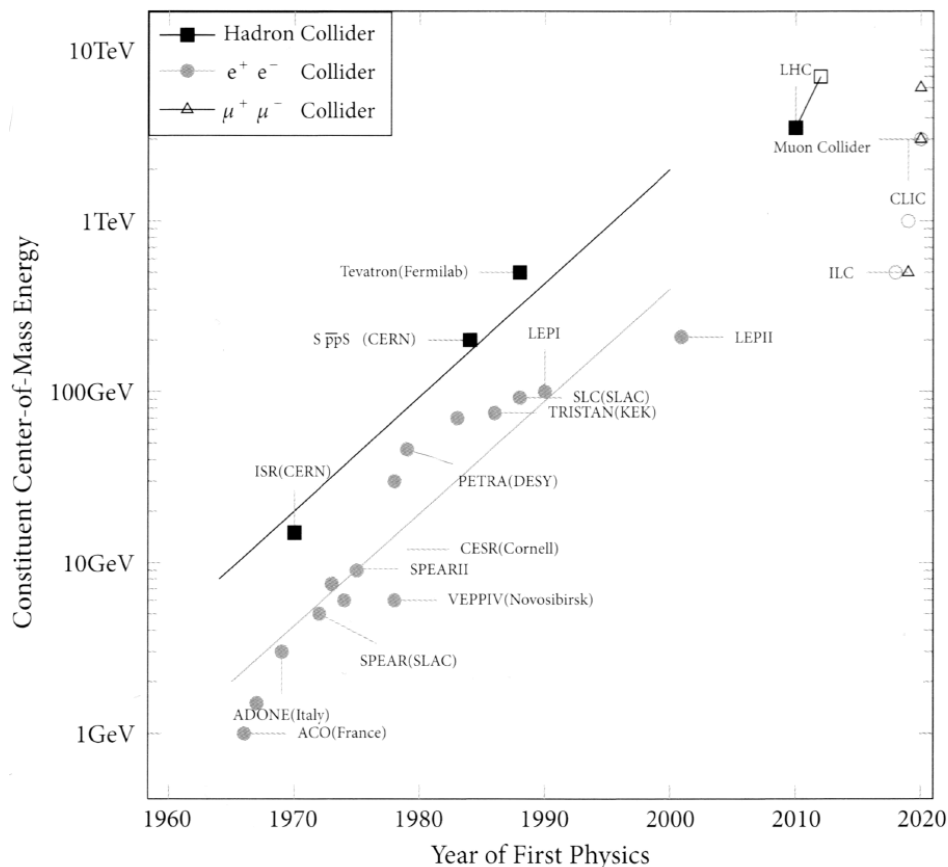


Figure 3.1: Livingston plot in constituent center-of-mass energy, $q\bar{q}$, qq , or ee [7].

Linear colliders are therefore the only option for realizing electron–positron collisions at tera-electron-volt energies. The inherent features of this scheme influence the design in twofold: First, the linacs have to accelerate the particles in one single pass. As a result high electric fields for acceleration are required to keep the length of the collider within reasonable limits. Such high fields can be achieved only in pulsed operation.

Secondly, after acceleration, the two beams collide only once. In a storage ring, the beams collide with a high repetition frequency, in the case of LEP at 44 kHz. In contrast, a linear collider would only have a repetition frequency of typically 5–100 Hz. This means that the luminosity that is necessary for the particle physics experiments can only be reached by very small beam dimensions at the interaction point and with the highest possible bunch charge.

Currently, two different technologies for linear colliders are under development, each with a different energy range:

- The International Linear Collider (ILC) [8] collaboration is studying a machine with a center-of-mass energy of 500 GeV and a possible future upgrade to 1 TeV. This study is based on an RF system using superconducting cavities for acceleration, with a nominal accelerating field of 31.5 MV/m and a total length of 31 km for a colliding-beam energy of 500 GeV. Since superconducting technology is fundamentally limited with regard to achievable gradients, a higher energy is not achievable over distances of this scale.

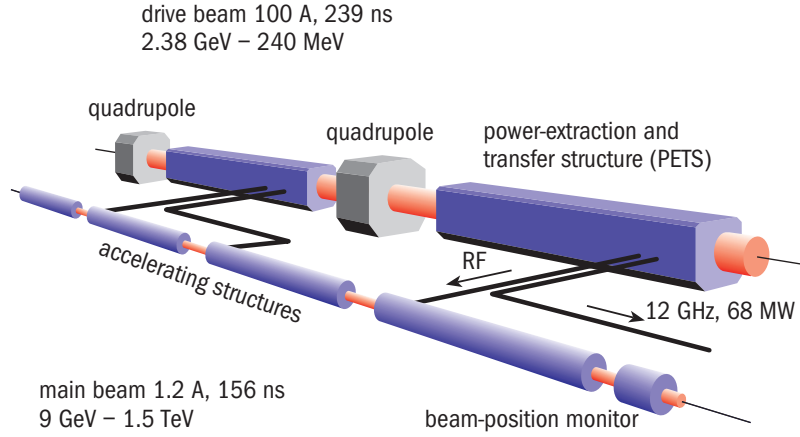


Figure 3.2: The CLIC two-beam scheme. The main beam is accelerated by energy provided from the lower energy, high intensity drive beam [10].

- The Compact Linear Collider (CLIC) [9] is a study for an e^+e^- linear collider with a nominal center of mass energy of 3 TeV, and foresees building CLIC in stages, starting at the lowest energy required by physics, with successive energy upgrades. The CLIC scheme is based on normal conducting travelling-wave accelerating structures, operating at very high electric fields of 100 MV/m to keep the total length to about 48 km for a colliding-beam energy of 3 TeV. Such high fields require high peak power. Hence, a novel power source, the CLIC two-beam system, in which a drive beam supplies energy to the main accelerating beam has been developed (see Figure 3.2).

Figure 3.1 helps to classify the future linear colliders in the view of accelerator history. It presents a so called Livingston plot, in which the center-of-mass energy of the fundamental constituents - electrons and quarks - is plotted against the year of first physics of the according accelerator. Like its relative, Moore's law in semiconductor technology for the number of transistors on a chip, the achievements in constituent energy are approximately exponential in time, with continual predictions over decades that this rate cannot be maintained for long [7].

3.1 CLIC Layout

As mentioned before, the key feature of CLIC acceleration method is the two-beam scheme to produce and distribute the high peak RF-power. The proposed CLIC layout is presented in Figure 3.3. The overall CLIC parameters as denoted in the conceptual design report (CDR), are given in Table 3.3. The tunnel for CLIC will contain the elements for both the main beam and the drive beam running parallel to each other about 65 cm apart. Transfer lines to transport both beams from the injectors to the far ends of the two linacs can be installed in the same tunnel under the ceiling.

Drive Beam. The drive beam is generated and accelerated by conventional high-power

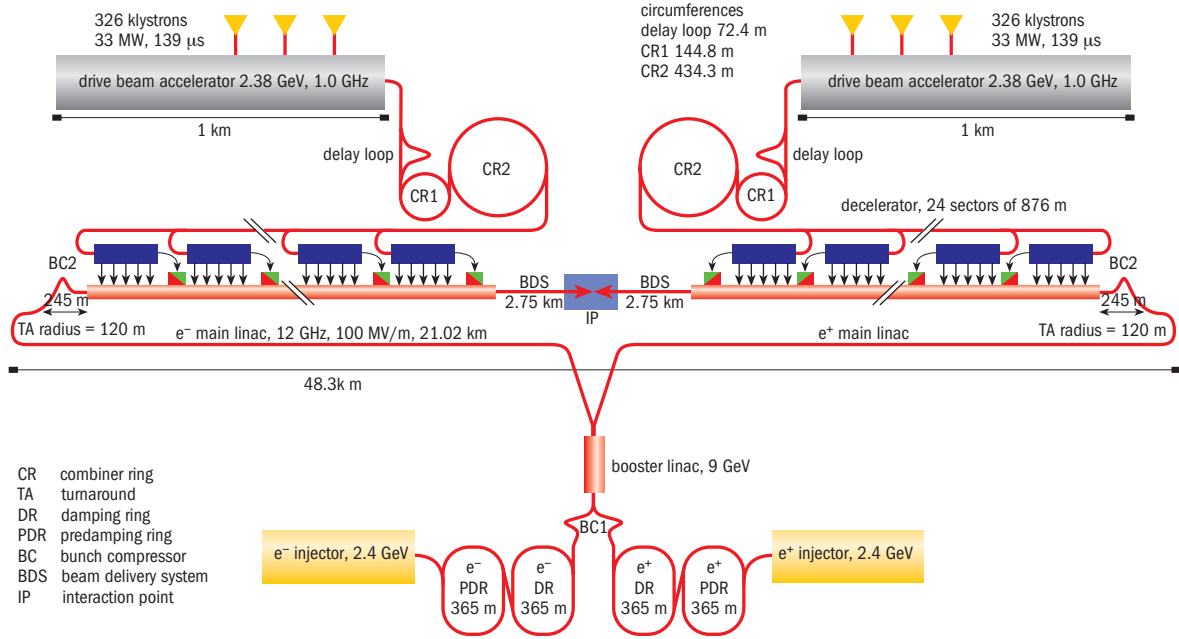


Figure 3.3: The proposed layout for CLIC, showing the various components of the injection system and the drive-beam system [10] .

klystrons to the energy of 2.4 GeV at the frequency of 0.5 GHz. After the acceleration, the particle bunches of the drive beam are recombined using a delay loop (combination factor 2) and two combiner rings (CR1 and CR2, with combination factors 3 and 4, respectively), resulting in total combination factor of 24 and hence the final frequency of 12 GHz. The current of the drive beam is ≈ 4 A before and ≈ 100 A after the recombination.

PETS and main linac. After the recombination scheme the drive beam is lead to 24 decelerator modules. To transfer the energy to the main beam, the drive beam passes through so-called power extraction and transfer structures (PETS), where the kinetic energy of the beam is transformed to electromagnetic (RF) energy with an efficiency of $\approx 84\%$. This RF energy is extracted from the PETS and sent via waveguides to the accelerating structures (AS) in the parallel main beam.

To achieve the luminosity required the experiments, beams of extremely small emittance are needed. Therefore, at CLIC two damping rings in succession (PDR, DR) will provide the necessary reduction in each of the main beams. Finally, a sophisticated beam delivery system (BDS) focusses the beam down to dimensions of 1 nm rms size in the vertical plane and 40 nm horizontally.

Two beam modules. The CLIC two-beam configuration along most of the length of the main and drive linacs consists of repeated 'modules', referred to as the two beam modules (TBM). Each main linac contains more than 10.000 such modules. The drive beam, running parallel to the main linac, regularly powers two main beam accelerating structures (AS) from one power extraction and transfer structure. Each module contains up to four PETS, each

Center of Mass Energy	500 GeV	3 TeV
Total luminosity	$2.3 \cdot 10^{34}$	$5.9 \cdot 10^{34}$
Total site length [km]	13.0	48.3
Loaded accel. gradient [MV/m]	80	100
Main linac RF frequency [GHz]	12	12
Beam power/beam [MW]	4.9	14
Bunch charge [$10^9 e^+ / e^-$]	6.8	3.72
Bunch separation [ns]	0.5	0.5
Bunch length [μs]	74	44
Beam pulse (train) duration [ns]	177	156
Repetition rate [Hz]	50	50
Hor./vert. norm. emitt. [$10^{-6} / 10^{-9}$]	4.8/25	0.66/20
Hor./vert. IP beam size [nm]	202/2.3	40/1
Wall-plug-to-beam transfer efficiency	4.1%	5.0%
Total power consumption [MW]	240	560

Table 3.1: CLIC main parameters. [9]

feeding two accelerating structures, and two drive-beam quadrupoles to ensure the low-energy drive beam remains focussed. Space for quadrupoles in the main linac is made by leaving out two, four, six or eight accelerating structures and suppressing the corresponding PETS (see Figure 3.4). Five types of module are needed. Module Type-0 contains only accelerating structures in the main beam line whereas module Type-1 to Type-4 have main beam quadrupoles of variable length, replacing from 2 to 8 accelerating structures (see Figure 3.4).

Interaction point and detectors. CLIC is designed to have two detectors sharing a single collision point. The detectors will be moved several times in a year using a so-called push-pull system. The International Large Detector (ILD) and Silicon Detector (SiD), originally developed for ILC, are basis for the detectors proposed for CLIC. The CLIC ILD concept is based on a time projection chamber (TPC), which provides a highly redundant continuous tracking with relatively little material in the tracking volume itself. The CLIC SiD concept has a compact all-silicon tracking system, which has the advantage of fast charge collection. Both concepts have barrel calorimeters and tracking detectors located inside a superconducting solenoid. The particle energy measurement is performed by electromagnetic silicon-tungsten sampling calorimeters and highly granular hadronic sampling calorimeters.

3.2 Machine Protection System

A comprehensive explanation of the CLIC machine protection system can be found in the CLIC CDR [9] and in [11]. However, due to its importance as the framework for the BLM system, it is summarized in this section.

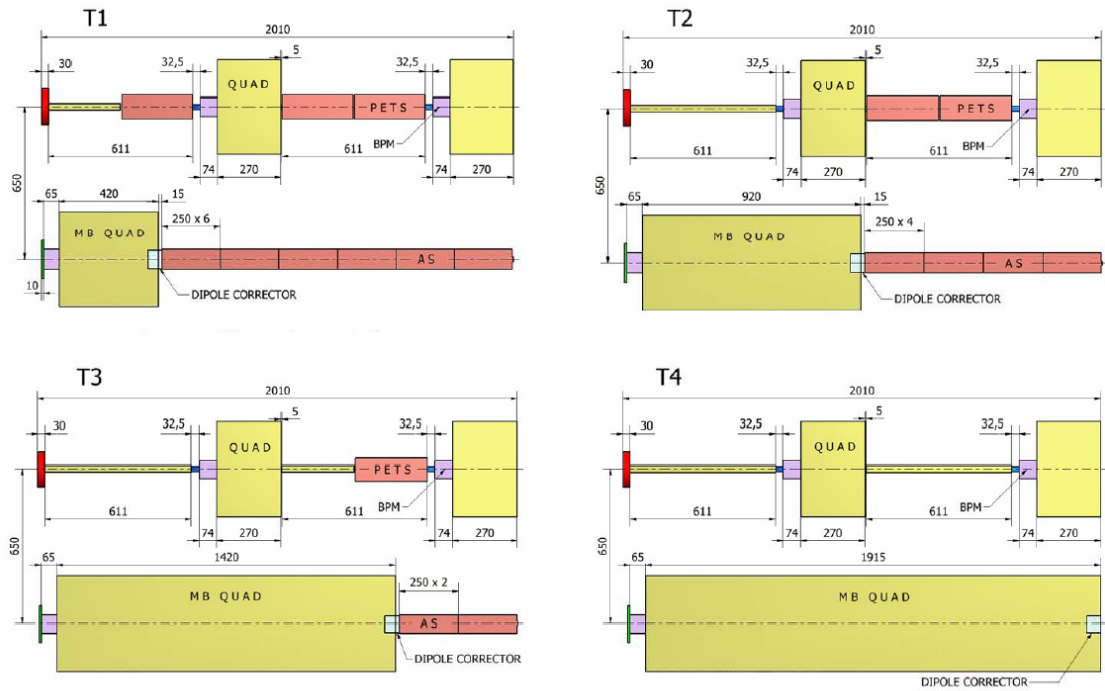


Figure 3.4: Schematic layout of the CLIC modules with main quadrupole. T1 - type 1 module, T2 - type 2 module, T3 - type 3 module, T4 - type 4 module; [10]

In CLIC, machine protection has to cope with a wide variety of failures, from real-time failures (RF breakdowns, kicker misfiring), to slow equipment failures, to beam instabilities. The machine protection has to protect the various machine components from damage caused by badly controlled beams. Therefore, it should reduce the damage risk to a level where the risk becomes acceptable. For CLIC, a risk is regarded as acceptable if the total expected operational downtime from all risks terms is smaller than a few percent. Likewise, the total expected financial impact should be less than a few percent of the operational cost.

3.2.1 Beam Power and Destructive Capacity

The beam power is given by the product of the beam charge, the particle energy and the cycle repetition rate (50 - 100 Hz). It is large both for the drive beam (70 MW) and the main beam (14 MW). However, for the definition of a "safe beam", the destructive potential is primarily determined by the charge density of the beams. Table 3.2 lists the beam characteristics for different sections of the TBM. The energy density in copper due to direct ionization loss by the incident beam particles and the shower core particles is noted. These numbers must be related to the level of structural yield in copper (60 J g^{-1}). Hence, as presented in the last column of Table 3.2, the drive beam is two orders of magnitude above safe beam, while the main beam is up to four orders of magnitude above safe beam.

Beam	Particle Energy [GeV]	Pulse Charge [μC]	Beam Size [mm^2]	Energy Density in copper [J g^{-1}]		Damage Potential
				Incident Beam	Shower Core	Incident Beam
DBT	2.4	25	1	$3.4 \cdot 10^3$	40	$0.8 \cdot 10^2$
MB-DR	2.8	0.20	$125 \cdot 10^{-6}$	$1.8 \cdot 10^5$	0.34	$0.5 \cdot 10^4$
MB- βcoll	$1.5 \cdot 10^3$	0.18	$40 \cdot 10^{-6}$	$6.7 \cdot 10^5$	120	$1.5 \cdot 10^4$

Table 3.2: CLIC TBM beam characteristics and energy density [11] for a single drive beam train (DBT), the main beam at the extraction of the damping rings (MB-DR) and the main beam at the betatron collimation section (MB- βcoll).

3.2.2 Failure Types

According to their nature, the following types of failure can be distinguished in CLIC:

1. Fast failures

These failures occur at time scales corresponding to the beam passage through the accelerator complex. In particular in the main linac, it may be impossible to detect a failure and dump the beam. The major sources of these fast failures are:

- RF breakdown. An RF breakdown could potentially produce enough transversal kick to send the drive beam or the main beam off trajectory into some accelerator component.
- Kicker misfiring. A misfiring of a kicker can send the beam off trajectory into the extraction channel.
- Klystron trip. A klystron trip in the drive beam linac may potentially disrupt the beam sufficiently to cause large losses.

2. Inter-cycle failures

These are mainly equipment failures that happen in the interval between two successive machine cycles (10-20 ms). The major sources of equipment failures are:

- Power supply failures
- Positioning system failures
- Vacuum system failures

3. Slow failures

These are failures that develop at time scales larger than the repetition rate of CLIC. They cause a slow onset of losses due to drifts in temperature, misalignment or beam feedback saturations. Under normal conditions, the beam feedback system should keep these drifts under control.

Machine sub-systems	E_{beam} [GeV]	e^-/train	τ_{train}	$N_{e^-, \text{dam}}$	$N_{e^-, 1W/m}$ [$m^{-1}s^{-1}$]
Main Beam					
e^- and e^+ injector complex	0-2.86	1.16E+12	156ns		2.18E+09 (at 2.86GeV)
Pre-Damping and Damping Rings	2.86	1.16E+12	156ns	3.48E+08 (at extraction)	2.18E+09
RTML	9	1.16E+12	156ns		6.94E+08
Main Linac	9-1500	1.16E+12	156ns	3.48E+08	6.94E+10 - 4.16E+06
Beam Delivery System	1500	1.16E+12	156ns	1.16E+08	4.16E+06
Drive Beam					
Injector complex	0-2.4		140 μ s	1.54E+13	2.60E+09 (at 2.4GeV)
Decelerator	2.4-0.24	1.53E+14	240ns	1.54E+12	2.60E+09 -2.60E+08
Dump lines	0.25 (peak)	1.53E+14	240ns	1.54E+12	2.60E+08

Table 3.3: Beam parameters and loss limits in the CLIC Complex [9]. The listed parameters are the beam energy, E_{beam} , the number of electrons per train, e^-/train , the bunch train duration, τ_{train} , the estimated number of electrons to damage beam line components, $N_{e^-, \text{dam}}$, and the number of electrons for a loss of 1 Watt per meter $N_{e^-, 1W/m}$.

3.2.3 Protection Strategies

The machine protection of CLIC consists of various strategies to deal with each type of failure.

- **Passive protection**

In case of fast failures, for which the detection and beam abort is impossible, the protection will be based on passive protection in the form of masks and spoilers. The passive protection must be made robust enough to provide full protection for the whole bunch train.

- **Real-time protection**

In cases where the geometry of the CLIC complex provides the possibility to take a short-cut in the signal path, a protection in real-time is considered.

- **Beam interlock system**

In case of an equipment failure during an inter-cycle period, a beam interlock system (BIS) will assure that the next cycle is inhibited. The BIS will handle all failures up to 2 ms before the next cycle is set off.

- **Safe by design**

To cover the 2 ms blind period prior to each cycle, all magnet circuits in critical beam transport structures must have enough inertia to remain within tolerance for 2 ms after a power converter fault. The same principle must be applied to all active equipment: vacuum, positioning systems, RF-HV, kicker-HV and beam instrumentation.

- **Next cycle permit**

The repetition rate of CLIC allows for nearly 10 ms to analyse the performance of a cycle and to decide whether it is safe to commit the machine for the next cycle. After every cycle the next cycle permit is systematically revoked and is then only re-established if a predefined list of beam and equipment quality checks has passed.

Although the results of all beam observation systems will be surveyed, the main responsibility falls on the BLM system, which is discussed in the next section.

3.2.4 Operational Scenarios

Safe operation of CLIC requires that potentially harmful beam must not be allowed into the machine. At a start-up, i.e. when the machine conditions are unknown, only a pilot beam that is less likely to cause structural damage to the accelerators components is safe. Once the machine is probed by such a safe pilot beam, the charge density of the beam can be increased in steps by the beam control system, as long as allowed by the post cycle analysis of every pervious step.

3.3 Beam Loss Monitoring System for the TBM

The beam loss monitoring (BLM) system is a key element of the CLIC machine protection scheme. A comprehensive discussion of the required features can be found in the CLIC conceptual design report (CDR) [9]. The primary role of the system is to detect potentially dangerous beam instabilities and prevent subsequent injection into the main beam linac (MB) and the drive beam decelerators (DB). Its secondary role, as an important part of beam diagnostics, is to localize and characterize the beam loss distribution. This includes the ability to measure the time structure of the losses, which would indicate the origin of beam perturbations. In principle, these two roles could be decoupled and represented by two different systems, however, one system that provides both protection and diagnostics is preferable.

The CLIC elements that have to be protected from beam losses are:

- the predamping rings,

- the damping rings, with their superconducting undulators which should be protected from quenching,
- the bunch compressors,
- the transfer lines, in particular the turnarounds,
- the combiner rings,
- the drive beam accelerator,
- the beam delivery system,
- and the two-beam modules.

At the two-beam modules, the protection from beam losses is particularly challenging and important. Beam losses on either side of the TBM can have catastrophic consequences for the machine [12], due to the high intensity (drive beam) or high energy and small emittance (main beam). In the following, the requirements for the beam loss system in terms of detector sensitivity, response time, position resolution, dynamic range and ability to distinguish losses originating from various sources are discussed.

3.3.1 System Sensitivity

Ideally, the system sensitivity allows for a detection of standard losses during normal operation. In CLIC, the largest part of operational losses is expected to originate from beam-gas interactions [12]. On the other hand, it is required that the system is at least sensitive to the losses at which the machine can no longer operate in stable conditions. It is assumed from beam dynamics considerations that

- losses of more than 10^{-3} of the total beam intensity along the 21 km main linac, and
- more than 10^{-3} of the total beam intensity along each DB decelerator section (876 m),

will lead to luminosity losses due to beam loading variations. In order to detect the onset of such losses, the sensitivity requirements are specified to be the signal resulting from a loss of a factor 10 less.

3.3.2 Dynamic Range

The BLMs should be sensitive to signals from lost electrons with an energy range of 9 to 1500 GeV in the main beam, and 2.4 to 0.24 GeV in the drive beam. The upper limit of the dynamic range of the system should allow the detection of the signal corresponding to an onset of dangerous beam losses. Dangerous losses are defined as those which can cause damage to accelerator elements. As previously discussed, beam losses become destructive at the TBM at the level where approximately

- 1 % of the DB or

- 0.01 % of the MB

hits a single aperture restriction. To limit the required dynamic range of the BLMs, the upper end of the dynamic range can be defined as 10 % of the signal produced by a destructive loss.

From the results of simulations using the Monte Carlo code FLUKA [3, 4] to calculate the absorbed doses near the beam lines due to destructive loss scenarios [12], the dynamic range of the system was estimated to be in the range of 10^5 - 10^6 .

3.3.3 Signal Resolution

The required signal resolution is derived from the maximum allowed down time due to false triggers [12].

For this, it is assumed that every false trigger of injection inhibit will lead to about 10 seconds dead-time for the validation of the intensity-ramp procedure of the beam protection system. The dead time due to false triggers should be limited to 0.1 % in order not to affect the operational availability. Hence, false triggers should occur less than once per 10^4 seconds (~ 8.6 times per day). At 50 Hz this corresponds to a false trigger probability of $2 \cdot 10^{-6}$ per cycle. To achieve such a level of system performance, the individual BLM false triggers rate should be about the number of individual BLM channels times lower. In case of Cherenkov fibers of 100 m length, there would be ~ 500 channels, i.e. the signal resolution has to allow for a false trigger probability less than $4 \cdot 10^{-9}$ per cycle for an individual channel.

3.3.4 Spatial Resolution

Due to the specific design of CLIC with two parallel beam lines, the required spatial resolution for the loss location follows from two aspects [12].

- It is desirable to be able to distinguish losses originating from either the DB or the MB. Therefore, in horizontal transverse direction the necessary spatial resolution has to be better than 0.65 m, the distance between the beam lines.

The signal from the DB losses seen in monitors protecting the MB and vice versa is referred to as 'cross talk'. Due to the different characteristics of the DB (high intensity, low energy) and the MB (low intensity, high energy), it is conceivable that, e.g. a loss of a non-destructive power at the DB provokes a signal in the BLM at the MB side that is of the level of a destructive loss at the MB. Therefore, in order to avoid additional false trigger to the ones discussed in the previous section, the BLM signals from both sides of the TBM must be jointly considered before an injection inhibit.

However, the difference in time structures between the pulses from the MB and DB may further help to discriminate between losses from these two beams. As presented in Table 3.3, the bunch train duration, τ_{train} , is 156 ns in the MB and 240 ns in the DB. This time difference is necessary to due to the filling- and rise time of the AS and hence, at a particular position, the first bunch of the DB will arrive the 84 ns earlier

than the first bunch of the MB. Additional information from other instrumentation devices could also be employed.

- For diagnostic purposes, the longitudinal resolution should allow to resolve losses originating from two successive quadrupoles. In the CLIC DB, the shortest distance between two quadrupoles is 1 m and therefore, a longitudinal resolution of better than 1 m is desirable.

3.3.5 Temporal Resolution

The main task of the BLM system is as part of the MPS the protection of the main linacs and drive beam decelerators. The machine protection system, based on a 'next cycle permit' [11] requires a decision about the next pulse inhibit in less than 8 ms. Therefore, to fulfil the first mission of the system, a time resolution of this order is necessary.

For diagnostic purposes, a nanosecond scale resolution of a point-like BLM allows to resolve the time structure of the losses within a bunch train. Due to the difference in time structure of the MB and the DB, such high resolution may further help to discriminate between losses of these two beams.

3.3.6 Location Dependence

The system has to fulfil different specifications along the CLIC tunnel. Previous work [12] based on FLUKA simulations on absorbed doses due to different loss scenarios along the CLIC tunnel shows that the sensitivity varies by 2 orders of magnitude, while the dynamic range changes by one.

These results are not directly transferable to detectors based on Cherenkov light, nevertheless, they point out that the use of different detectors for various parts of CLIC may be necessary.

3.3.7 Radiation Hardness

Ideally, the BLM system should be sufficiently resistant to survive the entire lifetime of the accelerator. The intensity of ionizing radiation in an accelerator and thus the magnitude of the absorbed dose is proportional to the rate of beam loss. Estimates of maximum permissible beam loss during operation in CLIC are derived from considerations of beam dynamics as discussed in Section 3.3.1. The estimates for the annual absorbed doses at the CLIC TBM for the highest and lowest energies, i.e. 240 MeV and 2.4 GeV for the DB and 9 GeV and 1500 GeV for the MB, are presented in Table 7.1. The highest absorbed doses at a position close to the accelerator (cf. Figure 3.5). The assumptions made and the methods for the estimation are described in [9].

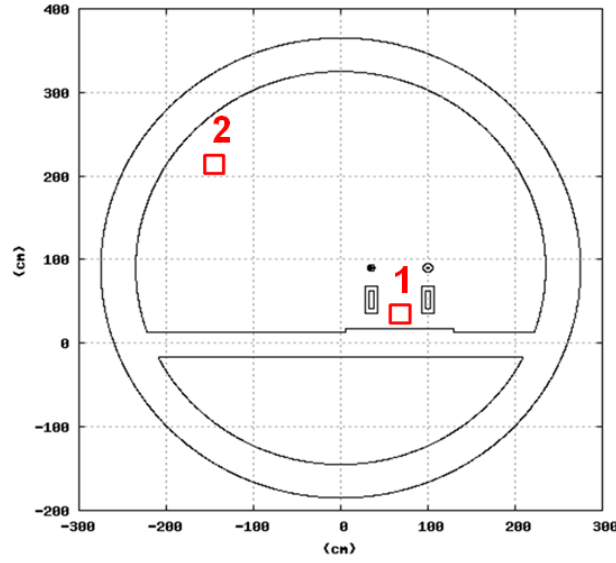


Figure 3.5: Locations in the CLIC tunnel (in red) related to the values presented in Table 7.1 [13].

	Absorbed dose close to accelerator [Gy/year]	Absorbed dose close to tunnel wall [Gy/year]
DB - 240 MeV	$\leq 10^4$	$\leq 10^3$
DB - 2.4 GeV	$\leq 10^5$	$\leq 10^4$
MB - 9 GeV	$\leq 10^4$	$\leq 10^3$
MB - 1500 GeV	$\leq 10^5$	$\leq 10^4$

Table 3.4: Estimates for the annual absorbed dose in two tunnel locations as shown in Figure 3.5 from the CLIC DB and MB, assuming 180 days continuous running with maximum permissible losses [13].

3.3.8 Considered Technologies

In the CLIC CDR [9], ionization chambers similar to the ones used at the LHC are specified as the baseline choice of BLM system in all machine sub systems except for the damping and predamping rings. The LHC ionization chamber itself has a very high dynamic range of at least 10^8 . The LHC readout electronics has a dynamic range of 10^5 and together with the LHC ionization chambers the sensitivity is $7 \cdot 10^9$ Gy in the shortest time integration interval. The main advantages of ionization chambers are radiation hardness and large dynamic range. Recently, diamond detectors have become increasingly popular for BLM purposes, for example at Fermilab or in LHC experiments. Their advantage is low dark current.

The total numbers of such localized BLMs required for the TBM is currently estimated to be in the range of 50.000. This estimation is based on the assumption that one BLM is placed at each quadrupole along the DB and MB. However, in order to reduce channels and costs, the total number of BLMs could be substantially reduced either by halving the number

of ionization chambers for the DB decelerator or by the use of alternative technologies, such like long ionization chambers (PLIC) [14] [15] or Cherenkov fibers [16] [17].

PLICs have successfully been used at SLAC for 20 years of running. However, their sensitivity and dynamic range may not meet the requirements for the TBM. Cherenkov fibers are an emerging technology and have mainly only been used as beam loss position monitors (BLPM), e.g. [18]. Their advantages and drawbacks for beam loss monitoring are discussed in detail in Chapter 7.

In both these technologies, the sensor is spanned along a distance (up to hundreds of meters) in parallel to the beam lines. The loss position is determined by a measurement of the arrival time of the loss signal at the end of the sensor with respect to a trigger signal that contains spatial and temporal information about the beam itself. Whereas this technology offers a high position resolution for single bunch losses, there is an ambiguity for signals resulting from different loss scenarios for multi-bunch trains. For example, the signal from losses of each bunch of the entire train at a single position and that from a portion of the bunches at more than one location can be similar. The resulting limits on the longitudinal resolution are discussed in Section 7.4.

3.4 CTF3 - the CLIC Test Facility

The CLIC Test Facility (CTF3) [19] is built for the proof-of-principle demonstration that the major CLIC technologies are feasible. The general layout is shown in Figure 3.6. CTF3 consists of a 150 MeV electron linac, followed by a series of two rings, the delay loop and the combiner ring. This part of CTF3 is a scaled-down version of the complex required to generate the CLIC drive beam. After the beam recombination in the combiner ring, the beam is sent to the CLIC experimental area (CLEX), towards the left of the layout. CLEX houses several beam lines such as the test beam line (TBL) and the two-beam test stand (TBTS) with the probe beam injector CALIFES, where the CLIC acceleration scheme will be tested. At the same time CTF3 offers possibilities to test CLIC instrumentation prototypes, like e.g. the Cherenkov fiber BLM system, in CLIC similar conditions.

3.4.1 Two Beam Test Stand

The two beam test stand (TBTS) is built to fully demonstrate the CLIC acceleration principle. The TBTS currently consists mainly of one PETS, one accelerating structure and the necessary instrumentation. The CTF3 drive beam generates power in the PETS which accelerates a probe beam that is generated by the CALIFES photo-injector in the CLEX hall.

3.4.2 Test Beam Line

The CLIC decelerator will decelerate the beam from 2.4 GeV to 0.24 GeV and it is mandatory to achieve small losses and avoid any instability. In CTF3 a test beam line is being constructed to test this deceleration. It currently contains 12 PETS and has space available for 16.

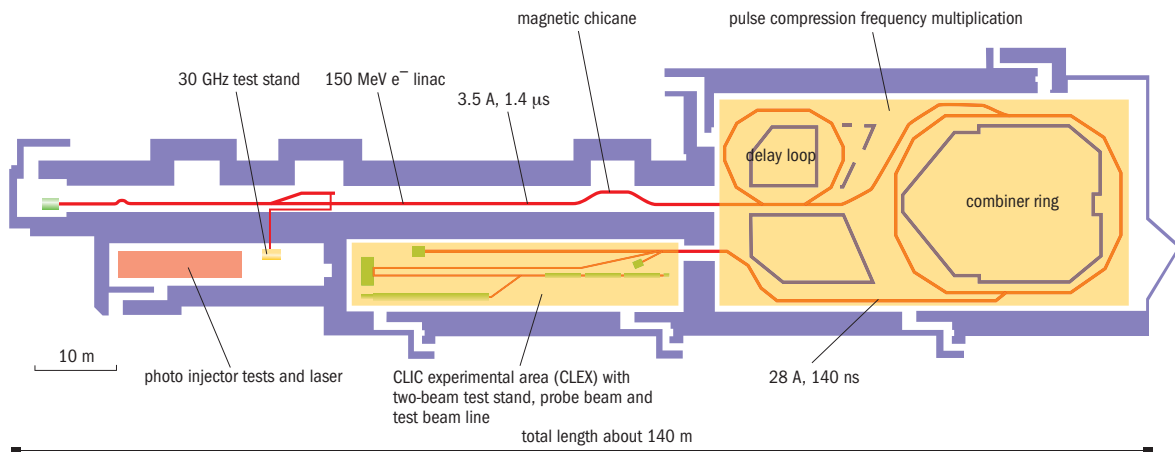


Figure 3.6: Diagram of the CLIC test facility (CTF3), with a 150 MeV linac, a delay loop and a combiner ring, together with the experimental area, CLEX [10].

4 Optical Fiber Waveguides and Photo Detectors

4.1 Optical Fiber Waveguides

An optical fiber is a cylindrical dielectric waveguide, consisting of a core surrounded by a cladding layer of slightly lower refractive index. The light is therefore guided within the fiber core.

Most fibers currently used in optical communication are made of high purity synthetic fused silica, SiO_2 , also referred to as quartz. There are two generic types of cladding. In all-fused-silica fibers, the lower refractive index region is created by doping the outer surface of the the preform from which the optical fiber is drawn, e.g. with germanium, fluorine or phosphorus. In the case of polymer-clad fibers, a lower refractive index material is applied around the core during the fiber drawing process. The cladding is covered with a buffer coating, as well an outer protection layer, the jacket. The buffer mostly consists of synthetic material, e.g. polyimide, acrylate, or silicone, and provides protection against mechanical damages and environmental influences. In particular, pure-silica-core (PSC) fibers with a doped silica cladding show superior performance with regard to low attenuation and radiation hardness.

The boundary between the core and cladding may either be abrupt - in step-index fibers, or gradual - in graded-index fibers. A step-index (SI) fiber is entirely specified by the refractive index of core, n_{co} , and cladding, n_{cl} , (cf. Figure 4.1), and their radii R and R_{cl} , respectively. Typical core to cladding diameter ratios (CCDR) are 1.1 or 1.2. A further useful parameter is the fractional refractive index change, Δ [20]:

$$\Delta \equiv \frac{n_{co}^2 - n_{cl}^2}{2n_{co}^2} \approx \frac{n_{co} - n_{cl}}{n_{co}} \ll 1 \quad (4.1)$$

The refractive index n_{co} ranges from 1.44 to 1.51, depending on the wavelength of the transmitted light (cf. Figure 5.2), and Δ typically lies between 0.001 and 0.03. Furthermore, fibers are often characterized by their numerical aperture, NA , which is defined as:

$$NA \equiv \sqrt{n_{co}^2 - n_{cl}^2} = n_{co} \sqrt{2\Delta} \quad (4.2)$$

The NA can be interpreted as the fiber input acceptance and therefore plays a critical role for the trapping of Cherenkov light within the fiber. Typically, for quartz fibers NA lies in the range between 0.1 and 0.6.

For a complete description of the propagation of light in an optical fiber, electromagnetic wave theory has to be considered. The base for this treatment are Maxwell's equations. For

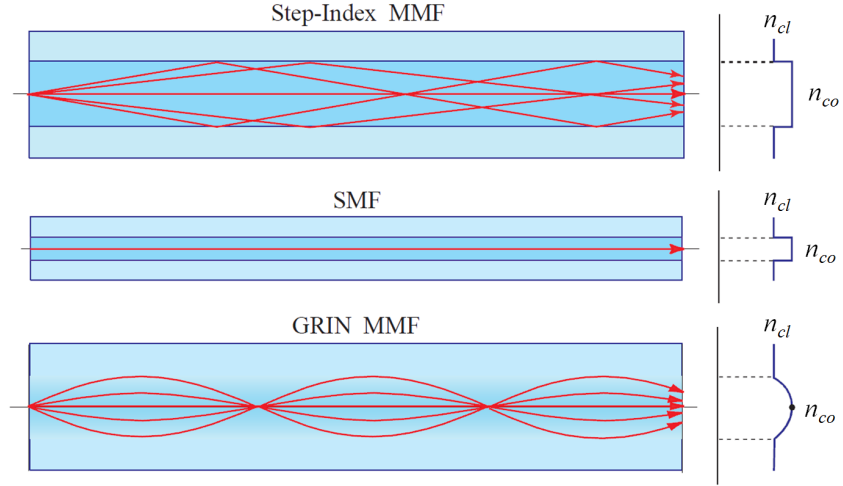


Figure 4.1: Geometry, refractive index profile, and typical rays in a step-index multimode fiber (MMF), a single mode fiber (SMF), and a graded-index multimode fiber (GRIN MMF) [20].

a medium with zero conductivity ($\rho = 0, \vec{j} = 0$), they can be written in terms of the electrical field \vec{E} , the magnetic field \vec{H} , the electric flux density \vec{D} , and the magnetic flux density \vec{B} as follows [21]:

$$\nabla \times \vec{E} = -\frac{\partial \vec{B}}{\partial t} \quad (4.3)$$

$$\nabla \times \vec{H} = \frac{\partial \vec{D}}{\partial t} \quad (4.4)$$

$$\nabla \cdot \vec{D} = 0 \quad (4.5)$$

$$\nabla \cdot \vec{B} = 0 \quad (4.6)$$

The four field vectors are related by:

$$\vec{D} = \epsilon \vec{E} \quad (4.7)$$

$$\vec{B} = \mu \vec{H} \quad (4.8)$$

where ϵ is the dielectric permittivity and μ is the magnetic permeability of the medium. Substituting for \vec{D} and \vec{B} and taking the curl of Equations (4.3) and (4.4) results in

$$\nabla \times (\nabla \times \vec{E}) = -\mu\epsilon \frac{\partial^2 \vec{B}}{\partial t^2} \quad (4.9)$$

$$\nabla \times (\nabla \times \vec{H}) = -\mu\epsilon \frac{\partial^2 \vec{H}}{\partial t^2} \quad (4.10)$$

A combination of the divergence conditions of Equations (4.5) and (4.6) with the vector identity relation

$$\nabla \times (\nabla \times \vec{X}) = \nabla(\nabla \cdot \vec{X}) - \nabla^2(\vec{X}) \quad (4.11)$$

leads to the nondispersive wave equations:

$$\nabla^2 \vec{E} = \mu\epsilon \frac{\partial^2 \vec{B}}{\partial t^2} \quad (4.12)$$

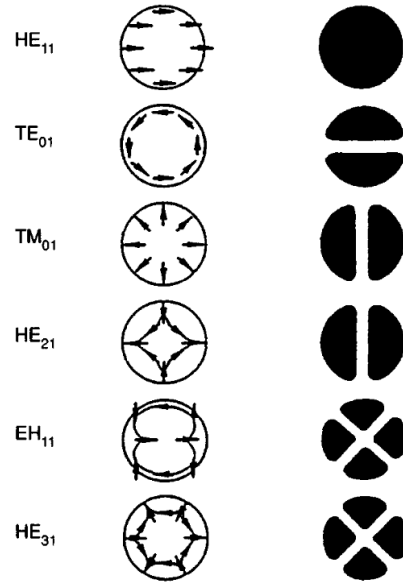


Figure 4.2: Transverse electric field patterns and field intensity distributions for the lowest modes in a step-index fiber [23].

$$\nabla^2 \vec{H} = \mu\epsilon \frac{\partial^2 \vec{H}}{\partial t^2} \quad (4.13)$$

where ∇^2 is the Laplacian operator. Both wave equations have to be solved according to the boundary conditions imposed by the cylindrical dielectric core and cladding. Detailed calculations can be found in [22, 20, 21, 23], in this thesis only the important results in relation to the theory of Cherenkov fibers will be discussed.

Modes - As with all waveguides, for an optical fiber there are certain special solutions to the wave equation, called modes. Each mode travels along the waveguide with a distinct propagation constant and group velocity, maintaining its transverse spatial distribution and polarisation. Modes are labeled as TE_{lm} (where $E_z = 0$) or TM_{lm} (where $H_z = 0$). The indices l and m characterize the azimuthal and radial distributions of a mode, respectively. Furthermore, hybrid modes where E_z and H_z are nonzero occur within a cylindrical waveguide (cf. Figure 4.2). These modes are designated HE_{lm} or EH_{lm} , depending upon whether the components of \vec{H} or \vec{E} make larger contributions to the transverse field [21].

The number of guided modes supported by the waveguide can be approximated by using its 'V-number', or normalized frequency, which is defined as:

$$V \equiv \frac{2\pi R}{\lambda} NA \quad (4.14)$$

The number of modes, N , supported as a function of V is given by [23]:

$$N = \frac{V}{2} \quad (4.15)$$

When $V < 2.405$, thus when the fiber radius R approaches the wavelength of the guided light λ , all modes with exception of the fundamental mode HE_{11} are cut off. Fibers that

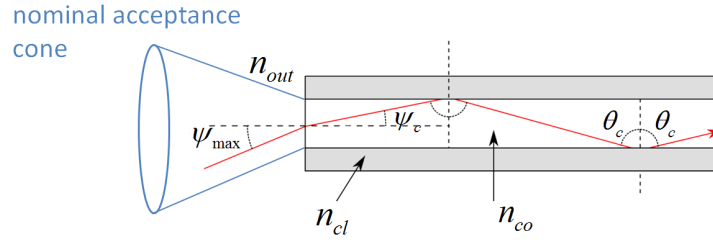


Figure 4.3: Critical ray path for light coupling from air into a step-index fiber, defining the nominal exit cone.

support many modes are known as multimode (MM), and those that support one (the HE_{11}) are known as single mode (SM) fibers (cf. Figure 4.1).

4.1.1 Ray Theory

For multimode fibers the concept of light propagation can be developed using either the ray theory, or the geometrical optics approach. An optical ray in a step-index fiber is guided by total internal reflection. Thereby the discrete set of modes resulting from wave theory can be interpreted as a discrete set of allowed reflection angles at the core-cladding boundary. However, for the dimensions of a typical Cherenkov fiber, with e.g. $d = 300 \mu\text{m}$, $NA = 0.22$, the number of modes is large and the discrete set of angles can be approximated to be continuous. Figure 4.1 shows possible ray paths in the different fiber types. For SI fibers, two fundamental types of rays can be distinguished:

Meridional rays - Meridional rays are confined to planes that pass through the fiber axis, as illustrated in Figure 4.4a. They are further defined by their longitudinal propagation angle ψ , which is confined between the ray track and the fiber axis. Meridional rays are guided if ψ is smaller than its critical value for total reflection determined by Snellius's law, i.e. if:

$$\psi \leq \psi_c = \arccos \frac{n_{cl}}{n_{co}} \quad (4.16)$$

Consequently, a ray incident from air, with $n_{out} \approx 1$, into the fiber becomes a guided ray if, subject to refraction at the fiber end face, it makes an angle ψ with the fiber axis that is smaller than ψ_c . As shown in Figure 4.3, when Snellius's law is applied to the air-core boundary, the angle ψ_{max} in air corresponding to the angle ψ_c in the core is obtained from $n_{out} \cdot \sin \psi_{max} \approx 1 \cdot \sin \psi_{max} = n_{co} \sin \psi_c$, which leads to $\sin \psi_{max} = n_{co} \sqrt{1 - (n_{cl}/n_{co})^2} = \sqrt{n_{co}^2 - n_{cl}^2}$. The acceptance angle of the fiber for meridional rays is therefore:

$$\psi_{max} = \arcsin(NA) \quad (4.17)$$

Thus, ψ_{max} defines the limiting cone for external rays to be coupled into the fiber - the nominal exit cone, and the numerical aperture is a measure of the light guiding ability of the fiber. Meridional rays correspond to the TE_{lm} and TM_{lm} modes [21].

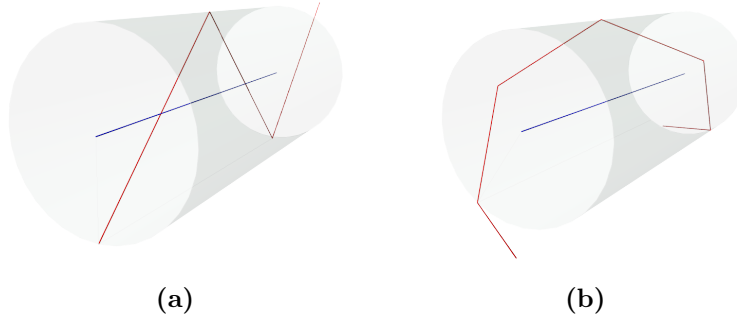


Figure 4.4: (a) Meridional ray and (b) skew ray. Meridional rays pass through the fiber axis after every reflection, skew rays follow a helical path.

Skew rays - Skew rays are rays that do not cross the fiber axis after every reflection and are fully defined by the longitudinal propagation angle ψ , and the azimuthal propagation angle η , where η is projected angle between the ray path and the normal to the core-cladding boundary into a plane perpendicular to the fiber axis (cf. Figure 5.5). A skew ray thus repeatedly reflects into planes that make the same angle η with the normal to the core-cladding boundary (= radius). The guiding conditions for skew rays are defined by the angle ξ between the normal to the core boundary at the point of reflection and the ray track. The angle ξ can be expressed in terms of ψ and η as (cf. Figure 5.5):

$$\cos \xi = \cos \eta \sin \psi \quad (4.18)$$

The ray is guided if ξ is larger than its critical value for total reflection, ξ_c , determined by Snellius's law, i.e. if:

$$\xi \geq \xi_c = \arcsin \frac{n_{cl}}{n_{co}} \quad (4.19)$$

Compared to meridional rays, skew rays have larger maximum acceptance angles $\psi_{max,s}$ given by [21]:

$$\sin \psi_{max,s} = \frac{NA}{\cos \eta} \quad (4.20)$$

Skew rays correspond to the HE_{lm} and EH_{lm} modes [21].

4.1.2 Attenuation

The power of a light signal traveling through an optical fiber decreases exponentially with distance L as a result of absorption and scattering. The associated attenuation coefficient is usually defined in units of dB/km and is denoted by the symbol α :

$$\alpha \equiv -\frac{10}{L} \log_{10} \frac{P(L)}{P(0)} \quad (4.21)$$

where $P(L)/P(0)$ is the ratio of transmitted to incident power. Consequently, for a given incident power and attenuation coefficient, the output power after a distance L is given by:

$$P(L) = P(0) \cdot 10^{-\frac{\alpha L}{10}} \quad (4.22)$$

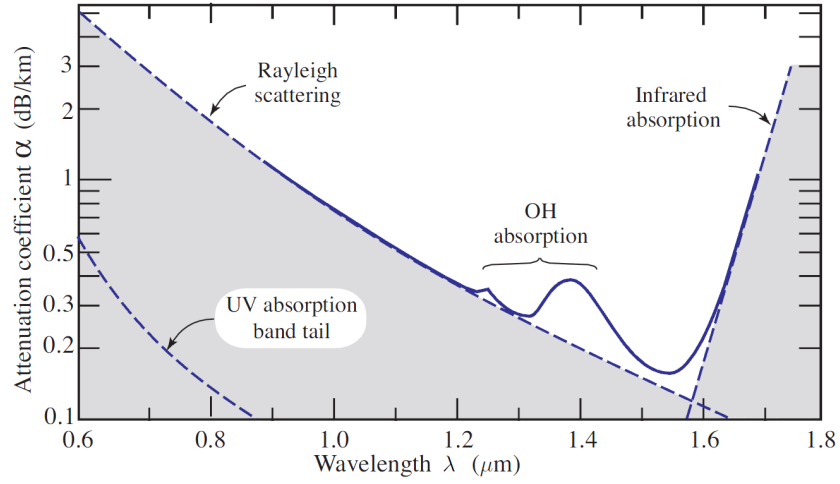


Figure 4.5: Attenuation coefficient α of quartz as a function of wavelength λ [20].

For quartz fibers the attenuation coefficient is strongly dependent on the wavelength λ of the transmitted light. As illustrated in Figure 4.5, the transparent window in quartz is limited by Rayleigh scattering on the short-wavelength side, and by infrared absorption on the absorption on the long-wavelength side, leading to an overall minimum of α at around $1.55 \mu\text{m}$.

Aside from these material-intrinsic effects there are extrinsic absorption bands that result from the presence of impurities, in particular metallic ions and OH radicals associated with water vapor in the glass. OH impurities are difficult to eliminate and affect the optical transmission performance in the near infrared region. Conversely, fibers with high OH content in the core perform significantly better in the near UV region and are more radiation resistant (cf. Section 4.2). Figure 4.6 shows an example for the nominal attenuation dependency on the wavelength for a high OH multimode fiber from the Thorlabs-BFH22 series.

Rayleigh scattering - For BLM applications quartz fibers are used as a Cherenkov light radiator. As discussed in Section 5.1, the spectrum of Cherenkov light is continuous, with an $1/\lambda$ dependency and a peak in the UV region. Due to the greater light yield, the part of the spectrum of greatest interest is situated at low wavelengths. However, many photodetectors have their Photo Detection Efficiency (PDE) peak in the wavelength range around 450 nm, which moves the spectrum range of interest to the blue.

In this wavelength region, Rayleigh scattering is the dominant factor contributing to the attenuation coefficient. It results from random inhomogenities in the refractive index, much smaller than the wavelength of the transmitted light. It is described by the Rayleigh scattering coefficient, γ_R , which is proportional to $1/\lambda^4$. γ_R can be approximated by [21]:

$$\gamma_R \approx \frac{A}{\lambda^4} \text{ quartz fibers} \approx \frac{0.83}{\lambda^4 [\mu\text{m}]} [\text{dB/km}] \quad (4.23)$$

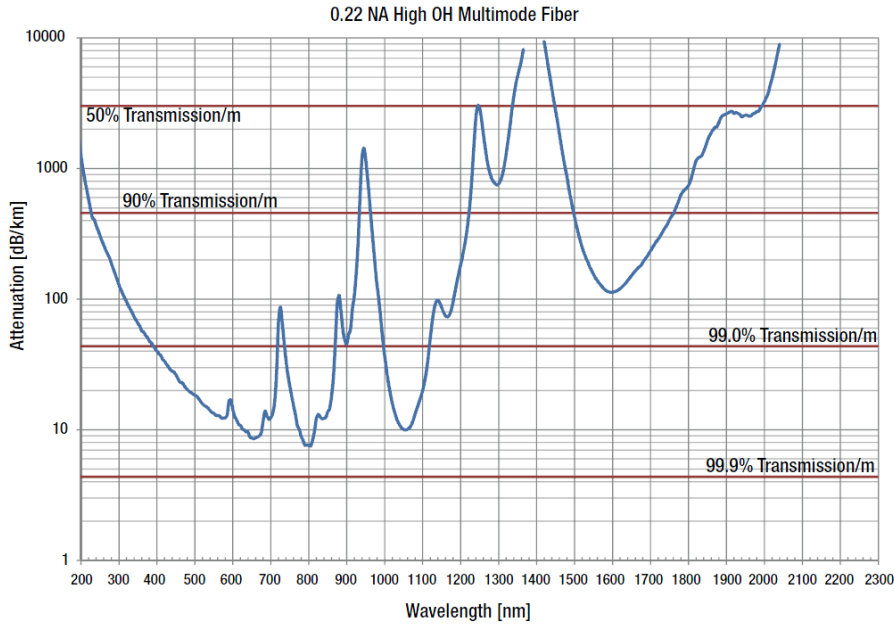


Figure 4.6: Nominal attenuation as a function of wavelength for a Thorlabs BFH22, high OH multimode fiber.

4.1.3 Dispersion

When a short pulse of light travels through an optical fiber, it experiences dispersion, i.e. the pulse spreads in time. In multimode fibers, the principal contributions are modal dispersion and material dispersion.

Modal dispersion - Modal dispersion in multimode fibers is a result of the different group velocities of the modes. In ray theory, this can be interpreted as the fact that rays entering the fiber at different angles travel different path lengths until they reach the far end of the fiber. Consequently they arrive at different times.

The shortest path length, L_{min} , is given by a path parallel to the fiber axis, whereas the longest possible path length, L_{max} , is defined by the critical longitudinal propagation angle, ψ_c . Following Figure 4.3 and then substituting (4.16), for meridional rays the ratio between the longest and shortest path is given by:

$$\frac{L_{min}}{L_{max}} = \cos \psi_c = \frac{n_{cl}}{n_{co}} \quad (4.24)$$

Consequently, if the propagation velocity along each track is assumed to be constant ($v = c/n_{co}$), the maximum propagation time spread for meridional rays after a travel distance L can be expressed as:

$$\Delta\tau_{max} = \frac{L_{max} - L_{min}}{c/n_{co}} = \frac{L}{c} n_{co} \Delta \quad (4.25)$$

This is only a rough estimate, since for skew rays the longitudinal propagation angles are allowed to be larger and thus also the dispersion is larger. Modal dispersion can be significantly reduced by the use of graded-index fibers [20].

Material dispersion - Quartz is a dispersive medium, i.e. its refractive index is a function of wavelength. In a simplified model each photon will - depending on its wavelength - travel with a velocity $v = c/n(\lambda)$ along its ray track. Two photons with λ_1 and $\lambda_2 > \lambda_1$, respectively, would therefore separate according to:

$$\Delta\tau \approx \frac{L}{c} \left(\frac{1}{n(\lambda_2)} - \frac{1}{n(\lambda_1)} \right) \quad (4.26)$$

4.2 Radiation Effects in Optical Fibers

A large number of experimental studies have been devoted to the characterization of the radiation effects in silica-based optical fibers to evaluate their vulnerability in harsh environments including space, military, civil nuclear industry, high energy physics experiments and future thermonuclear fusion plasma reactors [24]. Radiation in this context means ionizing radiation, i.e. X-rays, γ -rays and highly energetic particles.

When an optical fiber encounters radiation, all properties are affected. However, some are only relevant at high doses and have small practical influence. The main radiation effects fall into the following three categories [24, 25]:

- Radiation induced, increased absorption.
- Compaction or densification, which leads to:
 - change of refractive index
 - change of bandwidth
 - change of mechanical properties, e.g. strength and dimension.
- Radiation induced luminescence, which can be important in the context of using the fiber as a Cherenkov light radiator [25].

The most obvious and disturbing effect is Radiation Induced Absorption (RIA). It is a result of point defects in the silica lattice through ionization or displacement processes [26]. These point defects, or color centers, induce the appearance of new energy levels located inside the band gap. As a consequence, the defect-containing material absorbs a larger part of the transmitted light leading to an increase of the attenuation of the fiber waveguide. The induced attenuation typically is lower at higher optical wavelengths. Color centers mainly absorb in the UV and visible part of the spectrum, with absorption tails extending to the infrared. However, they can be made to disappear through thermal or optical processes, called 'photobleaching', causing a decrease in RIA. Also during the irradiation, both new color center formation and recovery compete. Therefore, the magnitude of the RIA also depends on the dose rate [24]. Some of the defects can also be excited by the photons transmitted along the fiber and then emit parasitic light that superimposes on the signal. This effect is called Radiation Induced Luminescence (RIL). The radiation responses of fibers, and in particular the RIA have manifold experimentally observed dependencies [25, 27]:

- Manufacturing conditions:
 - Fiber type - single mode, graded index, step index
 - Doping of core, doping of cladding, and the dopants concentration
 - Preform manufacturer and fabrication methods
 - Core material manufacturer - purity
 - OH content and other impurity concentration
 - Cladding Core Diameter Ratio (CCDR)
 - Coating (buffer) material
 - Drawing conditions
- Operation conditions:
 - Optical wavelength
 - Light power
- Environment:
 - Type of radiation, dose-rate and total dose
 - Irradiation history and annealing periods
 - Temperature
 - Mechanical stress

In combination with each other, these factors can cause a difference in the RIA of many orders of magnitude [25].

Due to the long list of parameters that influence the radiation response, and due to their mutual interference, it is difficult to transfer or even compare results from different tests. Extrapolations of the effects are rarely expedient, and no generally reliable predictive models are available. When dealing with RIA in optical fibers it is therefore of utmost importance to clearly specify which type of fiber, core and cladding materials and doping are involved, which environmental conditions and at what wavelength the stated values were measured. For a particular application a specific, preform dedicated radiation test is necessary.

Therefore only some examples of the influences of parameters are presented hereafter. Figure 4.7a shows a comparison between the RIA of fibers with different core doping materials [25]. The measurement was carried out with an optical wavelength of $\lambda \approx 830$ nm. Fiber manufacturers, applied dose, fiber diameter and CCDR rate are equal but not indicated. The pure silica core, step index fiber shows the best results, with a maximum RIA of 4-5 dB/km at a total absorbed dose of 10^4 Gy. Moreover, a relaxation process at a total absorbed dose of $\approx 10^3$ Gy is observed. The graded index fibers with an F-doped or Ge-doped core show saturation at higher dose levels. The worst result is obtained for the graded index P-doped fiber, with an RIA of $\approx 2 \cdot 10^4$ dB/km at 10^4 Gy and no foreseeable saturation.

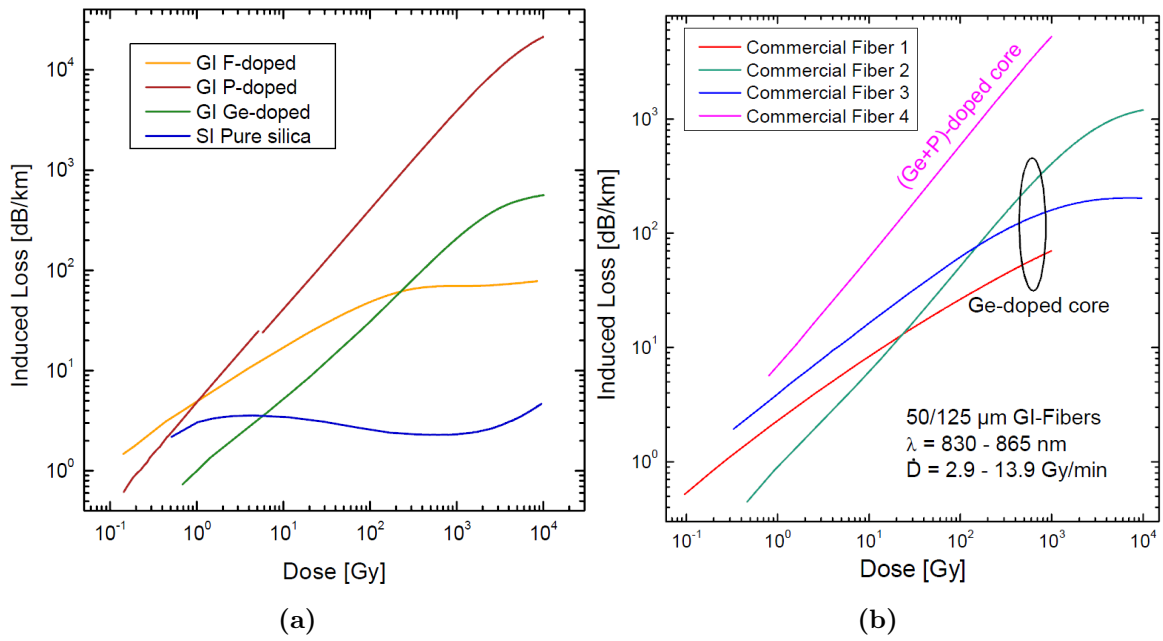


Figure 4.7: (a) Comparison between the RIA of fibers with different core doping materials as listed in the legend [25]. The RIA is measured for an optical wavelength $\lambda \approx 830 \text{ nm}$. Fiber manufacturers, applied dose, dose rate, fiber diameter and CCDR are equal but not indicated. (b) Comparison between the RIA of commercial fibers with equal core doping from different manufacturers [25]. Fiber type and diameter, λ and dose rate are listed in the legend.

Figure 4.7b shows the difference between the performances of fibers with equal core doping material, but from different manufacturers [25]. The fiber diameter, core doping material, optical wavelength and applied dose rate are listed in the legend of the plot. A difference in the RIA of a factor 100 at a total absorbed dose of 10^3 Gy is observed. This might be due to the different materials used for the fiber cladding and buffer, but, as indicated in the list above, there are many more parameters that depend on the manufacturing conditions. Most of them are generally not accessible for the users as they may be considered as confidential by the fiber manufacturers. So, as long as a manufacturer does not guarantee for a uniform fabrication method (material supplier, drawing speed, etc.) also for one single manufacturer the fiber characteristics can differ significantly.

4.2.1 Radiation Hardness

A variety of commercially available fibers exist that are referred to as 'radiation hard', however they typically only have a slightly lower RIA than other fibers of the same type [25]. Furthermore, RIA varies strongly with the wavelength λ of the transmitted light. Since most optical fibers are employed for data transmission, mostly only typically used wavelengths in this field, such as 0.85 , 1.3 or $1.5 \mu\text{m}$, are tested. With regard to the fact that the spectrum of Cherenkov light is continuous, sales information therefore has to be carefully reviewed and simplified statements questioned.

In high energy particle physics, quartz fibers have been used for several purposes as an active measurement medium in harsh environments. One example is the NA38 experiment at CERN, where quartz counters read out by quartz fibers were used to identify and center a sulfur ion beam [28]. The gain of the PMTs used for the readout of Cherenkov radiation in quartz has not been changed as a compensation for increases or decreases in light output after an integrated radiation dose of more than 50 Grad (500 MGy) over eight years. However, the wavelength range for which this statement is valid or type of employed PMTs is not specified.

A second example is the use of quartz fibers for Quartz fiber calorimeters, e.g. in the CMS experiment at the LHC at CERN [28]. This example is of particular interest regarding the employment of Cherenkov fibers for beam loss monitoring, since Quartz fiber calorimeters are also purely based on the detection of secondary shower particles by means of Cherenkov light generated within fibers. In the framework of the R&D for these calorimeters, two publications on the radiation hardness of fibers were published [28, 29].

In [28], five different fibers were irradiated: one with fluorine doped, quartz cladding and four different types of plastic clad fibers. All the fibers were produced by Spectran, USA. The irradiations were performed using a 2 MeV electron beam. The light output measured was produced by Cherenkov light of the irradiation electrons crossing the fiber at 45° and at a fixed location on the fibers. In this way, radiation damage affecting the Cherenkov light production and loss in transmittance for light could be observed simultaneously. The light was detected with a CCD camera with visible light optics. A peak dose of 2.2 Grad (22 MGy) was delivered over a period of 130 min.

Figure 4.8 shows the relative light yield for the five different types of fiber as a function of dose. HCG is an ultra-pure quartz fiber with a fluorinated quartz cladding; HCR is an ultra-pure fiber with high OH content core and plastic cladding; HCP is the same type as HCR but with a low OH content core material, and HCM are the cheapest fibers in the tested series, due to a higher level of impurities. Relatively little or no loss was observed for the quartz clad fiber, while the plastic clad fibers lost transmission after approximately 700 Mrad, presumably due to the structural damage of the plastic cladding.

In [29] various fibers produced by Polymicro, USA, were irradiated 3 MeV electrons at a rate of approximately 1 Mrad/h. Before and after irradiation, the Cherenkov light yield due to an irradiation by a Strontium 90 beta source was measured. The signal was measured as a DC current in a Hamamatsu R329 PMT, which has a glass surface that does not transmit UV light.

Figure 4.9 shows the irradiation test results. This test reveals the influence of the buffer material. Whereas fibers with with a doped silica clad and an aluminium buffer showed no damage up to 12 Mrad (120 kGy), the fiber with a doped silica clad and an acrylate buffer showed 10% degradation at the same dose level. The worst results were obtained for fibers with polyimide buffer.

Both tests described above are very promising for the application of Cherenkov BLMs for the CLIC TBM. However, the part of the light spectrum which showed the obtained stability is not specified. In both tests, optical components only suitable for the visible spectrum were

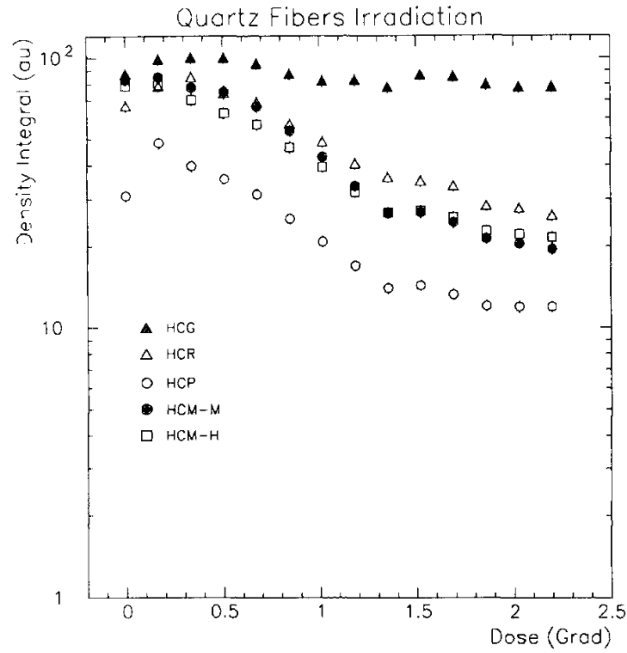


Figure 4.8: Integrated light yield for different kinds of quartz fibers as a function of delivered dose as presented in [28]. HCG (filled triangles) is an ultra-pure quartz fiber with a fluorinated quartz cladding; HCR (open triangles) is an ultra-pure fiber with high OH content core and plastic cladding; HCP (open circles) is the same type as HCR but with a low OH content core material, and HCM (filled circles and open squares) are the cheapest fibers in the tested series, due to a higher level of impurities.

used.

Solarization resistant fibers - Recently the use of optical fibers for applications, such as laser or plasma diagnostics [30] has lead to the requirement that they are radiation hard in the ultraviolet and visible (UV-Vis) part of the spectrum. For other applications, e.g. spectroscopy, fibers with improved UV transmission are needed to transport relatively high amounts of UV light ($\lambda < 300$ nm). It has been observed that high power UV light inside a fiber can generate absorbing defects leading to darkening phenomenons. This UV effect is called 'solarization'. In order to reduce the impact of the effect, 'solarization resistant' (SR) fibers have been developed. Studies have pointed out some similarity between effects of UV and γ -rays [30] and therefore also the general response to ionizing radiation is expected to be improved.

Figure 4.10a presents an example (see [30]) of the RIA spectral dependence measured at different dose steps for an SR fiber of type FVP-STD, manufactured by Polymicro, USA. The spectra are measured during a steady state irradiation with 10 keV X-rays at a dose rate of 5 krad/s. In the inset of Figure 4.10a, the radiation responses of three other SR fibers (Polymicro FVP-UVMI, FVP-UVMI, FDP-STD) and one pure-silica-core (PSC) fiber (Polymicro SSU) are compared (same radiation and dose rate as above), for a total absorbed dose of 50 Mrad [30], which is equal to 500 kGy. For the tested SR fibers, the RIA is 100

Quartz fiber	Diameter (micron) core outer		Clad	Buffer	Damage (3 Mrad)	Damage (12 Mrad)
1. FVL400440520	390	520	Doped silica	Aluminum	0	0
2. FIA200240500	202	500	Doped silica	Acrylate	0	10%
3. SHA300320345	297	343	Proprietary	Acrylate	20%	50%
4. FIP200220240	200	239	Doped silica	Polyimide	20%	40%
5. FIL300330370	300	428	Doped silica	Aluminum	0	0
6. FVP300315345	301	348	Doped silica	Polyimide	35%	55%
7. FIS200220500	203	504	Doped silica	Silicone	Breaks too easily	
8. FVP300330370	300	370	Doped silica	Polyimide	30%	50%
9. FVP300330370	300	370	Doped silica	Polyimide	33%	
Second batch	Sept.	1998				
10. FVP200220240	200	240	Doped silica	Polyimide	35%	
Second batch	Sept.	1998				

Figure 4.9: Irradiation test results as stated in [29]. All listed fibers are produced by Polymicro, USA.

times higher at 250 nm compared to 350 nm. The measurements show, that the RIA levels for $\lambda < 300$ nm are too high for use at such wavelengths. $\text{RIA} > 100$ dB/m corresponds to a decrease of greater than 50% of the signal after only a length of 3 cm.

Figure 4.10b shows the spectral dependency of the RIA measured 1 s after an X-ray pulse of ~ 20 krad for the same four SR fibers as mentioned above. Furthermore it shows the RIA measured at the same total dose per shot for four radiation tolerant PSC fibers: Polymicro SSU, STU and F-doped. These fibers are compared to two other optical fibers (cores doped with P and Ge) [30]. The SR fibers present the lowest RIA for this specific measurement. The comparison of the SR fibers with the three PSC fibers reveals largest losses for low-OH fibers (STU, KC4B), whereas the high-OH fiber (SSU) presents losses quite comparable to the SR samples. The two other fibers have far higher losses, e.g. at 300 nm 1000 times higher than for the SR fibers.

The total dose of this test was quite low compared with the CLIC requirements, however it shows the great possible differences of the spectral behaviour between different products of one manufacturer.

Summary - There are very few "rules of thumb" that can be applied when selecting a fiber. However, whilst they must be used with caution, for Cherenkov BLMs some recommendations are established [25]. First, it is important to know the manufacturers, i.e. who has drawn the fiber and who has made the preform. In respect of the radiation resistance, high OH, pure silica core step-index fibres with F-doped cladding have in general shown good results. For the future, solarization resistant (SR) fibers might be an interesting option. A large core diameter maximises the sensitive sensitive volume and therefore the generated light signal, however the diameter is usually proportional to the price. In order to reduce the signal background, the fiber should be shielded against ambient light. Those considerations finally led to the selection of a step-index fiber with $300 \mu\text{m}$ core / $330 \mu\text{m}$ cladding diameter, acrylate coating and a black nylon buffer for most of the realized projects, e.g. at FLASH at

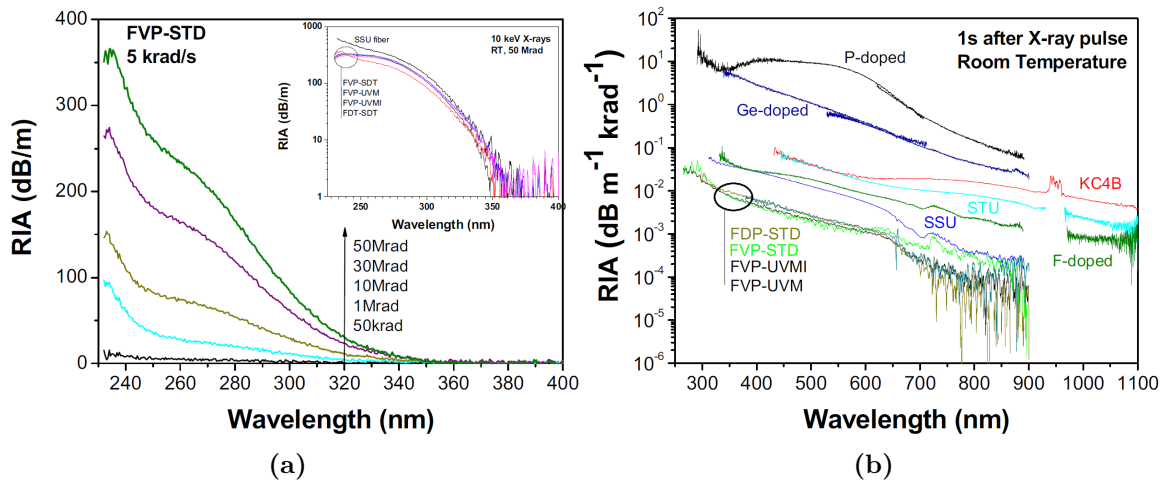


Figure 4.10: Spectral dependence of RIA in several fiber types as presented in [30]. **(a)** Example for the Polymicro FVP-STD fiber. In the inset, the responses of three other SR fibers (Polymicro FVP-UVM, FVP-UVMI, FDP-STD) and one pure-silica-core (PSC) fiber (Polymicro SSU) are compared for a steady state 10 keV X-ray irradiation, with a dose rate of 5 krad/s (10 krad/s for the SSU fiber) and a total absorbed dose of 50 Mrad (= 500 kGy). **(b)** RIA spectrum measured 1 s after X-ray pulse of ~ 20 krad at room temperature in the SR fibers and in other samples with pure (SSU, STU, KC4B) or doped cores (P, F, Ge-doped).

DESY [31] or Elettra [18].

4.3 Photo Detectors

When employing a Cherenkov fiber BLM system, the produced Cherenkov light has to be detected at either one or both ends of the fiber. Looking into references for the used photodetectors (PD) for Cherenkov fiber BLM or BLPM systems, e.g. [16, 25], Photon Multiplier Tubes (PMT) seem to be the common choice. Beside PMTs, also a relatively new type of photon counting devices, Silicon Photo Multipliers (SiPM), are used [18]. Considering the requirements on the CLIC-TBM beam loss monitoring system, both devices seem to be promising candidates. In the following, the basic characteristics of both photodetector types are discussed.

4.3.1 Photo Multiplier Tube (PMT)

PMTs have been extensively used in the past decades in high energy particle physics and therefore their characteristics are well known. PMTs are still the leading technology for many performance parameters, like timing, gain, or noise. Since the devices have a long history and many design variants, a broad applicability is ensured.

The PMT consists of an input window, a photocathode, focussing electrodes, an electron multiplier (dynodes) and an anode, all housed in vacuum tube (see Figure 4.11). The multiplied electrons are collected at the anode to produce the output signal.

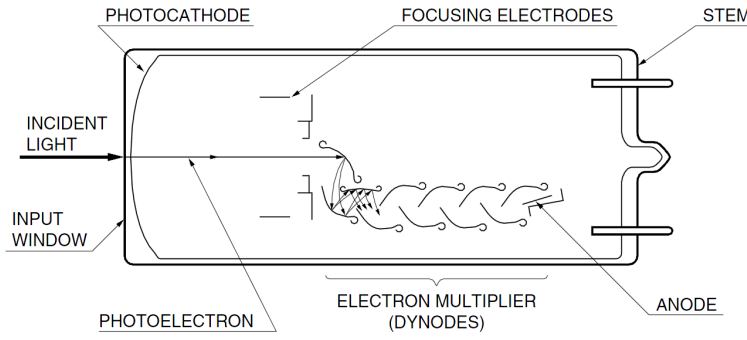


Figure 4.11: Schematic drawing of a PMT [32].

During operation a high voltage is applied to the cathode, dynodes and anode such that a potential 'ladder' is set up along the length of the cathode-dynode-anode structure. When an incident photon impinges the photocathode, an electron is emitted via photoelectric effect. Because of the applied voltage, the electron is accelerated towards the first dynode, where it releases secondary electrons which, in turn, are accelerated towards the next dynode. An electron cascade down the dynode string is thus created. At the anode, this cascade is collected to give a current which can be amplified or directly measured. A PMT can be operated in continuous or pulsed mode and, if operated in its linear region, the current output will be directly proportional to the number of incident photons.

Each of the PMT components has important consequences for its operational behaviour:

Input window and photocathode - The input window and photocathode are both responsible for the spectral response of the PMT. The photocathode converts incident light into photoelectrons by the photoelectric effect. The conversion efficiency varies strongly with the wavelength of the incident light. The spectral response range is determined by the photocathode material on the long wavelength edge, and by the window material on the short wavelength edge. The overall spectral response is usually expressed in terms of quantum efficiency $QE(\lambda)$:

$$QE(\lambda) = \frac{\text{Number of Photoelectrons}}{\text{Number of Photons}} \quad (4.27)$$

For the linearity of the device, the resistivity of the cathode is also an important factor, in particular if it is operated at low supply voltage and high current [33, 34].

Electron multiplier (dynodes) - The electron multiplier system amplifies the small primary photocurrent by using a series of dynodes (cf. Figure 4.11) to produce a measurable current at the anode of the PMT. Most conventional PMTs contain 8 to 12 dynode stages and can reach overall amplification factors or gains up to 10^7 . Dynode strings can be constructed in many ways and, depending on the configuration, affect the response time and range of linearity of a PMT. The best results in this context are obtained by a linear focussed or

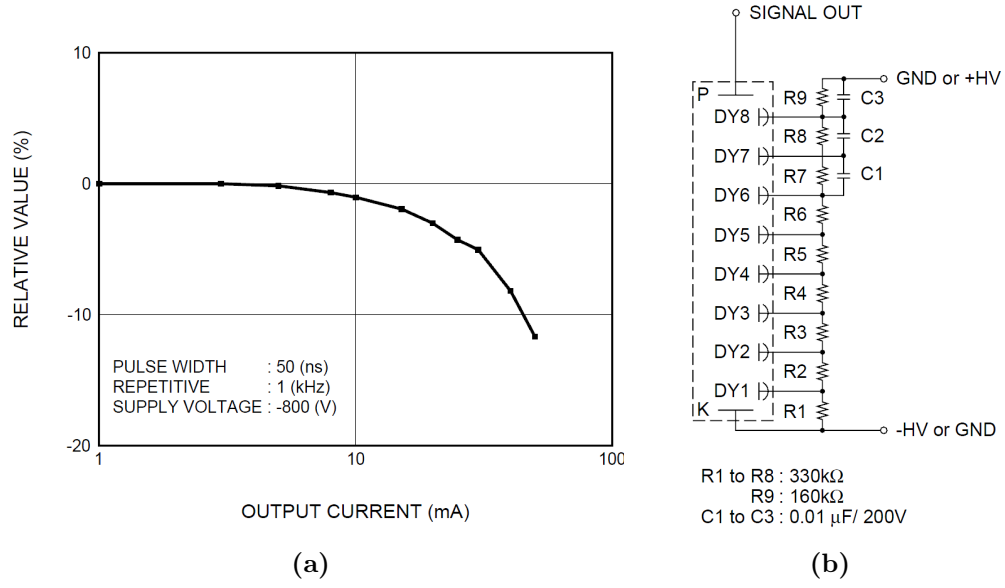


Figure 4.12: (a) The pulse linearity characteristic of the Hamamatsu R7400U PMT. An output current of 30 mA is attained at a 5 % deviation from ideal linearity. (b) The voltage divider circuit incorporated in the Hamamatsu E5770 Socket Assembly [35].

metal channel types [34, 32].

The gain is strongly dependent on the number of dynodes and the secondary emission factor δ , which is a function of the energy of the primary electron. The electron energy, in turn, is dependent on the potential difference between each dynode.

In relation to gain stability, it is crucial to have a well regulated voltage applied to the dynodes. Commonly this is achieved by a stabilized voltage supply in conjunction with a voltage divider. A voltage divider consists of a chain of resistances chosen such as to provide the required voltage to each dynode. It must be designed in such a way to prevent the occurrence of large potential variations between the dynodes due to the changing in current in the tube. Such variations would cause fatal changes in gain and linearity of the PMT. For this reason, it is important that the current in the resistance chain is large compared to the anode current. If a linearity of better than $\pm 1\%$ is required, the maximum output must be held less than a 1 % of the divider current [33].

When a PMT is pulse-operated, peak currents much larger than this limit can occur, particularly in the last dynode stages. To prevent this problem, decoupling capacitors can be connected to the last few stages (see Figure 4.12b). These capacitors provide the necessary charge during the peak period and thereby significantly improve the linearity. Figure 4.12a shows an example of the pulse linearity characteristics for the Hamamatsu R7400U PMT.

To achieve an output linearity of better than $\pm 3\%$, assuming having three capacitors in the voltage divider circuit (cf. Figure 4.12b), the amount of charge Q_3 , stored in C_3 , should

be greater than 100 times the integrated charge of the signal Q_0 :

$$Q_0 = \int_{Pulse} I_{out}(t) dt \quad (4.28)$$

Accordingly, the charge Q_2 , stored in C_2 , should be a factor 50 and the charge Q_1 , stored in C_1 , should be a factor 25 times Q_0 [33].

Moreover, deviations from proportionality can be caused by space charge effects in the later stages of the electron multiplier. The magnitude of this effect depends pulse height of the PMT output current and on the strength of the electric fields between the dynodes.

4.3.1.1 Main Characteristics

Spectral response - The spectral response is the relationship between wavelength of the incident light and the photocathode sensitivity. It is described by the quantum efficiency $QE(\lambda)$. A QE up to 45 % at the peak wavelength is possible. There is a variety of PMTs with different spectral ranges available.

Gain - The gain for a given PMT is strongly dependent on the applied voltage. PMT gains are typically in the range of 10^6 .

Anode dark current - When a PMT is not illuminated, but connected to HV, a small current still flows. This current is called dark current and arises mainly from thermionic emission of electrons from the cathode and dynodes. Other contributions are e.g. leakage currents or field emission. Typical dark currents are in the range of 1-10 nA, depending on the type of PMT.

Pulse linearity and dynamic range - The pulse linearity is defined by the proportionality between the input light amount and the output current in pulse operation mode. The pulse linearity is usually defined by an output current at which a deviation of $\pm 5\%$ from linearity is reached [32]. Typical maximum anode currents are in the range of 5-100 mA, depending on the type of PMT.

By considering the dark current and the maximum output current for linearity, the dynamic range of PMTs can be deduced. The dynamic range of PMTs is usually of the order 10^6 .

Time response - The time response of a PMT is primarily determined by the transit time required for the photoelectrons emitted from the photocathode to reach the anode, as well as the transit time difference between each photoelectron. The main influence factors are the dynode type, but also the supply voltage. In general, the time response improves in inverse proportion to the square root of the supply voltage [33].

- **Rise time and fall time.** The rise time is the time taken for the anode output pulse to rise from 10 % to 90 % of the peak amplitude when the whole photocathode is illuminated by a delta-function light pulse (cf. Figure 4.13). Typical values are a few ns, whilst better performing PMTs can have rise times of 0.5 ns.

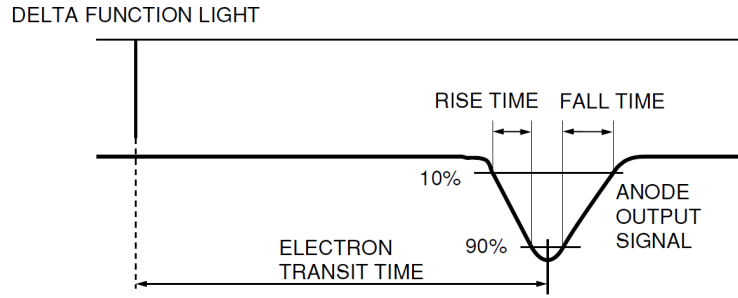


Figure 4.13: Definition of rise/fall time and electron transit time [33].

Conversely, the fall time is defined as the time required to decrease from 90 to 10 % of the peak output pulse height. In general, the fall time of a PMT is two or three times longer than the rise time [33].

- **Electron transit time.** The electron transit time is the time interval between the arrival of a light pulse at the photocathode and the appearance of the output pulse. Typical values are 5-40 ns.
- **Transit time spread (TTS).** The TTS is also called the transit time jitter. It is the fluctuation in transit time between individual pulses , and is defined as the FWHM of the frequency distribution of electron transit times. Typical values are in the range of 0.5 ns, good PMTs can have a TTS of 200 ps.

4.3.2 Silicon Photo Multiplier (SiPM)

Recently, semiconductor based photosensors become more and more competitive. In a few aspects they are even superior to classical PMTs: Semiconductor based devices allow more compact designs, the devices are insensitive to magnetic fields, and the photon detection efficiency (PDE) can be significantly higher. Moreover, the required bias voltage, the power consumption and also the costs are usually lower. From the variety of products, especially the group of Geiger-mode operated pixel devices, often referred to as SiPMs (Silicon Photo Multiplier) are very promising for the application of Cherenkov fiber BLM systems.

The detection of photons in semiconductors is based on the generation of electron-hole pairs within a depletion layer during the absorption of photons. The generated electrons and holes move in an electric field and the current of the moving charge is registered as a signal. The electric field is generated by applying an external voltage to a *pn*-junction in the semiconductor. As for classical PMTs, the detection efficiency depends strongly on the wavelength of the incident photons. This dependency is based on the bandgap of silicon, and the absorption length of the photons. Photons with shorter wavelength have a shorter absorption length. Consequently, as only electron-hole pairs generated within the depletion layer contribute to the signal, the PDE drops with shorter wavelength.

If the electric field is high enough, electrons and holes can gain sufficient energy between collisions with the semiconductor lattice to generate further electron-hole pairs. This avalanche

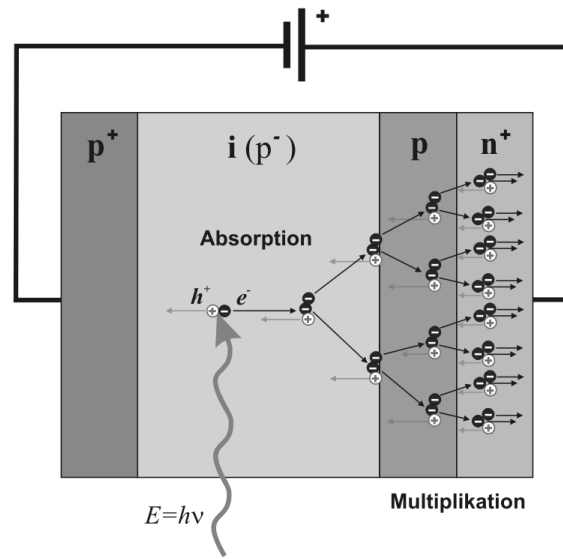


Figure 4.14: Operating principle of an APD [37].

effect is used to amplify the signal. Three operation regimes can be distinguished [36]:

- **No gain.** PIN diodes have a large depletion layer between the p - and n -doped layers, in which the electron-hole pairs are collected. Accordingly, the quantum efficiency and spectral sensitivity are high. However, the maximal generated charge is only one electron-hole pair per photon. The signal amplitude is practically independent of the temperature.
- **Proportional gain.** Avalanche photodiodes (APD) show a proportional amplification when a reverse bias voltage is applied. Usually the design combines a long drift (depletion) region with a subsequent short avalanche region (cf. Figure 4.14). This allows a good spectral acceptance and a good control of the amplification process. APDs have a typical gain of 100.
- **Geiger-mode operation.** When the reverse voltage applied to an APD is slightly higher (10 %-20 %) than its breakdown voltage, the internal electric field becomes so high that a huge gain (10^5 to 10^6) can be obtained. Operating an APD under this condition is referred to as 'Geiger mode' operation. The emerging avalanche has to be quenched externally, which is often done by a high ohmic resistor. This quenching process causes a recovery or dead time of the APD. The size of the signal is defined by the geometrical design and the operation (over-) voltage, but not on the initially generated charge and thus number of impacting photons.

In general, the gain of avalanche multiplication depends on the temperature. This is due to the temperature dependence of lattice vibrations. With increasing temperature the mean free path of the electrons and holes reduces, as the probability to interact with a phonon increases. Consequently, the electrons have less time to gain energy before they lose it again in collisions, and the gain of the device decreases.

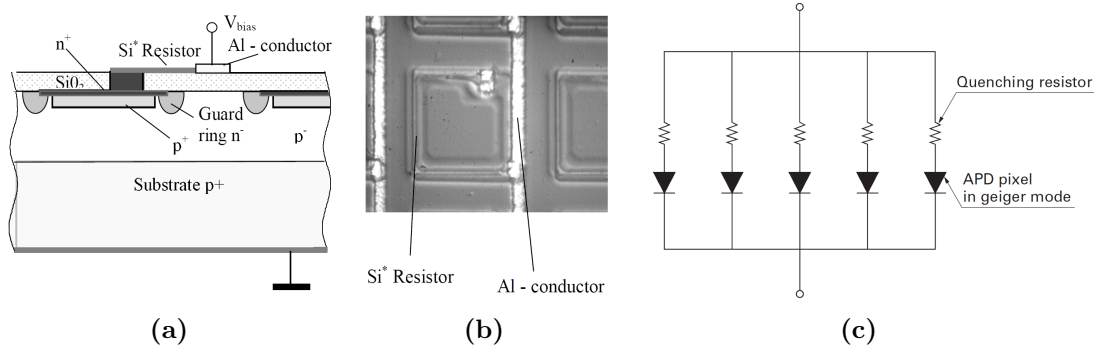


Figure 4.15: (a) SiPM topology [38], (b) microscopic image [38], and (c) equivalent circuit [39].

In semiconductor based PDs, the operation voltage influences not only the gain of the device, but also the size of the sensitive region inside the semiconductor. This leads to a change in detection efficiency with operation voltage and consequently to a change of sensitivity of the device [36].

The disadvantage of Geiger mode operation is that the proportionality to the incident light signal is lost. To overcome this problem, many small Geiger mode operated APD pixels can be arranged in an array. In this thesis, this kind of device will be referred to as Silicon Photomultiplier (SiPM) [38]. However, different producers use different names for similar devices, e.g. Hamamatsu - MPPC, SensL - SPM, ST-Microelectronics - SPAD, CPTA - MRS, etc. Typically the pixel size is in the range of 15 to 100 μm , and the total number of pixels is 100 - 4000 per mm^2 . Latest developments even provide SiPMs with up to $4 \cdot 10^4$ cells per mm^2 [40].

All pixels of the array are connected in parallel (cf. Figure 4.15c) and therefore the total analog output signal of the SiPM is the sum of all outputs of all pixels, creating a large pulse. By measuring the height or electrical charge of this pulse the number of photons detected by the SiPM can be estimated by [39]:

$$Q_{\text{out}} = C_{\text{pix}} \cdot (V_R - V_{BR}) \cdot N_{\text{fired}} \quad (4.29)$$

where C_{pix} is the capacitance of one APD pixel, N_{fired} is the number of APD pixels that detected photons, V_R is the applied reverse bias voltage, and V_{BR} is the breakdown voltage of the APD pixel. The factor $C \cdot (V_R - V_{BR})$ is the single pixel gain.

When photons enter an APD pixel operated in Geiger mode, the pulse output of the pixel is constant, regardless of the number of incident photons or their energy. This means that each APD pixel only provides a binary information on whether or not it received one or more photons. This binary behaviour leads to a very characteristic pulse height or output charge distribution of SiPMs when illuminated at very low intensity. Figure 4.16a shows a typical example for the output charge distribution. The first peak to the left represents the pedestal noise. The second peak represents the pulse height due to one pixel fired (1 p.e.,

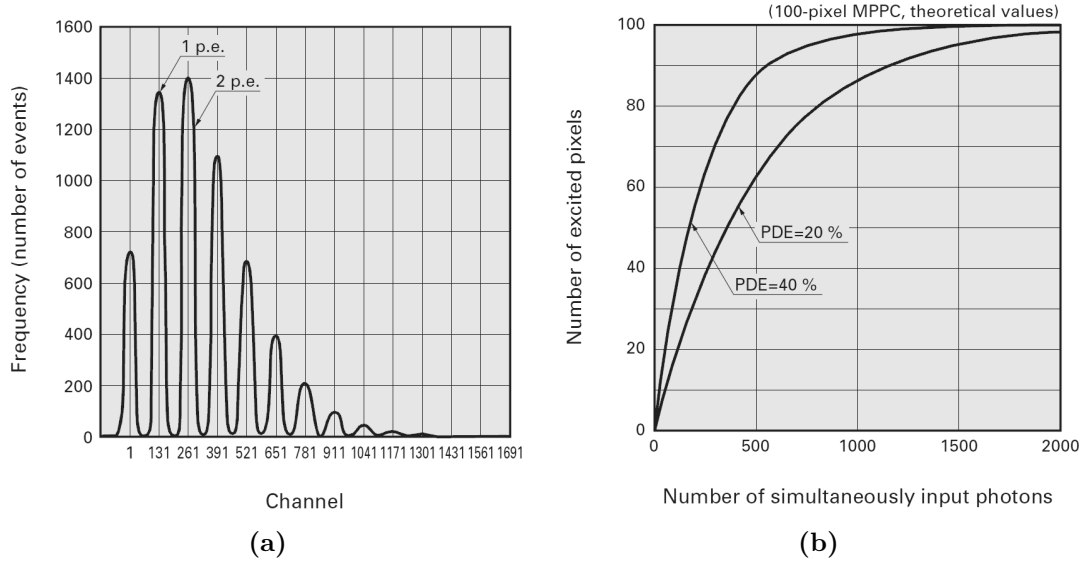


Figure 4.16: (a) Frequency distribution example of output charge [39]. (b) Theoretical curves for the saturation effect in a 100 pixel SiPM according to Equation (4.30), with ϵ_{ct} set to zero [39].

i.e one photon equivalent), the third due to two pixels fired simultaneously (2 p.e.), etc. The distance between the peaks corresponds to the single pixel gain, whereas the width of the peaks allows conclusions on the pixel- to -pixel gain variation.

The dynamic range of SiPMs is limited by the number of pixels. In order to ensure a linear operation, the incident photon flux has to be limited to a level such that the probability of multiple hits of one pixel during its recovery time is negligible. Theoretically, the relation between the mean signal S of an SiPM and the number of incident photons N_{photon} can be expressed by [39, 36]:

$$S = g \cdot N_{fired} = g \cdot N_{total} \cdot \left[1 - e^{-\frac{N_{photon} \cdot PDE \cdot (1 + \epsilon_{ct})}{N_{total}}} \right] \quad (4.30)$$

where, N_{total} is the total number of pixels of the SiPM, g is the single pixel gain, and ϵ_{ct} is the crosstalk probability. Figure 4.16b shows two example response curves for an SiPM with 100 pixels and an optical crosstalk probability of zero.

When the incident light pulse has a duration larger than the recovery time, an additional saturation effect occurs that is related to the pixel dead time: If, after an initial photon, the pixel is hit again before it is completely recovered, i.e. the pixel capacitance is fully recharged, a smaller pulse than expected is obtained. The amplitude of the pulse therefore varies according to the charging level.

4.3.2.1 Main Characteristics

Spectral response - In addition to the quantum efficiency $QE(\lambda)$, that fully defines the spectral response of PMTs, for SiPMs two more influence parameters have to be considered: First, the fact that the probability for photon detection is lower due to insensitive areas on

the detector surface, ϵ_{geo} , and secondly the fact that the probability to trigger a Geiger-avalanche for each electron-hole pair, $\epsilon_{trigger}$ is not unity. The quantity which summarizes all three parameters is the Photon Detection Efficiency, PDE [41, 39]:

$$PDE = \frac{\text{Number of detected Photons}}{\text{Number of Photons}} = QE \cdot \epsilon_{geo} \cdot \epsilon_{trigger} \quad (4.31)$$

The QE itself is usually above 75 % and mainly depends on λ . ϵ_{geo} depends on the pixel size, since the dead area due to the voltage supply lines and pixel decoupling regions increases with smaller pixels. $\epsilon_{trigger}$ depends on the over-voltage above breakdown and on λ . The peak overall PDE is typically 30 % for devices with 1500 pixels per mm^2 , and 75 % for devices with 100 pixels per mm^2 .

Gain - The gain of an SiPM strongly depends on the operation voltage and on the temperature. In order to obtain stable output, it is essential to change the bias voltage according to the temperature, or to keep the temperature constant. Typically, the maximum gain is in the range of 10^5 to 10^6 .

Dark count rate and optical crosstalk - Electron-hole pairs generated without the involvement of photons - either by thermal or field assisted excitation - give rise to unwanted noise that can also trigger a Geiger-avalanche in a pixel. The resulting signal is indistinguishable from a photon induced signal. However, since noise occurs randomly in time, it is very unlikely that dark counts at a 2 p.e., 3 p.e., or 4 p.e. level are detected. This means that the effects of dark counts can be reduced by adjusting the threshold level. If the arrival time of the incident light is known, the effects of dark counts can be further reduced by setting an appropriate time gate. The dark count rate is strongly depending on the temperature and rises exponentially with applied over-voltage. A rule of thumb for the thermal dependency is that the dark rate doubles for each temperature increase of 8°C [41]. Typical dark count rates at room temperature are in the range of a few hundred kHz/mm^2 up to MHz/mm^2 .

During an avalanche, additional photons in the visible range are emitted. If they reach the neighbouring pixel, additional breakdowns, nearly simultaneous with the primary breakdown, can be caused. This effect is the origin for the high noise rate at levels above 1 p.e. and is called optical crosstalk. Its probability can be described by a parameter ϵ_{ct} , which depends on the gain and the geometrical layout of the pixels. At fixed gain values, small pixel devices have a higher crosstalk probability due to the shorter travel distance of the photons [41]. Several producers reduce crosstalk by adding trenches between the pixels [41].

Pulse linearity and dynamic range - The dynamic range for simultaneously incident photons is determined by the number of pixels. The saturation behaviour of SiPMs can be determined from Equation (4.30). In practice, deviations from linearity usually start at an occupancy of approximately 60 % of the pixels. Typically the dynamic range of SiPMs is in the range of 10^2 to 10^3 , however, recently devices with values up to 10^5 have been also developed [40].

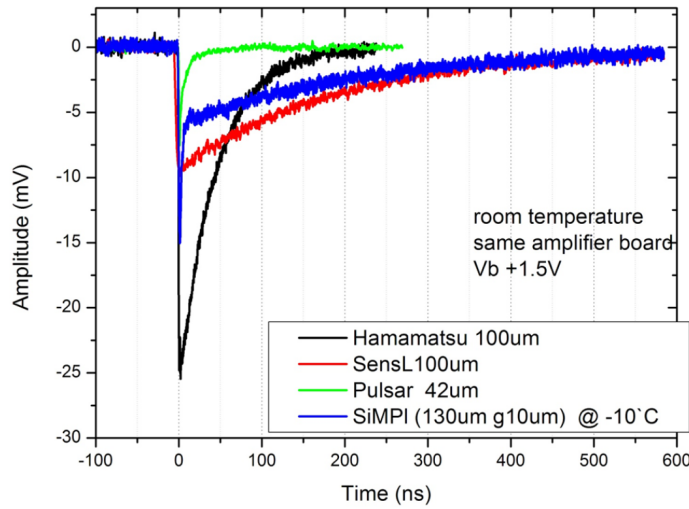


Figure 4.17: Comparison of single pixel pulses from SiPMs of different producers, measured at room temperature with the same over-voltage and amplifier [41].

For light pulses with a duration much larger than the pixel recovery time, an effective dynamic range, depending on the single pixel dead time can be defined. Since a shorter dead time allows a pixel to be fired multiple times during the pulse, the effective dynamic range increases with shorter pixel dead times.

Time response - The development of the Geiger discharge is, due to the very thin width of the depletion region in the semiconductor, very fast (few hundred ps [38]).

- **Rise time and recovery (fall) time.** Typical rise times of SiPMs are in the order of 1 ns. The fall or recovery time for a single pixel is the time needed to recharge the pixel capacitance, C_{pix} . It is determined by the time constant $\tau = C_{pix} \cdot R_q$, where R_q is the quenching resistor. Typical values for τ are widely spread, in the range of 5 ns up to a few hundred μ s. Figure 4.17 shows a comparison of single pixel pulses from SiPMs of different producers, measured at room temperature with the same over-voltage and amplifier [41].
- **Transit time spread (TTS).** Due to the microscopic dimension of SiPMs, the TTS, or jitter is very small. Typical values lie in the range of hundreds of picoseconds. Values down to 50 ps are possible.

5 Cherenkov Fibers

5.1 Cherenkov Effect

In a dielectric medium with refractive index n , a charged particle moving with velocity v can exceed the phase velocity of light $v_p = c/n$ inside the medium. In this case the particle emits electromagnetic radiation, known as Cherenkov radiation.

The Cherenkov radiation is the result of a time dependent dipole field created when the charged particle polarizes atoms or molecules locally in the medium. If the particle is slower than the local velocity of light, the dipoles are arranged symmetrically around a particle track and the resulting integrated dipole field is zero. However, If $v > c/n$, the symmetry is broken and there is a net dipole field resulting in the emission of electromagnetic radiation.

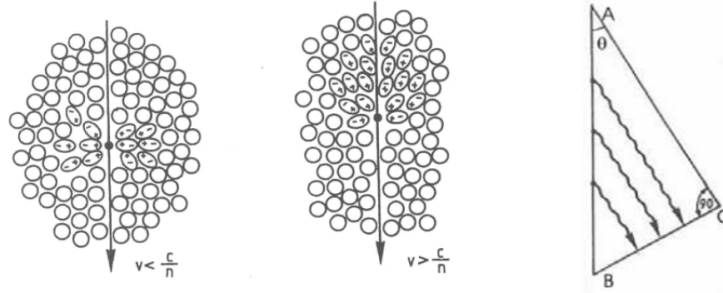


Figure 5.1: Left: Illustration of the polarization of a medium due to a charged particle traveling above or below the speed of light in this medium [42]; Right: Illustration of the direction of the emitted photons

The characteristic emission angle θ_c of the Cherenkov light with respect to the direction of the particle track can be derived from a simple consideration of the positive interference of photons at an angle of θ_c as shown in Figure 5.1. While the particle travels the distance $AB = t\beta c$ in the time t , the photon covers the distance $AC = tc/n$ and the emission angle is given by

$$\cos \theta_c = \frac{1}{\beta n} \quad (5.1)$$

where $\beta = v/c$. Due to the fact that real media are always dispersive, n is a function of wavelength. However, it can be approximated by a constant in certain spectral regions (see 5.2). e.g. for quartz by $n \approx 1.46$. From (3.1), Cherenkov photons are emitted at a fixed angle θ_c with equal probability in the azimuthal direction. They, therefore, propagate on a cone around the direction of the charged particle with included angle θ_c . At the production

Particle	E_0 [MeV]	$E_{kin,th}$ [MeV]	$E_{kin,\beta=0.999}$ [GeV]
e^-, e^+	0.511	0.186	0.011
μ^-, μ^+	105.5	38.5	2.26
p^+, p^-	938.2	341.8	20.05
π^+, π^-	139.6	50.9	2.98
K^+, K^-	493.7	179.9	10.55

Table 5.1: A list of charged particles typically found in a high energy beam loss shower, their rest mass energy E_0 , the threshold kinetic energy $E_{kin,th}$ for the Cherenkov effect in fused silica and the kinetic energy $E_{kin,\beta=0.999}$ corresponding to the listed particles with $\beta = 0.999$.

threshold the radiation is emitted in forward direction and the emission angle increases with the speed of the particle. Thus, the threshold value β_{th} for the production of Cherenkov radiation follows from (5.1) by setting the Cherenkov emission angle to zero:

$$\theta_c \equiv 0 \rightarrow \beta_{th} = \frac{1}{n} \quad (5.2)$$

The emission angle takes its maximum for $\beta \rightarrow 1$:

$$\theta_{c,max} = \arccos\left(\frac{1}{n}\right) \quad (5.3)$$

For quartz, $\theta_{c,max}$ is obtained to be $\approx 47^\circ$.

For considerations in some of the following chapters the kinetic energy thresholds $E_{kin,th}$ of various charged particles were calculated. These are determined by considering the relativistic kinetic energy of the particle, given by:

$$E_{kin} = E_{tot} - E_0 = mc^2\gamma - mc^2 \quad (5.4)$$

where E_{tot} is the total relativistic energy, E_0 is the particle rest mass energy and $\gamma = 1/\sqrt{1-\beta^2}$ is the relativistic Lorentz factor. Therefore, the threshold energy is given by

$$E_{kin,th} = mc^2 \left(\frac{1}{\sqrt{1-\beta_{th}^2}} - 1 \right) = mc^2 \left(\frac{n}{\sqrt{n^2-1}} - 1 \right) \quad (5.5)$$

In Table 5.1 the values for fused silica ($n \approx 1.47$) for relevant particles are shown.

The energy loss, dE , per unit path length, dL , of a particle due to the emission of Cherenkov radiation is described by the Frank-Tamm formula [43], originally expressed in the *cgs*-system in units of ergs/cm:

$$\frac{dE}{dL} = \frac{e^2}{c^2} \int_{\beta n(\omega) > 1} \left(1 - \frac{1}{\beta^2 n(\omega)^2} \right) \omega d\omega \quad (5.6)$$

Here e is the elementary charge and $\omega = 2\pi c/\lambda$ is the angular frequency of the emitted photons. The integration is performed over values of ω for which $\beta n(\omega) > 1$, such that (5.1)

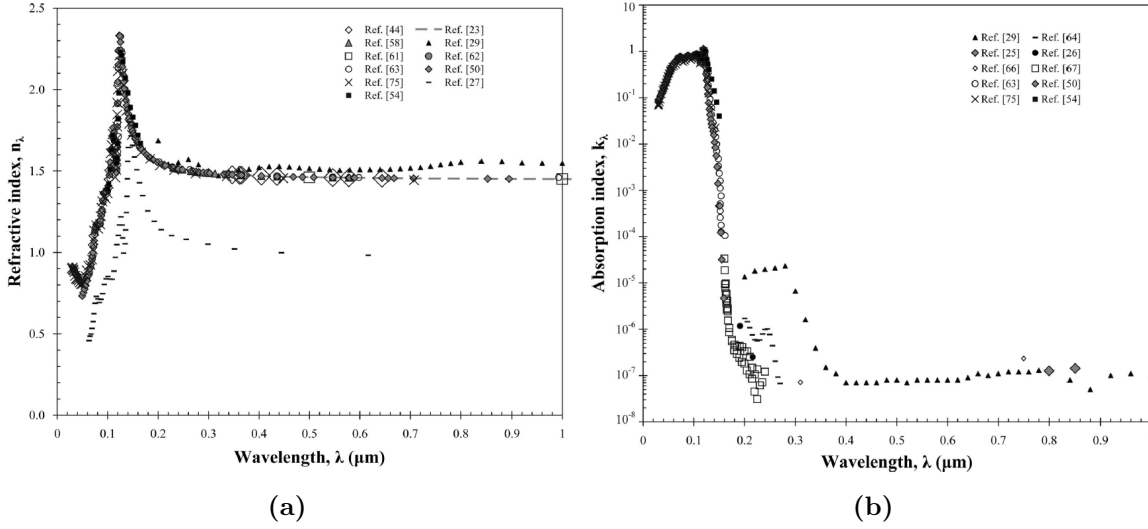


Figure 5.2: (a) Real n and (b) imaginary k parts of the complex refractive index of silica glass as reported in the literature [44].

is always satisfied. Since there is no frequency cut-off for the integral of Equation (5.6), the emitted radiation initially seems to be infinite. However, for most of the transparent media the condition $n(\omega) > 1/\beta$ is not met for the entire spectral range. As shown in Figure 5.2, in the X-ray region in particular $n(\omega)$ is always smaller than 1 and radiation is therefore suppressed. As a result, in practice, the emitted energy is always finite.

From (5.6) the number of photons dN_{ph} emitted per unit path length dL , can be expressed as a function of the wavelength λ :

$$\frac{dN_{ph}}{dL} = 2\pi\alpha z^2 \int_{\beta n(\lambda) > 1} \left(1 - \frac{1}{\beta^2 n(\lambda)^2}\right) \frac{d\lambda}{\lambda^2} \stackrel{n \approx \text{const.}}{\approx} 2\pi\alpha z^2 \sin^2 \theta_c \int_{\beta n > 1} \frac{d\lambda}{\lambda^2} \quad (5.7)$$

where α is the fine structure constant and $z \cdot e$ is the charge of the particle. Through similar considerations one can derive further relations for the double differential spectral distributions:

$$\frac{d^2 E}{dL d\omega} \propto \omega$$

$$\frac{d^2 E}{dL d\lambda} \propto \frac{1}{\lambda^3}$$

$$\frac{d^2 N_{ph}}{dL d\omega} \propto \text{const.}$$

$$\frac{d^2 N_{ph}}{dL d\lambda} \propto \frac{1}{\lambda^2}$$

For quartz there are approximately 100 photons produced per mm by a charged particle with $\beta \approx 1$. The emission of Cherenkov light is in general a very small contribution to the total energy loss of a charged particle. For example, the energy loss due to Cherenkov emission of a particle with $\beta \approx 1$ in quartz is of the order of 1 keV/cm, whereas a minimum ionizing particle (MIP) loses about 4.5 MeV/cm due to ionization loss.

5.2 Cherenkov Effect in Optical Fibers

By using an optical fiber as a Cherenkov light radiator, the generated light can be guided to a photodetector at the end of the fiber. The light is trapped and guided by means of total reflection at the interface of the core and cladding of the fiber. Only for a fraction of the produced light, are the conditions for trapping met.

In the framework of this thesis, a model, based on ray theory, was developed. It allows to calculate the light yield reaching the photo detector per particle crossing the fiber and furthermore the dispersion of the Cherenkov light signal. Together with the simulated loss scenarios for the CLIC two beam modules described in section 7.2, it allows for the estimation of the integrated light yield for each loss and its arrival time structure at both ends of the fiber. The following points are considered for the model:

1. The light yield Y caused by the passage of a single charged particle through the fiber core.
2. The trapping probability P_t for the emitted photons in connection with the directionality of the Cherenkov effect.
3. The influence ϵ_{att} of attenuation on the Cherenkov light spectrum.
4. The coupling efficiency η_{coupl} between the fiber and the photon detector.
5. The photon detection efficiency η_{PDE} (PDE) of the photon detector.
6. The dependency ϵ_d of the light yield generated by an extended charged particle beam (i.e. with a dimension much larger than the fiber diameter) on the diameter of the fiber.
7. The possible longitudinal resolution of the position of the beam loss in connection with the dispersion of the Cherenkov light signal.

As a result of points 1.-5., the average number of photons detected $N_{ph,det}$ per charged particle crossing the fiber can be expressed as

$$N_{ph,det} = Y * P_t * \epsilon_{att} * \eta_{coupl} * \eta_{PDE} \quad (5.8)$$

Similar models with an emphasis on one or several of the above points have been developed previously [45, 28, 46, 47, 48]. In particular, the geometry described in [28], is used as a basis for all following derivations.

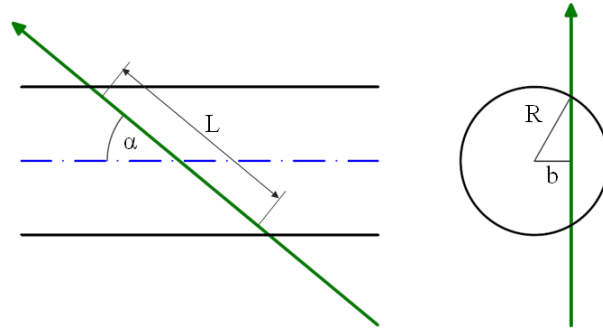


Figure 5.3: Schematic drawing of a charged particle (green arrow) crossing the fiber core

5.2.1 Model

5.2.1.1 Light yield

To obtain the light yield generated by the passage of a single charged particle through the fiber core, Equation (5.7) has to be integrated over the tracklength of the particle inside the fiber and the relevant Cherenkov photon wavelength range. This range can be limited by the photon detection efficiency (PDE) of the considered photon detector and the transmittance of the fiber core material. For these reasons the wavelength interval $\lambda_1 - \lambda_2$ is set to 200 - 900 nm in all further calculations.

The length, L , of the trajectory of the particle within the fiber core can be expressed as:

$$L = \frac{2\sqrt{R^2 - b^2}}{|\sin \alpha|} \quad (5.9)$$

Here R is the fiber radius, α is the incident angle between the particle track and the fiber axis and b is the impact parameter, the distance of the closest approach between the particle and the fiber axis (Figure 5.3). The light yield Y for a single particle crossing the fiber is then given by:

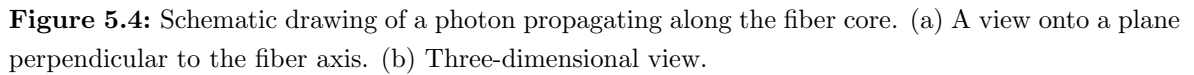
$$Y \approx \frac{2\pi}{137} \frac{2\sqrt{R^2 - b^2}}{|\sin \alpha|} \left(1 - \frac{1}{\beta^2 n^2}\right) \frac{\lambda_2 - \lambda_1}{\lambda_2 \lambda_1} \quad (5.10)$$

5.2.1.2 Trapping probability

Three major cases for the trapping probability can be distinguished:

1. Probability P_t for the photons to be trapped:

The Cherenkov photons generated are trapped and transported if the condition for total reflection at the intersection between the core and the cladding of the fiber is met. This condition can be described by the total angle ξ between the normal to the core boundary at the point of reflection and the photon track. From Snellius's law it follows


$$\xi \geq \xi_c = \arcsin\left(\frac{n_{cl}}{n_{co}}\right) \quad (5.11)$$
$$\xi_{test} = \xi - \xi_c \geq 0 \quad (5.12)$$
$$\cos \xi = \cos \eta \sin \psi \quad (5.13)$$

2. The probability P_e for the photons to be trapped, with a successive exit at the fiber end face:

$$\psi \leq \psi_{c,e} = \arcsin\left(\frac{n_{out}}{n_{co}}\right) \quad (5.14)$$
$$\psi_{test,e} = \psi_{c,e} - \psi \geq 0 \quad (5.15)$$

where $\psi_{c,e}$ is the critical ψ for an exit of the photon and n_{out} is the refractive index of the medium into which the light exits. For all following calculations this medium was

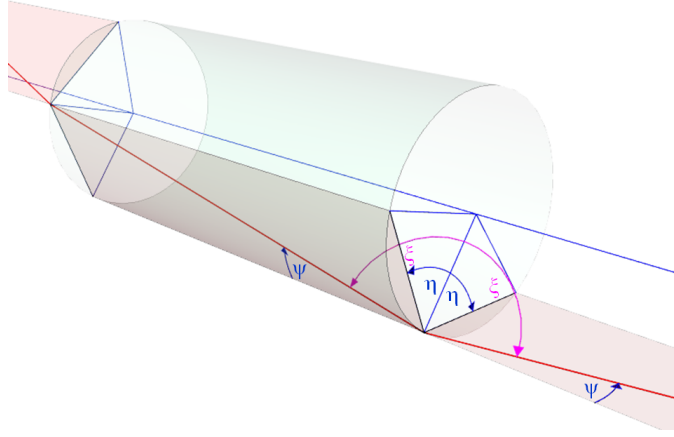


Figure 5.5: Schematic drawing of a photon propagating along the fiber core. The photon is indicated as a red line. If the condition in (5.14) is met, both the longitudinal propagation angle ψ and the azimuthal propagation angle η are preserved at each reflection. Consequently, the photon is mirrored at each reflection into a new plane, indicated in light red.

assumed to be air with $n_{out} \approx 1$.

3. The probability $P_{e,n}$ for the photons to be trapped, with a successive exit within the nominal acceptance cone at the fiber end face:

Of the remaining photons exiting the fiber, only a fraction exits within the nominal acceptance cone. For this point, in addition to (5.13), the condition

$$\psi \leq \psi_{c,e,n} = \arccos\left(\frac{n_{cl}}{n_{co}}\right) \quad (5.16)$$

or

$$\psi_{test,e,n} = \psi_{c,e,n} - \psi \geq 0 \quad (5.17)$$

must be satisfied.

For the calculation of the trapping probability, the relation between the angles ξ , η and ψ , defining the conditions for the probabilities listed above, and the directionality of the Cherenkov effect has to be derived. For this derivation the geometry presented in [28] is followed.

Figure 5.6 shows a schematical drawing of the geometry of a single Cherenkov photon emitted by a traversing charged particle. The particle trajectory, indicated in green, with respect to the fiber is characterized by the impact parameter b and the angle α between the particle track and the fiber axis. At point P, defined by b and x , the photon is emitted along the surface of the Cherenkov cone with half-angle θ_c . The direction of emittance along the cone is described by the azimuthal angle ω . ψ and η are then given by:

$$\cos \psi = \cos \alpha \cos \theta_c - \sin \alpha \sin \theta_c \cos \omega \quad (5.18)$$

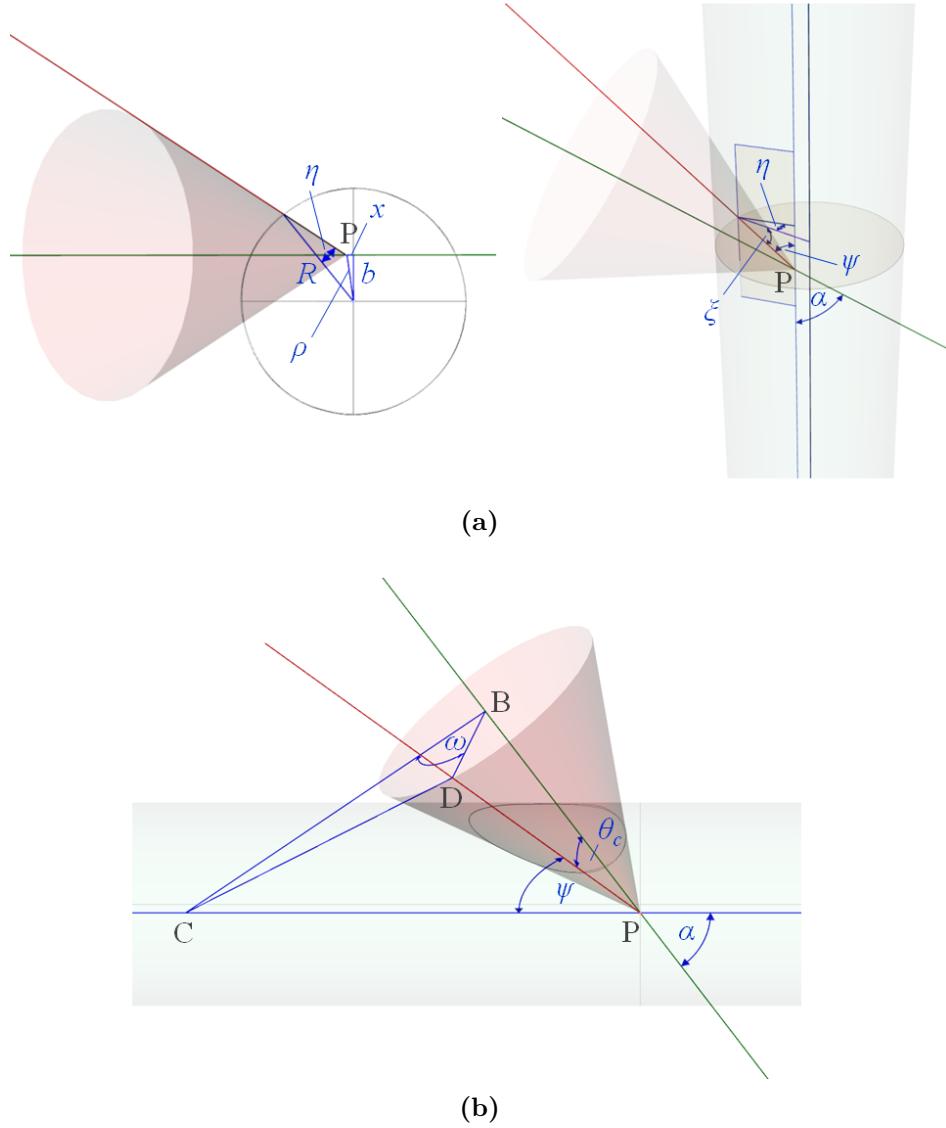


Figure 5.6: Different views of the geometry related to the emission of a single Cherenkov photon (red line) by a particle (green line) crossing a cylindrical fiber. The charged particle is characterized by the impact parameter b and the incident angle α between the fiber longitudinal axis and the particle track. At point P the photon is emitted along the surface of the Cherenkov cone with a semi-opening angle of θ_c . The azimuthal angle ω describes the direction of emittance along the cone surface.

(a) Left: Projection onto a plane perpendicular to the fiber axis. The azimuthal propagation angle η is the angle between the projection of the photon track and the radius of the fiber. Point P, the position of emittance, is defined by b and x . Right: Three-dimensional view. The angle ψ is the longitudinal propagation angle.

(b) Three-dimensional view to illustrate the relation between ξ , η and ψ , expressed in (5.13)

and

$$\sin \eta = \frac{\rho}{R} \left(\arctan \frac{\sin \theta_c \sin \omega}{\cos \theta_c \sin \alpha + \cos \omega \sin \theta_c \cos \alpha} + \arcsin \frac{b}{\rho} \right) \quad (5.19)$$

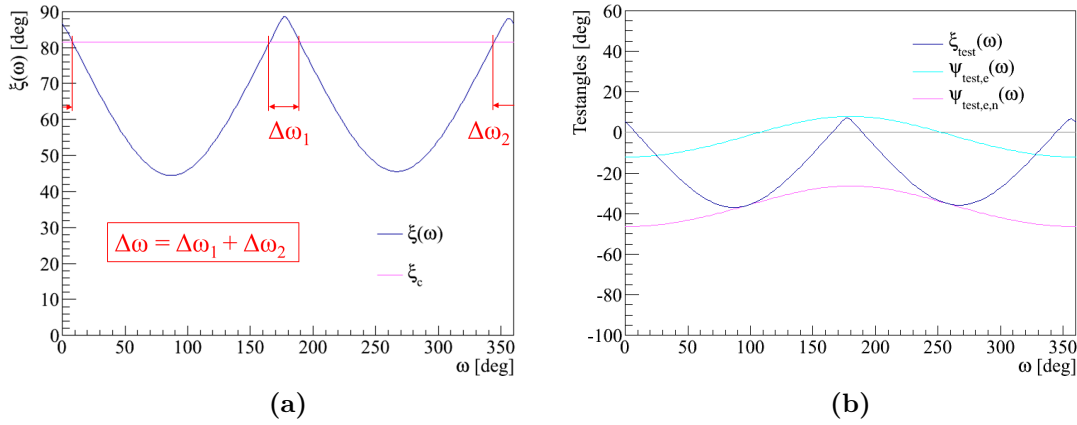


Figure 5.7: (a) An example of $\xi(\omega)$ for randomly chosen variables α , b and x . If the Cherenkov photon is emitted into the region $\Delta\omega$ where $\xi(\omega) > \xi_c$, it gets trapped. (b) The test angles defined in Equations (5.12), (5.15) and (5.17) for the same point as used in (a).

Using Equations (5.18), (5.19) and (5.13) it is possible to calculate whether the conditions 5.11, 5.14 and 5.16 are satisfied for a single photon. To summarize, the geometry related to the production of a single Cherenkov photon can be completely described by the following variables:

- Fiber properties: n_{co} , $n_{cl} \leftrightarrow NA$
- Particle properties: α , β , b
- Photon properties: ω and position of emittance (b , x)

To calculate the average trapping probability, one has to consider that the direction of emittance of the photon along the Cherenkov cone is a uniform distribution in ω . Consequently, for a given fiber, position of emittance, and crossing particle, the angles ξ and ψ are a function of ω only. Figure 5.7a shows an example of $\xi(\omega)$. If the photon is emitted into the region $\Delta\omega$ where $\xi(\omega) > \xi_c$, it is trapped. By dividing $\Delta\omega$ by 2π , the trapping probability for this single event is obtained.

When ξ and ψ are a function of ω , the test angles ξ_{test} , $\psi_{test,e}$ and $\psi_{test,e,n}$ are also a function of ω . By plotting the results for all three angles (Figure 5.7b), the regions of ω , where the conditions for the three cases of trapping are satisfied, can be determined.

If the fiber is placed in a beam loss particle shower, all impact parameters b are equally likely. Averaging over all possible impact parameters b and positions of emittance x , while keeping the incident angle of the particle α stepwise constant, results in the average trapping probability P_t as a function of α . Similar considerations, using the conditions (5.14) and (5.16) provide the solutions for P_e and $P_{e,n}$.

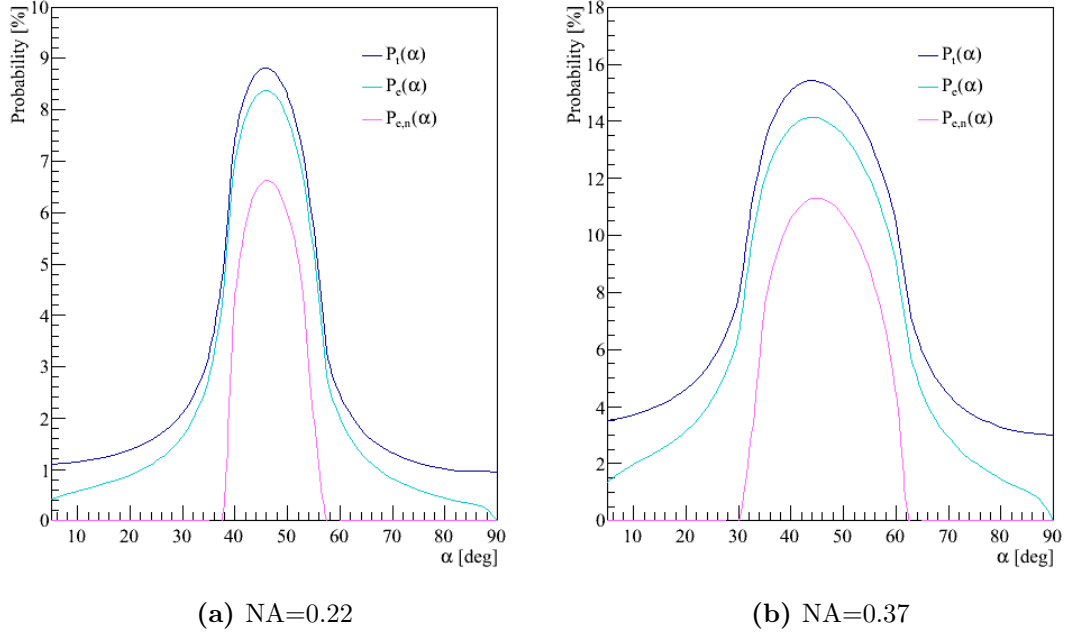


Figure 5.8: Results for the photon trapping probabilities as a function of α , for $\beta = 1$ and $z = 1$ particles, in a quartz fiber with (a) NA=0.22 and (b) NA=0.37. The medium outside the fiber is assumed to be air ($n \approx 1$). The upper blue curves show the probability P_t for the photons to be trapped in the fiber. The central lines show the probability P_e for photons to be trapped, with a following exit at the fiber end face. The lower pink lines show the probability $P_{e,n}$ for photons to be trapped, with a subsequent exit within the nominal exit cone.

For the probability $P_{e,n}$ there is also an analytical solution independent of the impact parameter and the position of photon creation. The derivation is shown in [46] and can be expressed as:

$$P_{e,n} = \frac{1}{\pi} \arccos \left(\frac{\beta \sqrt{n_{co}^2 - NA} - \cos \alpha}{\sin \alpha \sqrt{\beta^2 n_{co}^2 - 1}} \right) \quad (5.20)$$

Figure 5.8 shows the solutions for particles with $\beta = 1$ and quartz fibers with a numerical aperture of NA=0.22 and NA=0.37, respectively. In both cases there is a significant maximum at an angle corresponding to the Cherenkov angle in quartz. This is a consequence of the fact that $\Delta\omega$ reaches a maximum if $\alpha \approx \theta_c$, as then a large part of the Cherenkov cone surface is directed nearly in parallel to the fiber axis. The strong tails of the curves for $P_t(\alpha)$ and $P_e(\alpha)$ result from spiralling photons which follow skew ray paths. These photons are generated by particles with high impact parameters b and have large longitudinal and azimuthal propagation angles ψ and η .

Additionally, one can see the large influence of the numerical aperture. The peak becomes both wider and higher, and the integrated probability for a NA=0.37 fiber is about three times as large as for a NA=0.22 fiber. According to the analytic expressions used to build the model, the trapping probabilities are independent of the diameter d of the fiber.

Trapped light yield

The average photon yield caused by the passage of one single charged particle as a function of α can be determined by convoluting the average trapping probability with the $1/|\sin \alpha|$ dependency of the Cherenkov light generation.

$$Y_t = Y * P_t \quad (5.21)$$

The results, for fibers with a numerical aperture of NA=0.22 and NA=0.37, are shown in Figure 5.9. This distribution also shows a peak at approximately the Cherenkov angle, resulting from the distribution of the trapping probability. The blue, upper curves show the yield of the trapped photons which will be transported along the fiber. This curve additionally has a steep rise at low angles, which stems from the large number of photons produced at these small angles, multiplied by the small trapping probability. However, these photons are very hard to couple into a photon detector due to their previously described large propagation angles ψ and η . Depending on the geometry and method used to couple the fiber to the photon detector, a part will be reflected back at the end face. Of the remaining part, a fraction will be refracted with too large exit angles. This will make it impossible to reach the active surface of the photon detector. The central, cyan curves show the example distribution of the photon yield exiting the fiber into air ($n \approx 1$). The lower, pink line shows the distribution for the photons exiting the fiber within the nominal exit cone. For these photons, ψ is restricted by (5.17), and consequently the coupling efficiency is very high.

For the photons exiting the fiber within the nominal exit cone, an analytical solution for $Y_{e,n}$ can be obtained by combining (5.20) and (5.10) to:

$$Y_{e,n} \approx \frac{R\pi}{137|\sin \alpha|} \left(1 - \frac{1}{\beta^2 n^2}\right) \frac{\lambda_2 - \lambda_1}{\lambda_2 \lambda_1} \arccos \left(\frac{\beta \sqrt{n_{co}^2 - NA} - \cos \alpha}{\sin \alpha \sqrt{\beta^2 n_{co}^2 - 1}} \right) \quad (5.22)$$

Figure 5.10 shows the photon yield $Y_{e,n}$ as a function of the charged particle properties α and β . The 'ridge'-shaped function is symmetric with respect to the angle $\alpha = 90^\circ$. Within a range of $0 \leq \alpha \leq 90^\circ$, the maximum of the "ridge" is found at values for α , which each correspond to the Cherenkov emission angles θ_c for values of β according to (5.1):

$$Y_{e,n,max}(\alpha, \beta) : \quad \alpha \equiv \theta_c = \arccos \frac{1}{\beta n} \quad (5.23)$$

The two 'ridges' in Figure 5.10 have an approximately constant maximum until β approaches β_{th} , and α approaches zero or 180° . There, the maximum of the function $Y_{e,n,max}(\alpha, \beta)$ goes to infinity. In theory, this happens since the path length of the particle within the fiber goes towards infinity, and the Cherenkov emission angle, θ_c , is zero for $\beta = \beta_{th}$. Therefore, the conditions for total reflection would be met for all generated photons and, consequently, all would be trapped inside the fiber. In practice, however, a track parallel to the fiber ($\alpha = 0^\circ$ or 180°) is not possible. Therefore, the results of the model only can be taken as an approximation in the parameter regions where $\beta \rightarrow \beta_{th}$ and $\alpha \rightarrow 0^\circ$ or $\alpha \rightarrow 180^\circ$.

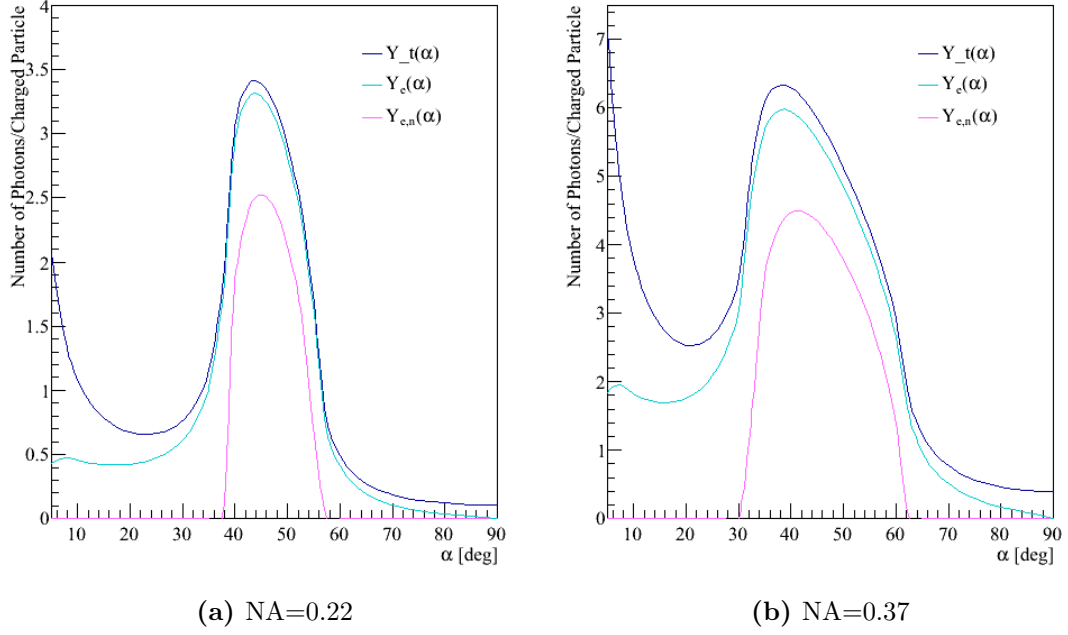


Figure 5.9: Results for the photon yield per incident charged particle as a function of α for $\beta = 1$ and $z = 1$ particles, in a quartz fiber with a diameter of $d=365\mu m$ and (a) NA=0.22 and (b) NA=0.37. The medium outside the fiber is assumed to be air ($n \approx 1$). The upper blue curves show the yield Y_t of the photons which are trapped in the fiber. The central lines show the yield Y_e of photons which are trapped and able to exit the fiber at the end face. The lower pink lines show the yield $Y_{e,n}$ of the trapped photons which are able to exit the fiber within the nominal exit cone.

5.2.1.3 Attenuation

As described in Section 4.1.2, in the UV/Vis spectral range, the most relevant wavelength range for Cherenkov fiber applications, Rayleigh scattering is the dominant contribution to attenuation. For the model described in this thesis, the attenuation coefficient resulting from Rayleigh scattering is therefore used as an approximation for the overall influences of attenuation on the Cherenkov light spectrum.

Recalling Equation (4.23) and (4.22), the attenuation factor mentioned in Equation (5.8), ϵ_{att} , can be expressed as:

$$\epsilon_{att} = \frac{P(L)}{P(0)} \approx 10^{-\frac{0.83 \cdot L_{fib} [km]}{10 \cdot \lambda^4 [\mu m]}} \quad (5.24)$$

By combining the equation above with Equation (5.7), the differential Cherenkov light yield after a propagation of a distance L_{fib} through a fiber, per single charged particle, can be approximated by:

$$\frac{dN_{ph}}{d\lambda} \approx 2\pi\alpha z^2 L \sin^2 \theta_c \cdot P_t \cdot \frac{10^{-\frac{0.83 \cdot L_{fib} [km]}{10 \cdot \lambda^4 [\mu m]}}}{\lambda^2} \quad (5.25)$$

The factor L occurring in the above equation is thereby the track length of the charged particle within the medium. For a cylindrical fiber, L is fully defined by Equation (5.9).

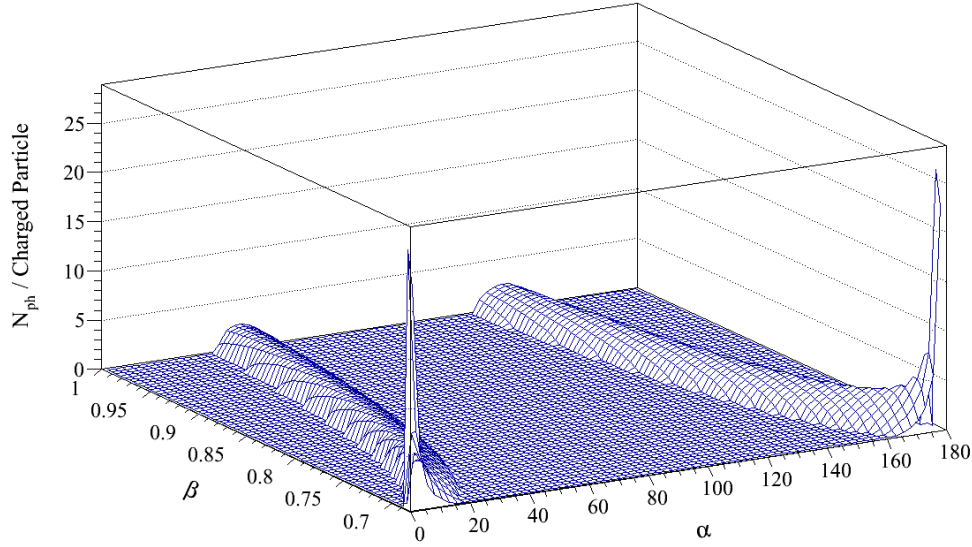


Figure 5.10: Number of photons exiting the fiber within the nominal exit cone per charged particle, as calculated by Equation (5.22), as a function of the impact angle α and the relative velocity $\beta = v/c$.

Figure 5.11a shows the influence of attenuation on the Cherenkov light spectrum. The upper, green curve shows the characteristic Cherenkov light production spectrum. The other curves show the residual spectra after a propagation through a fiber with length L_{fib} . The fiber lengths corresponding to the colors are denoted in the legend of the plot. It is clearly visible that the low-wavelength part of the spectrum becomes less and less significant with increasing fiber length. In particular for L_{fib} greater than 100 m, the blue/green part of the spectrum is degenerated.

The integral over the spectra results in the light yield reaching the far end of the fiber. For example, considering the wavelength range between 200 and 900 nm, after 4 m of fiber the signal is reduced by 10 %, after 50 m by 45 %, after 100 m by 65 %, and after 300 m by 80 %.

As stated above, these results are only approximations since the contribution of extrinsic absorption bands to attenuation are neglected. However, they show that it is important to consider attenuation effects with regard both to the choice of the photodetector and its spectral response (PDE), and to consider the feasible fiber length for a Cherenkov BLM. For a particular fiber, the analysis on the influence of attenuation can be enhanced by using the nominal attenuation dependency on the wavelength.

5.2.1.4 Photon detection efficiency

As discussed in Section 4.3, the photon detection efficiency (PDE), or η_{PDE} , of photodetectors is strongly dependent on the wavelength. Since there is a great variety in the wavelength range covered by different photodetectors, a generic approximation is not useful, and each case has to be considered separately.

From Equation (5.25), the detected differential Cherenkov light yield after a propagation

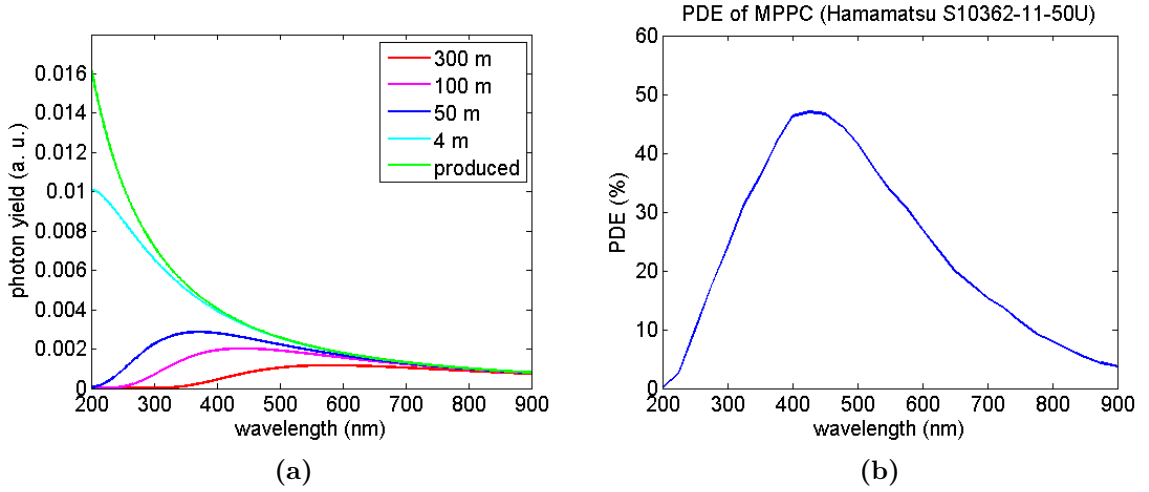


Figure 5.11: (a) Influence of attenuation on Cherenkov light spectrum. The curves shown represent the residual part of the spectrum after a propagation through a fiber with length L_{fib} . The length L_{fib} corresponding to the color is shown in the legend. (b) Photon detection efficiency (PDE) of the Hamamatsu S10362-11-50U MPPC.

of a distance L_{fib} through a fiber, per single charged particle, can be approximated by:

$$\frac{dN_{ph}}{d\lambda} \approx 2\pi\alpha z^2 L \sin^2 \theta_c \cdot P_t \cdot \frac{10^{\frac{0.83 \cdot L_{fib}[\text{km}]}{10 \cdot \lambda^4[\mu\text{m}]}}}{\lambda^2} \cdot \eta_{PDE}(\lambda) \quad (5.26)$$

As an example, Figure 5.11b shows the PDE of the Hamamatsu S10362-11-50U MPPC, which was used for one of the beamtests discussed in Chapter 6. Figure 5.12a shows both the influence of attenuation and the photon detection efficiency on the initial Cherenkov light spectrum. The blue dots show the characteristic Cherenkov light production spectrum. The red dots show the attenuated spectrum due to a fiber length of $L_{fib} = 4$ m. The cyan dots show the part of the spectrum that is finally detected, assuming the PDE of the Hamamatsu S10362-11-50U MPPC. For this example, only approximately 21 % of the produced photons are detected.

Figure 5.12b shows the corresponding results for $L_{fib} = 100$ m. Compared to the results for $L_{fib} = 4$ m, it can be observed that, due to attenuation, the low-wavelength part of the spectrum of the Cherenkov light reaching the far end of the fiber is degenerated. As a result, the spectral response of the photodetector is no longer fully exploited. For such long fibers, a detector with a peak-PDE at higher wavelengths would therefore be a better choice. Furthermore, a focus on the detection of the higher-wavelength spectral range would lead to less variation in the detected Cherenkov light yield due to the lower influence of the attenuation effects. On the other hand, the light yield would be substantially lower in this range, which would have to be compensated by larger fiber diameters.

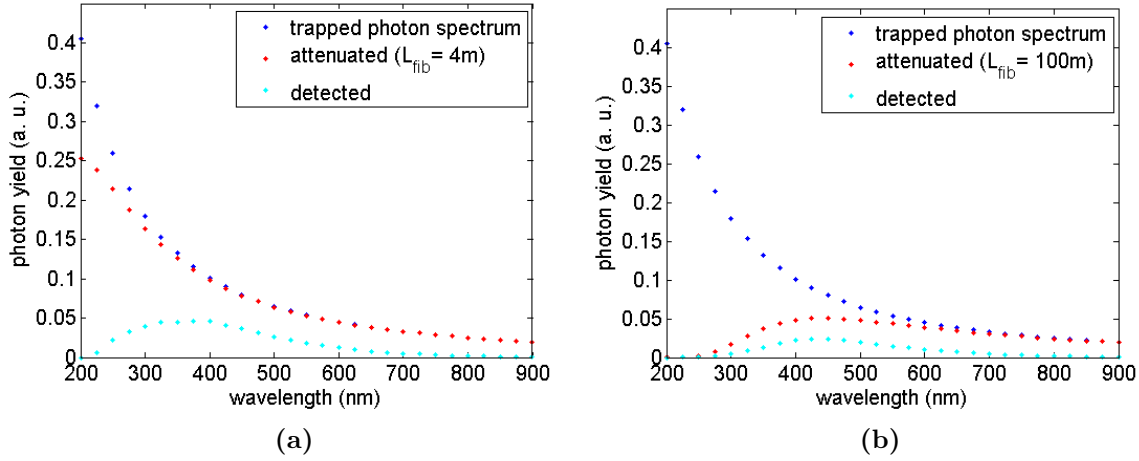


Figure 5.12: Influence of attenuation and the photon detection efficiency on the initial Cherenkov light spectrum. The blue dots show the characteristic Cherenkov light production spectrum. The red dots show the attenuated spectrum due to a fiber length L_{fib} . The cyan dots show the part of the spectrum that is finally detected, assuming the PDE of the Hamamatsu S10362-11-50U MPPC as shown in Figure 5.11. (a) Results for $L_{fib} = 4$ m, and (b) results for $L_{fib} = 100$ m

5.2.1.5 Coupling efficiency

The optical coupling efficiency η_{coupl} between the fiber and the photodetector depends on the geometry of the connection, the acceptance angles of the fiber and the type of optical connection being used. There are two generic types of connections: A 'wet' connection, consisting of optical grease, or a small air gap. Wet connections provide a better coupling onto the sensitive surface of the PD since the refractive index of the grease can be adjusted in such a way that the rays exiting the fiber do not, or only in a controlled way, experience defraction. On the other hand, attaching with air gaps is easier to achieve and more reliable.

Considering an attachment with an air gap, a fraction of the photons will exit the fiber with too large propagation angles ψ and η and will not be detected. Consequently, the distance between the fiber end face and the PD has to be adjusted in such a way that at least all photons exiting the fiber within the nominal exit cone are detected. For SiPMs the distance has to be chosen according to a compromise between a shorter distance and therefore higher coupling, and a larger distance and therefore a larger irradiated area on the active surface, i.e. a larger number of available pixels.

5.2.1.6 Fiber diameter dependency of light yield

In the model described in this thesis, the photon yield resulting from an extended beam (i.e. beam dimensions much larger than the fiber core diameter) scales by the square of the fiber core diameter. This is a result of the following considerations:

1. The photon yield for a single charged particle crossing a fiber is proportional to its track length L within the fiber (cf. Section 5.2.1.1). From Equation (5.9), and as indicated

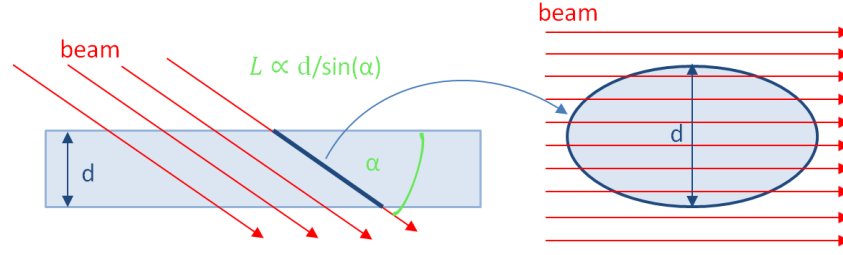


Figure 5.13: Influence of the fiber diameter on the Cherenkov light yield for the case of an extended particle beam impinging upon a fiber. **Left:** Horizontal cross section through the fiber core. The Cherenkov light yield for a single charged particle scales with its track length L within the fiber. **Right:** Vertical cross section through the fiber core. The number of particles out of an extended beam crossing the fiber scales with the diameter of the fiber.

in Figure 5.13, the track length is proportional to the fiber diameter.

2. As illustrated in Figure 5.13, for an extended beam the number of particles crossing the fiber is proportional to the fiber diameter.

Further dependencies of the light yield on the fiber diameter are not expected. However, in [46, 47] it is stated that the photon yield for a 'collimated' beam scales by the cube of the fiber diameter. Since, after comprehensive considerations, no reason for the additional third power could be deduced, a dedicated beamtest has been performed. This beam test and its results are discussed in detail in Chapter 6.

5.2.1.7 Dispersion and photon propagation velocities

Following the ray approach to model the capture and transport of Cherenkov photons, and assuming the speed of light (photons) $v = c/n_{co}$ to be constant, the distribution of the photon propagation velocity along the longitudinal axis of the fiber can be calculated. This distribution will be a result of the coupling behaviour of the Cherenkov light into the permitted propagation modes for different α , and according to the modes, the different path lengths towards the end of the fiber. The cosine of ψ characterizes the ratio between the shortest possible path along the fiber axis and the actual path taken by the photon.

Figure 5.14a shows the velocity distribution for the trapped Cherenkov light. The velocities are defined in the way that a positive velocity represents light traveling to the forward (downstream) end of the fiber, whereas a negative velocity represents light propagating to the backward (upstream) end. The upper, enveloping curve shows the result for a simulation in which all incident angles α of the particles ($\beta = 1$) crossing the fiber (NA=0.37) were taken to be equally likely. The distribution has a strong peak at velocities close to $v = c/n_{co}$ and a long tail towards lower velocities. The distributions below that curve, highlighted by different colors, are calculated by restricting α to intervals of 5° . For instance, the green line shows the results for the interval $1^\circ \leq \alpha \leq 5^\circ$. The velocities of the large number of photons generated within this interval all lie within a very narrow band between ≈ 12.5 -15.5 cm/ns

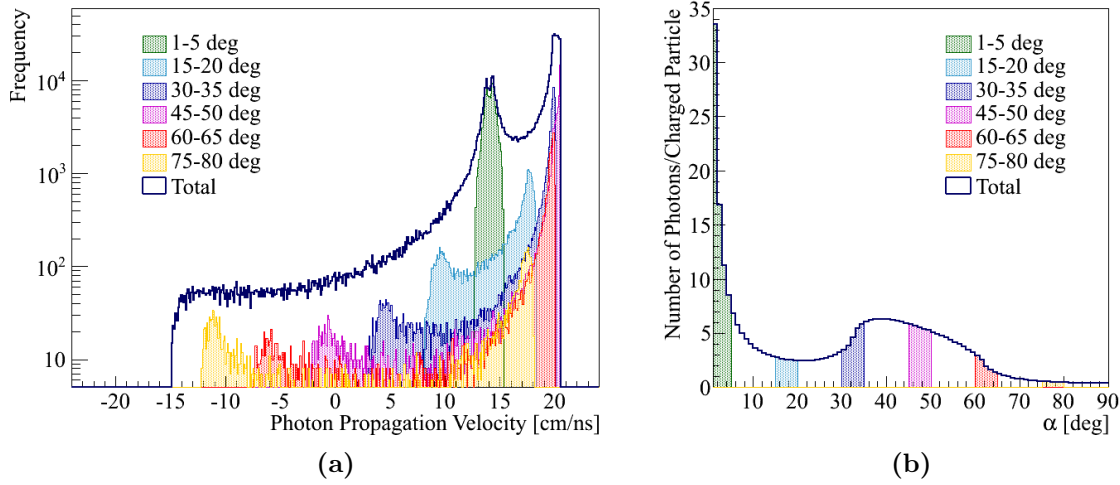


Figure 5.14: (a) Simulated photon propagation velocity along the longitudinal axis of a fiber with $NA=0.37$, for incident particles with $\beta = 1$. The colored distributions each represent the results obtained if all incident angles within the according ranges of α are assumed to be equally likely. The upper, enveloping line shows the total sum for $1^\circ \leq \alpha \leq 90^\circ$. (b) Photon yield per incident charged particle as a function of α , as also shown in Figure 5.9b. The angular ranges used in (a) are indicated by the corresponding colors.

and contribute significantly to the second peak of the overall distribution in that range. This is a further evidence for the fact that all these photons are highly spiralling, corresponding to large values of ψ . In contrast to that, the purple line shows the distribution for incident particles with $45^\circ \leq \alpha \leq 50^\circ$. It peaks at the largest possible velocity, which indicates that the majority of the generated photons propagates along paths described by a very small ψ . Particles with $\alpha \leq 45^\circ$ start producing photons contributing to the negative part of the distribution, until for 90° the amount of Cherenkov light traveling to the forward and backward end, respectively, is equal.

In a beam loss shower, however, the distribution of the incident particle angles α is not constant and the relative velocity β is not equal to one. Both variables are function of the beam energy and the beam line geometry. In Section 7.3, the photon propagation velocity distribution and the resulting dispersion is calculated for different simulated loss scenarios.

5.3 FLUKA Simulations

Several Monte Carlo transport codes such as GEANT4 and FLUKA offer the possibility to generate and propagate optical photons. The model described in this chapter is verified using experimental data (see following chapter). However, to make estimates of the expected photon yields in the Cherenkov detectors, it is nevertheless useful to have several benchmarked methods available.

This section presents a summary of some of the simulations performed using FLUKA

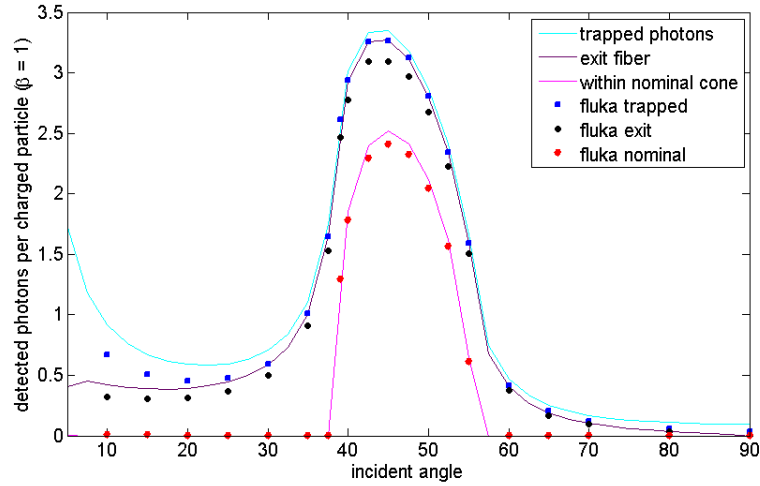


Figure 5.15: Comparison between the results for the photon yield per incident charged particle as a function of the impact angle α , calculated by the model explained in this chapter and FLUKA, respectively. The solid lines show the results calculated by the model. The upper, cyan curve shows the yield for the photons which are trapped in the fiber. The central, purple line shows the yield of photons which are trapped and able to exit the fiber at the end face. The lower, magenta curve shows the yield of the trapped photons which are able to exit the fiber within the nominal exit cone. The dotted distributions show the FLUKA results for the same three cases. The colors corresponding to each case are indicated in the legend of the graph.

version 2011.2 [3, 4] to determine the number of trapped photons in a fiber irradiated by 1 GeV ($\beta \approx 1$) electrons. The purpose of the study was to benchmark FLUKA code and verify the correct use of the user-controlled input parameters. A full description of the method, further results and a more detailed analysis of the angular distribution is given in [49].

The FLUKA model includes fiber core and cladding modelled with a silica composite (Silicon 0.533, Oxygen 0.467). The refractive indexes for the core and cladding were set to 1.46 and 1.44333 respectively, in accordance with NA equal to 0.22. The diameter of the core is $365 \mu\text{m}$. The cladding is surrounded by 'black hole', a FLUKA material with an infinite absorption cross section. Thus any tracking is terminated, and the photons at this external boundary are not reflected back into the fiber. The fiber was modelled to be 4 m long. Photon absorption coefficients were set such that absorption in the core was negligible. Scintillation and transmission radiation production were switched off in the core and cladding materials, and the generation of optical photons between the wavelengths 200 nm and 900 nm was permitted. The space at either end of the fiber contained a cylindrical region of air ($n \approx 1$) through which the optical photons could be transported.

The electron beam was represented as a rectangular distribution centred on the fiber axis, with a width in a plane orthogonal to the fiber axis equal to that of the fiber diameter. Therefore all 'impact parameters' (see Section 5.2.1.2) were sampled equally.

The angle of the beam with respect to the fiber axis varied from 5° to 90° and always impacted the fiber half-way along its 4 m length. For each beam angle, the number of 'trapped

photons', i.e the photons crossing a boundary 2 mm within the fiber core travelling towards the fiber exit was calculated. In addition, the angular distribution and total number of photons exiting the fiber was calculated. A solid angle bin corresponding to the acceptance angle for a fiber of NA 0.22 was defined. It was therefore possible to calculate the exact number of photons exiting within the nominal exit cone.

Figure 5.15 shows a comparison between the results for the photon yield per incident charged particle as a function of the impact angle α , calculated by the model explained in the in this chapter and FLUKA, respectively. The solid lines show the results calculated by the model for the following three cases (cf. Figure 5.9a): number of trapped photons, number of trapped photons that subsequently exit the fiber, and number of trapped photons that subsequently exit the fiber within the nominal exit cone. The colors corresponding to each case are indicated in the legend of the graph. In comparison, the three dotted distributions show the results of the FLUKA simulation. The results are in reasonable agreement. The small differences between the calculated values, in particular towards small angles, are currently not fully understood.

6 Verification Measurements

To validate the model developed in the previous section, three beam tests were performed. The studied properties are:

- The dependency of the light yield on the impact angle α of the charged particle.
- The dependency of the light yield, generated by an extended charged particle beam, on the diameter of the fiber.

In the following sections each beam test is discussed in detail.

6.1 Angular Dependency of the Cherenkov Light Yield

To verify predictions of the model on the dependency of the light yield on the impact angle α of the charged particle, two beam tests were performed.

6.1.1 First Beam Test

The first beam test was carried out at the H6A test beam in the CERN North Area in October 2011, parasitically to a beam test of the HEPHY institute, Vienna. The beam consisted of protons with a momentum of approximately 120 GeV/c and had a divergence of less than 5 mrad. The spill duration was approximately 8 s, with approximately $3 \cdot 10^4$ protons per spill.

As shown in Figures 6.1 and 6.10a, the fiber was mounted on a rotatable support. In total, 16 angular positions between 10° and 85° , in 5° degree steps were measured. For the photon detection, a read-out system similar to the one employed for the BLPM system at FERMI@Elettra [18], was used. It consists of a Hamamatsu S10362-11-050U MPPC (Multi Pixel Photon Counters) photon detector, which is an SiPM-type detector with 400 pixels, each $50 \times 50 \mu\text{m}^2$ large. Temperature drifts of the MPPC gain are compensated by means of a Negative Temperature Coefficient (NTC) Thermoresistor wired to the feedback loop of the reverse bias voltage generator [18].

Figure 6.2 shows a persistence plot of the dark count pulses for the MPPC used at the beam test, measured at room temperature. The pulses corresponding to each p.e.-level, i.e. to the number of simultaneously fired pixels, is clearly visible. The pulses corresponding to a p.e.-level larger than 1 are caused by optical crosstalk between the pixels. The pulse height due to one fired pixel was approximately -4 mV and accordingly approximately $-N \times 4$ mV for N simultaneously fired pixels.

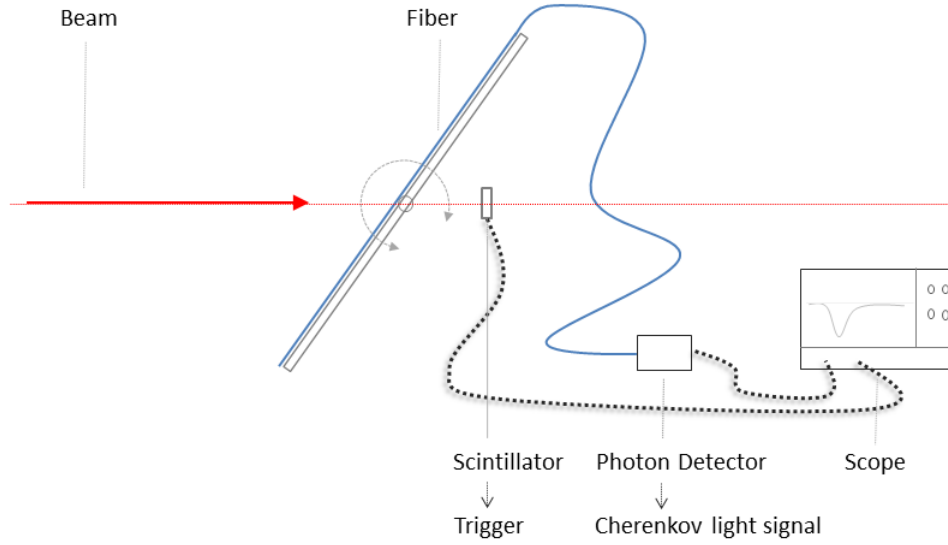


Figure 6.1: Schematic drawing of the beam test setup for the measurement of the photon yield per incident charged particle and the angular dependency of the trapping probability.

The employed fiber (Thorlabs BFH22-365) was a hard polymer buffer, pure silica/fluorine silica multimode fiber, with a high OH content. Its nominal attenuation is presented in Section 4.1.2 (Figure 4.6). The diameter was $365 \mu\text{m}$ and the numerical aperture $\text{NA}=0.22$. The beam crossed the fiber after a length of approximately 4 m from the PD.

Before the measurements, an estimation of the expected signal amplitude was performed. From the average arrival rate of the protons during the spill ($\approx 3.75 \cdot 10^3$ protons/s) and the recovery time of a single pixel (~ 50 ns, cf. Figure 6.2), it follows that the probability of two successive protons arriving within the recovery time of the PD, and therefore an overlap of their signal pulses was negligible. Since β is approximately 1 for 120 GeV-protons, the number of trapped photons for each proton, as a function of α , is expected to follow the curves shown in Figure 5.9a. Thus, for the optimal incident angle for trapping, which is approximately 45° for quartz fiber, in average only between 2.5 and 3.5 photons per proton are expected to reach the active surface of the PD. For less optimal angles, according to Figure 5.9a, this number is expected to be much lower.

Considering the influence of both the attenuation due to the 4 m of fiber and the PDE of the MPPC (cf. Figures 5.12a and 5.11b), only 19.8 % of the photons arriving at the MPPC is expected to be detected, i.e. in average between 0.5 and 0.7 photons per proton for the optimal incident angle.

Due to the fact that SiPM-type detectors show a high dark count rate at the 1 p.e. level, in the range of 1 MHz/mm^2 at room temperature, this signal can not be separated from the dark counts by applying an appropriate threshold on the signal amplitude.

Therefore, a scintillator was used as a trigger for the arriving protons. The scintillator was part of the beam test setup of HEPHY, and was 30 mm wide and 9.5 mm high in a plane perpendicular to the beam direction. Both the scintillator and the MPPC were connected to

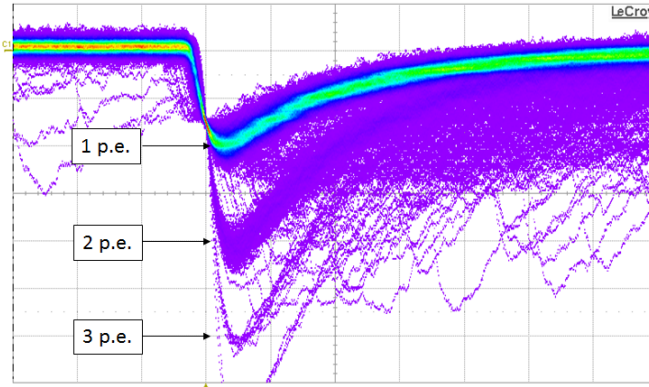


Figure 6.2: Persistence mode plot of the dark count signal of the MPPC module at room temperature, measured by an oscilloscope. Pulse forms corresponding to 1 p.e. (photon equivalent), 2 p.e., or 3 p.e. are observable. (horizontal axis: 10ns/div, vertical: 2mV/div)

a fast (2 GS/s) digital oscilloscope. For each trigger due to a scintillator pulse, i.e. a proton crossing the scintillator, the MPPC waveform with a temporal width of ± 100 ns w.r.t. the trigger signal was saved.

When a proton crossed both the scintillator and the fiber, a Cherenkov signal pulse was expected to occur at a distinctive time difference w.r.t. the trigger pulse. However, due to the fact that the area of the scintillator (285 mm^2) was much larger than the area of the fiber (3.5 mm^2), many of the saved waveforms did not contain any signal pulse.

In addition to the signal pulses, also dark count pulses were measured. The frequency of the dark counts was significantly reduced by using a spare CO_2 cooling system of the HEPHY group, which maintained the stability of the MPPC temperature at -0.5° C . The dark counts are uniformly distributed in time and have no correlation to the trigger signal.

Figure 6.3 shows a scope screenshot for a measurement at a later beam test in the CERN North Area in November 2011 with the same readout system, but a fiber with $d = 550 \mu\text{m}$ and a scintillator with a size of $20 \times 20 \text{ mm}^2$. The upper channel shows the MPPC waveform, saved at each trigger signal from the scintillator (lower channel), in persistence mode. For this measurement the single MPPC pixel pulse-height (1 p.e.) was approximately -4.5 mV . The red, horizontal band in the persistence graph of the MPPC channel indicates that most of the saved waveforms did not contain any pulse. The height of this red band corresponds to the average noise for this measurement. The continuous purple band below the red band of the height of 1 p.e.-amplitude indicates the uniform temporal distribution of the dark count pulses. Below this continuous purple band, uniformly distributed pulses with a 2 p.e.-amplitude are clearly visible. These pulses correspond to the dark pulses caused by optical crosstalk. At an interval of approximately -40 ns from the trigger signal an excess of pulses due to the Cherenkov photons is obtained. The interval between the trigger pulses and the signal pulses depends on different parameters of the used setup, e.g. cable lengths, used scintillator, etc., and is therefore different for the three performed beam tests.

Following from the considerations above, for a large number of saved MPPC waveforms,

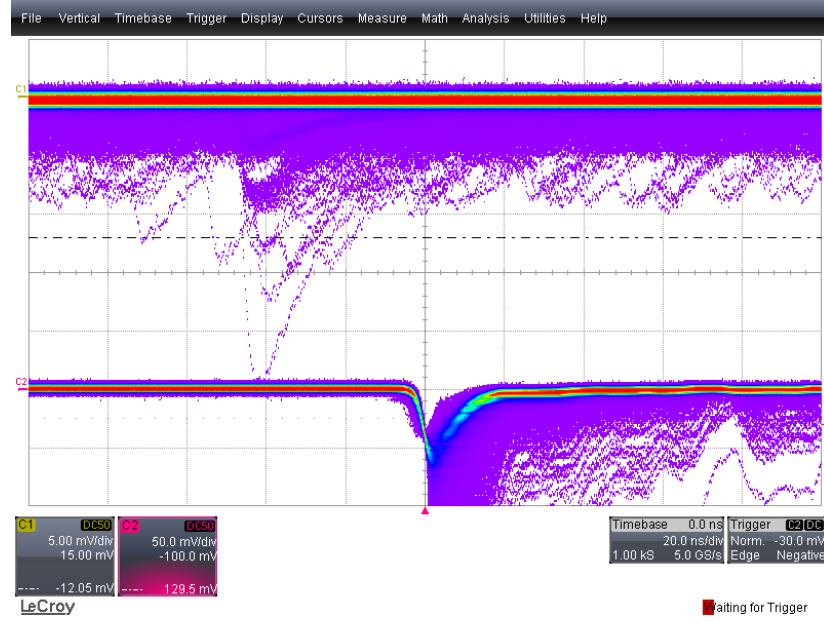


Figure 6.3: Scope screenshot for a measurement with a fiber with $d = 550 \mu\text{m}$ and a scintillator with a size of $20 \times 20 \text{ mm}^2$ in the CERN North Area in November 2011. The upper channel shows the MPPC waveform, saved at each trigger signal from the scintillator, in persistence mode. For this measurement the single MPPC pixel pulse-height (1 p.e.) was approximately -4.5 mV . The lower channel shows the scintillator signal. (horizontal axis: 20 ns/div , vertical: 5 mV/div)

the arrival time distribution of all occurring pulses (signal and dark counts) w.r.t. the trigger is expected to be a uniform distribution with a peak at a distinctive time related to the scintillator signal.

Figure 6.4a shows the distribution of the arrival time of all measured pulses w.r.t. the trigger signal, measured during the beam test in October 2011 at an angle of 45° . The origin of the time axis corresponds to the trigger signal and negative time values correspond to an earlier arrival time at the scope compared to the scintillator trigger. The peak shows a steep rise at its left side, and a tail at its right side. This can be explained by considering the photon propagation velocity distribution of the Cherenkov photons coupled into the fiber core. As discussed in Section 5.2.1.7 and illustrated in Figure 5.14, this velocity distribution is depending on the impact angle α of the charged particles onto the fiber. For angular range between 45° and 50° the propagation velocity distribution peaks at the highest possible velocity (c/n_{co}) and has a long tail to lower velocities. Thus, the steep rise at the left side of the peak in the pulse arrival time distribution is due to the fact that most of the photons propagate with the maximum possible velocity c/n_{co} . The tail to larger arrival times is formed by the photons with a lower propagation velocity.

Figure 6.5a shows the pulse height distribution for all pulses (dark counts and signal pulses) contributing to the pulse arrival time distribution shown in Figure 6.4a. The first and highest peak at the right side is the 1 p.e. peak, which contains many dark counts beside the signal pulses. The next peak to the left is the peak for the 2 p.e.-level, etc.

In order to calculate the total number of photons measured by saving the MPPC waveform

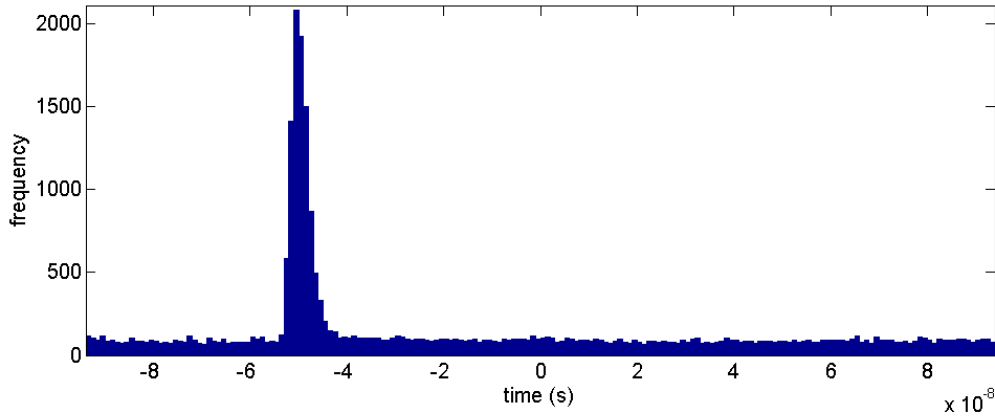


Figure 6.4: Distribution for the arrival time of all measured pulses (dark counts and signal pulses) w.r.t. the scintillator signal, during the beam test in October 2011 at an angle of 45° . The scintillator area was 285 mm^2 , whereas the area of the fiber was 3.5 mm^2 . The total number of saved waveforms used to generate this histogram is 129.000. The origin of the time axis corresponds to the trigger signal. Each bin is 1 ns wide.

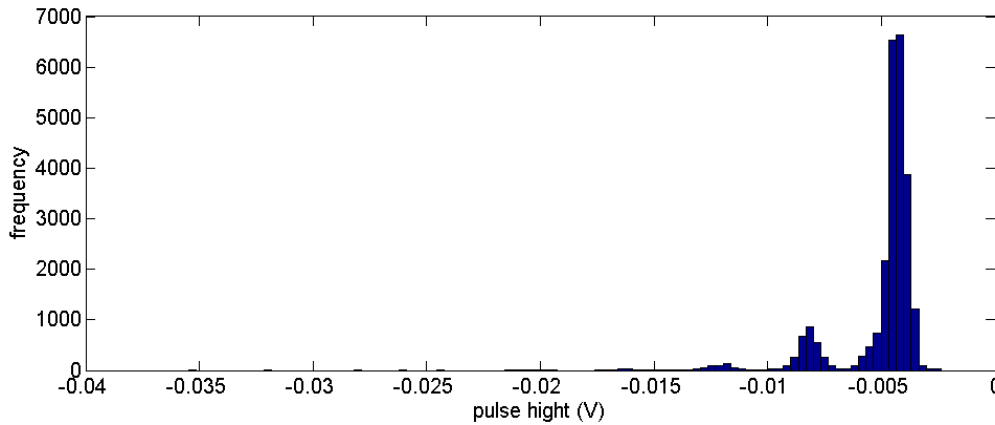


Figure 6.5: Pulse height distribution of all pulses (dark counts and signal pulses) contributing to the distribution presented in the figure above. The first and highest peak at the right side is the 1 p.e. peak, the second peak corresponds to 2 p.e., etc.

at each scintillator trigger signal, the signal pulses have to be separated from the dark pulses, and each signal pulse has to be attributed to the p.e.-level (number of photons) according to its pulse height.

Figure 6.6 shows the arrival time distributions of all measured pulses after their allocation to a particular p.e.-level. The distributions for the first six p.e.-levels are presented. The resulting total number of detected photons for each p.e.-level is calculated by subtracting the mean background signal due to the dark counts from the integral over the distribution over an interval containing the signal peak. The resulting value is multiplied by the integer corresponding to its p.e.-level. The mean background signal, illustrated as a magenta line in each of the graphs, is estimated by calculating the average bin content in the flat part of the distribution to the left of the signal peak. The statistical error on the total number of

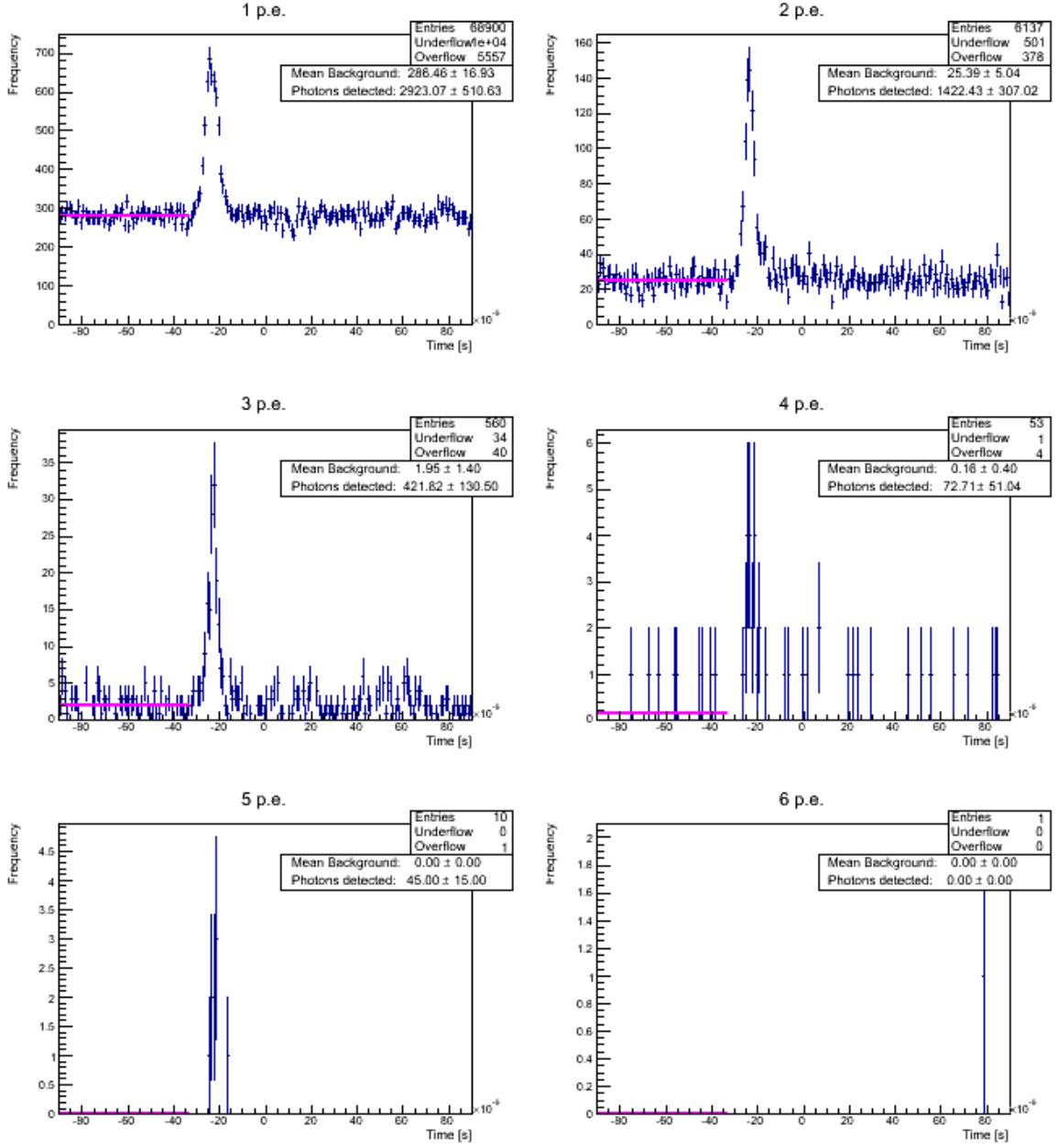


Figure 6.6: Distributions for the arrival time of all measured pulses (dark counts and signal pulses), separated for each p.e.-level. The horizontal , magenta lines drawn into each graph represents the estimated average magnitude of the background due to dark counts. The presented data were measured during the beam test in April 2012 at an angle of 45° and a scintillator with a size of $20 \times 20 \text{ mm}^2$. The total number of saved waveforms used to generate these histograms is 75.000.

photons for each p.e.-level is estimated by assuming an error per bin equal to the square root of the bin content, and a subsequent error propagation.

The overall number of measured photons for a certain angular position, $N_{ph,ov}(\alpha)$, is obtained by summing over the results of all p.e.-levels. By normalizing $N_{ph,ov}(\alpha)$ to the number of saved MPPC waveforms (= triggers), the results $N_{ph,ov,norm}(\alpha)$ for different incident angles

α can be related to each other and are expected to follow a similar distribution as the photon yield per incident particle as shown in Figure 5.9a.

However, for an absolute determination of the average number of detected photons per proton crossing the fiber, $N_{ph.p.P}$, the number of protons that crossed the fiber, and therefore contributed to the overall number of measured photons for each angular position, has to be known.

In order to calculate the ratio between the number of protons crossing the scintillator and the number of protons crossing both the scintillator and the fiber, the sensitive areas of the detectors, and also the beam intensity distribution along the width of the scintillator has to be considered.

6.1.2 Second Beam Test

Due to the short beam time, the position of the fiber in relation to the beam profile and the scintillator could not be measured during the beam test in October 2011. Therefore, a further parasitic beam test was scheduled in the CERN North Area in November 2011. The test setup and the beam conditions were equal to the one at the beam test in October 2011, except that a scintillator with the size of $20 \times 20 \text{ mm}^2$ was used and that two fibers, one with a diameter equal to $365 \mu\text{m}$ and one with a diameter equal to $550 \mu\text{m}$, were mounted onto the rotatable support.

For an absolute determination of the average number of detected photons per proton crossing the fiber, only one angular position ($\alpha = 45^\circ$) was measured. The horizontal position of the scintillator with respect to the beam profile was determined by scanning different horizontal positions x of the fibers with respect to the scintillator, whereas the beam profile and the scintillator position were kept constant. For each of the horizontal fiber positions, the number of photons normalized to the number of scintillator triggers, $N_{ph,norm}(x)$, was calculated. The horizontal beam profile was measured by a Delay Wire Chamber, which is part of the instrumentation of the beam test area.

The distribution of $N_{ph,norm}$ as a function of the horizontal fiber position is, subject to an appropriate normalization of the signal, expected to follow the horizontal distribution of the beam intensity. Therefore, the horizontal measurement positions of the fibers with respect to the beam profile could be obtained by numerically finding the optimal match between $N_{ph,norm}(x)$ and the beam intensity distribution. Due to the fact that the fiber positions with respect to the scintillator were known ($\pm 1 \text{ mm}$), the position of the scintillator with respect to the beam profile could also be determined ($\pm 1 \text{ mm}$).

The magenta line in Figure 6.7a shows the normalized measured beam profile averaged over five spills. The reason for the jagged curve shape could not be established by the person in charge of the Delay Wire Chamber in the CERN North Area. The normalized beam profile is fitted by a double gaussian fit function, indicated as a red line. The blue and cyan dots represent the measured Cherenkov signal, optimally matched to the beam profile. The two Cherenkov signal points at a horizontal position of approximately -8 mm correlate to the the

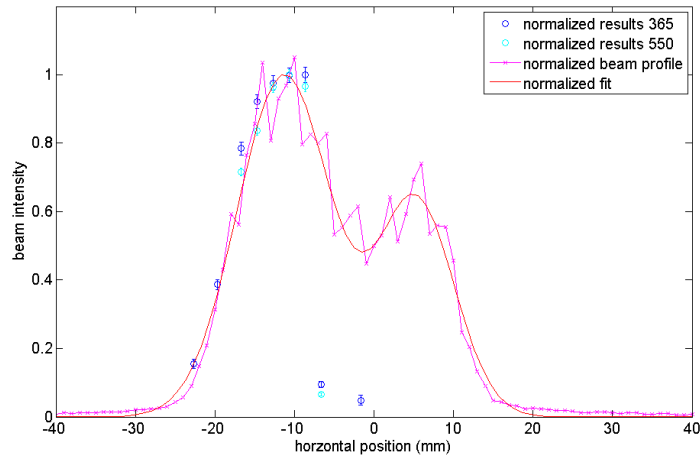


Figure 6.7: Normalized beam profile (magenta line), double gaussian fit on the normalized beam profile (red curve) and normalized results for the Cherenkov signal, measured at different positions of the fiber w.r.t. the scintillator. The blue dots show the normalized result for the fiber with a diameter equal to $550\ \mu\text{m}$ and the cyan dots show the result for the fiber with a diameter equal to $365\ \mu\text{m}$. The errorbars represent the statistical errors. Both results for the Cherenkov signal were adjusted in normalization and horizontal position to optimally match the curve shape of the normalized beam profile.

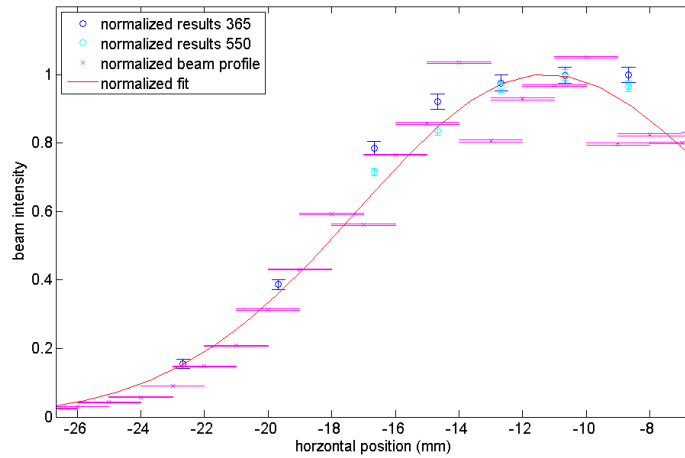


Figure 6.8: Zoomed image of the beam profile over the range that covered the trigger scintillator. The blue dots show the normalized Cherenkov signal for the fiber with a diameter equal to $550\ \mu\text{m}$ and the cyan dots show the normalized Cherenkov signal for the fiber with a diameter equal to $365\ \mu\text{m}$, respectively, both measured at different fiber positions. The errorbars represent the statistical errors. Both results for the Cherenkov signal were adjusted in normalization and horizontal position to optimally match the curve shape of the normalized beam profile.

right edge of the scintillator.

Figure 6.8a shows a zoom of the beam profile over the estimated range that covered the trigger scintillator. The ratio between the number of protons crossing the scintillator and number of the protons crossing both the scintillator and the fiber was calculated by dividing the integral over the fitted beam profile over an interval corresponding to the width of the fiber, at a certain position x , by the integral over the total width of the scintillator.

Furthermore, the average number of detected photons per proton crossing the fiber, $N_{ph.p.P}$, was calculated for each of the measurements at the different horizontal fiber positions by dividing the total number of measured photons for each measurement by the number of protons that crossed the fiber at the position in question.

For the fiber with a diameter equal to $365 \mu\text{m}$, in total seven positions were scanned. Consequently, the final result for $N_{ph.p.P}$ was calculated by a weighted average of the results for all scanned positions.

$$N_{ph.p.P} = 0.469 \pm 0.012 \text{ (stat.)} \quad (6.1)$$

Systematic uncertainties - There are multiple sources of possible systematic errors, the following of which are to be considered:

- The uncertainty of the scanned positions of the fiber with respect to the scintillator.
This affects the estimation on the ratio between the number of protons crossing the scintillator and number of the protons crossing both the scintillator and the fiber. For this, the positions of the fiber were varied within a range of $\pm 1 \text{ mm}$ w.r.t. the scintillator and a resulting uncertainty was found to be $\pm 13.5 \%$.
- The error on the parameters of the double gaussian fit function.
To obtain an estimate, the fit parameters were modified within their 95 % confidence interval. The resulting uncertainty was found to be $\pm 3.5 \%$.
- Long term stability.
The long term stability of the test setup was appeared to be very good and no significant contribution is expected.
- Uncertainty in angular position.
The effect of an uncertainty in the angular position was studied considering of the model discussed in the previous section. A variation of α within the range $45^\circ \pm 0.5^\circ$ resulted in an uncertainty of $\pm 1.5 \%$.

The total systematic uncertainty due to the items listed above is $\pm 14 \%$ and therefore the final result for the average number of detected photons per proton crossing the fiber is:

$$N_{ph.p.P} = 0.469 \pm 0.012 \text{ (stat.)} \pm 0.065 \text{ (sys.)} \quad (6.2)$$

Further systematic uncertainties that are not considered for the result stated above, but those which will be covered in [49] are:

- Data analysis.

For the data analysis, each MPPC pulse is attributed to a p.e.-level, i.e. a certain number of photons, according to its pulse height by setting cuts on the signal amplitude. From the pulse height spectrum shown in Figure 6.5a, it can be observed that the bins between the p.e.-peaks are not completely empty and therefore these cuts are limited in efficiency.

- The influence for optical crosstalk between pixels.

The negligence of fact that also each avalanche initiated by a signal photon can cause an avalanche in a neighbouring pixel by optical crosstalk leads to a an overestimation of the result for the number of photons detected.

6.1.3 Results

The absolute result for $N_{ph.p.P}$ for the impact angle of 45° , obtained from the data taken at the beam test in November 2011, was utilized for the normalization of the results for the angular scan, $N_{ph,ov}(\alpha)$, computed from the data taken at the beam test in October 2011 (see Section 6.1.1).

Figure 6.9 shows the comparison between the predictions of the model discussed in the previous section (solid lines) and the experimentally observed data points. The three curves shown represent the three cases trapped (dark blue), trapped and exit (cyan), and trapped and exit within the nominal exit cone (magenta). Each curve is computed by scaling the distribution presented in Figure 5.9a down by a factor 0.198. This factor is the result of a joint consideration of the influence of both the attenuation due to the 4 m of fiber and the PDE of the MPPC. For the errorbars on the data points the following contributions are considered:

- The error due to a propagation of the uncertainty on the absolute result for $\alpha = 45^\circ$ as presented in (6.2).
- The statistical uncertainties on the results of the angular scan, $N_{ph,ov,norm}(\alpha)$.
- An additional systematic error due to an uncertainty of the angular position during the angular scan.

The coupling efficiency between fiber and PD is not taken into account. However, due to the geometry of optical connection is between fiber and the PD it is expected that not all photons exiting the fiber, but more than all the photons exiting the fiber within the nominal exit cone are detected, i.e. that the data points lie between the magenta and cyan curve.

The data shows a good agreement with the theory. Only at the maximum of the distribution the experimental data points are slightly below the curve for the 'nominal exit'-photons. The reason for this could be an overestimation of the coupling efficiency in the scaling factor for the theoretical curves.

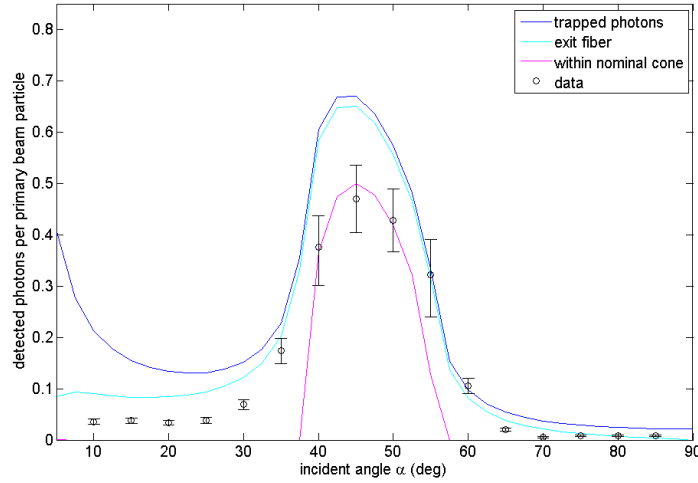


Figure 6.9: Result for the angular scan measuring the Cherenkov light yield per crossing charged particle with $\beta \approx 1$. The solid lines show the theoretical expected curves, which are computed by scaling the distribution shown in Figure 5.9a down by a factor 0.198. This factor is the result of a joint consideration of the influence of both the attenuation due to the 4 m of fiber and the PDE of the MPPC. The coupling efficiency between fiber and PD is not taken into account.

6.2 Dependency of the Light Yield on the Fiber Diameter

As discussed in Section 5.2.1.6, the photon yield resulting from an extended beam, i.e. a beam with much larger dimensions than the fiber core diameter, is expected to scale with the square of the fiber core diameter. However, in [46, 47] it is stated that the photon yield for a 'collimated' beam, scales by the cube of the fiber core diameter. Since, after comprehensive considerations, no reason for this additional power could be deduced, a dedicated beam test was performed.

This beam test was carried out at the T9 test beam in the CERN East Area in April 2012. Four fibers with the diameters $200\ \mu\text{m}$, $365\ \mu\text{m}$, $550\ \mu\text{m}$ and $910\ \mu\text{m}$ were, with respect to the beam direction, mounted behind each other onto a rotatable support (see Figure 6.10b). By this, each of the fiber experienced the same part of the horizontal beam profile.

Due to the large fiber diameters the MPPC module employed in the first two beam tests ($1 \times 1\ \text{mm}^2$ active area) could not be used. A purpose built module containing a Hamamatsu S10362-33-050C MPPC ($3 \times 3\ \text{mm}^2$, 3600 pixels) was developed in collaboration with electronics engineers and the workshop of the CERN BE-BI-BL section. From the pulse height distribution which is shown in Figure 6.13 it is clear that the MPPC had a low crosstalk probability.

Moreover the module contains a custom developed transimpedance amplifier and an FC-type fiber connector (see Figure 6.11). The schematic of the amplifier circuit is presented in Figure 6.12. This circuit did not contain a feedback loop to stabilize the temperature drift of the gain. Therefore, in advance of each measurement the bias voltage was regulated by hand



Figure 6.10: (a) The support used for the beam test in the CERN North Area in October 2011. The black tube containing the fiber was mounted on rotatable support. The beam was incident from the right. The scintillator used as a trigger is hidden in the box on the right side of the picture. (b) The fiber support used for the beam test in the CERN East Area in April 2012. The four fibers with different diameters (red) were placed behind each other, w.r.t. the beam direction. The beam is incident from the right.

such that the single pixel pulse height was -10 mV, and after each measurement the pulse height spectrum was inspected for any drifts in the single pixel gain.

A total of 16 measurements were made corresponding to four different settings (in terms of angle and horizontal fiber position w.r.t. the beam) for each of the four fibers. The result were four data sets, one for each setting (see Figure 6.14), where each data set contained the overall number of detected photons normalized by the number of triggers, $N_{ph,ov,norm}$, for each of the four fiber diameters d_i , $i = 1, \dots, 4$.

According to the model described in the previous section, these four values for $N_{ph,ov,norm}(d_i)$ in each data set k were expected to follow the function:

$$N_{ph,ov,norm,k}(d_i) = a_k \cdot d_i^2 \quad (6.3)$$

where a_k is a constant parameter for each set, depending on the angular setting and the horizontal position of the fibers with respect to the beam profile.

6.2.1 Results

The hypothesis of a quadratic dependence on the fiber diameter was tested by applying a global fit of the form

$$a_k \cdot d_i^b \quad (6.4)$$

to all four data sets k , with a single parameter b for all settings. Thus, there were 5 parameters (a_1, \dots, a_4 and b) to be fit to 16 measured data points.

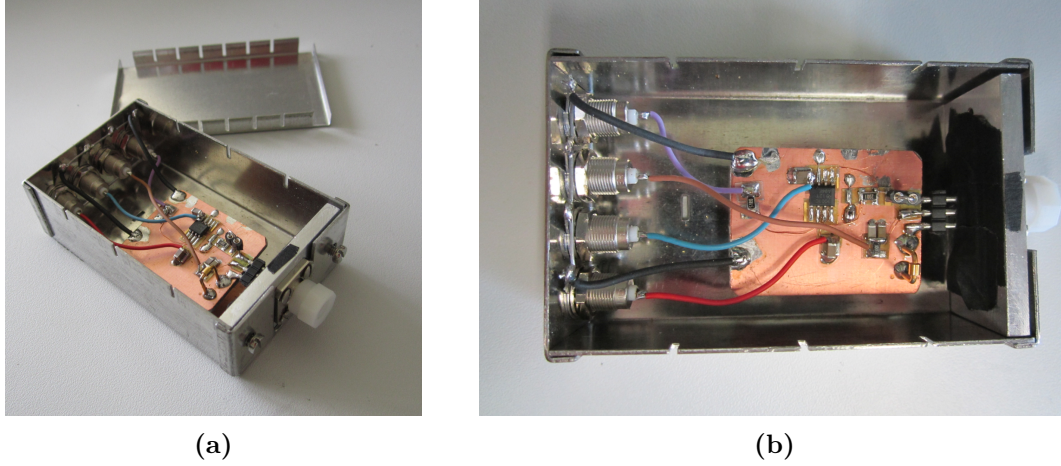


Figure 6.11: (a) Custom built module containing a Hamamatsu S10362-33-050C MPPC ($3 \times 3 \text{ mm}^2$, 3600 pixels) and a custom built transimpedance amplifier (see Figure 6.12 for the schematic). The FC-type fiber connector is visible at the front of the module. (b) Detailed view on the amplifier circuit board.

The global fit result for the parameter b is:

$$b = 2.163 \pm 0.064 \text{ (stat.)} \quad (6.5)$$

Systematic uncertainties - The following systematic uncertainties are considered:

- Uncertainty in the angular or horizontal fiber position.

Due to the fact that for a particular setting all four fibers were measured at the same angle and horizontal position within the beam profile, uncertainties on these parameters have no influence on the result of the fit parameter b .

- Stability of the test setup.

The stability of the test setup was regularly monitored during the measurements and was observed to be very good. Therefore no significant contribution to the uncertainty of b is expected.

- Nominal uncertainties of the fiber diameters.

The nominal uncertainties of the fiber diameters are in the sub-micron range. Since the thinnest fiber employed at the beam test had a diameter equal to $200 \mu\text{m}$, the influence of this is negligible.

- Reproducibility of the fiber connection.

For each setting, all four fiber diameters were measured consecutively and therefore each time the fibers had to be disconnected and reconnected to the MPPC module. Even though the module contained an FC-type fiber connector, small differences could have occurred. Moreover, each exchange of a fiber represented a risk in terms of polluting the fiber end face or the sensitive area of the MPPC.

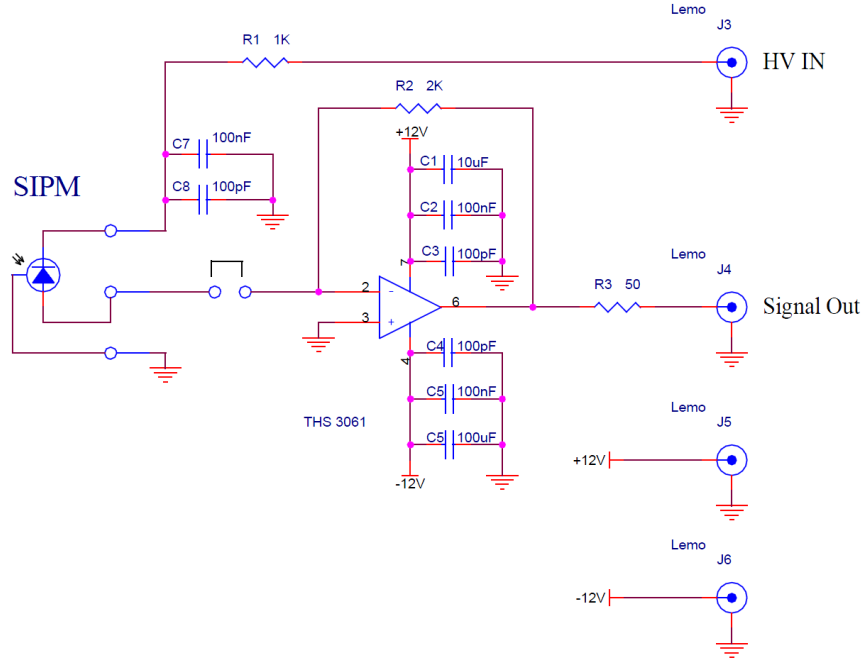


Figure 6.12: Schematic of the purpose built amplifier used for the beam test in April 2012, in the CERN East Area. Courtesy of E. Effinger and C. Chery.

A quantitative estimation for the resulting uncertainty on the fit parameter b is difficult. A systematic influence on the power in Equation (6.4) is not expected. However, due to the low number of data points, already one small outlier can influence the result of the fit. For a conservative estimate, single data points were modified to values $+15\%$ and -15% . The resulting uncertainty is $\pm 4.5\%$.

The final result for the fit parameter b is:

$$b = 2.163 \pm 0.064 \text{ (stat.)} \pm 0.097 \text{ (sys.)} \quad (6.6)$$

This result is compatible with the hypothesized quadratic dependency of the photon yield resulting from an extended beam on the fiber diameter, whereas a cubic dependency must be rejected.

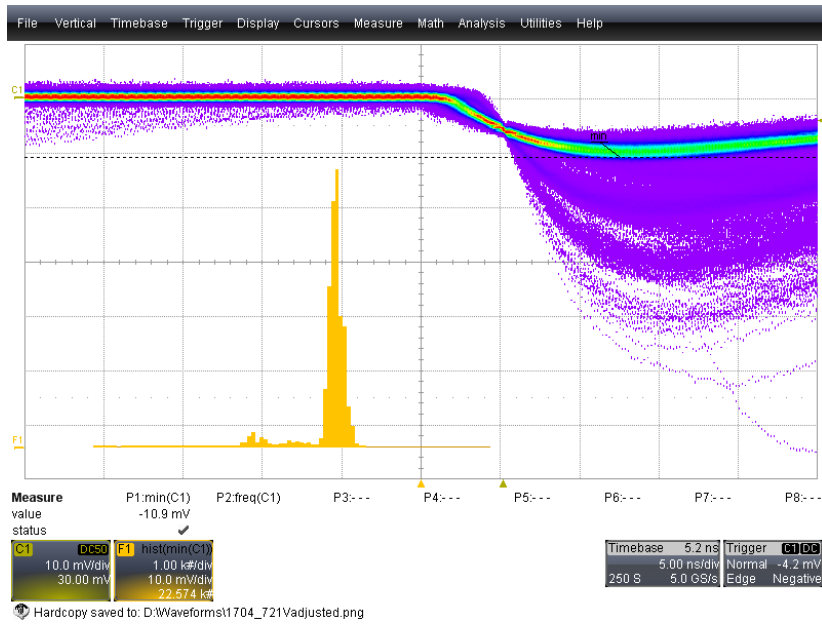


Figure 6.13: Persistence plot of the dark count signal of the MPPC (Hamamatsu S10362-33-050C) used for the beam test in April 2012, measured at room temperature. The MPPC reverse bias voltage was set by hand such that the single pixel pulse height (1 p.e.) was -10 mV. (horizontal axis: 5 ns/div, vertical: 10 mV/div)

The histogram (yellow) within the picture shows the pulse height distribution of the dark count signal. The horizontal scale for the histogram is 10 mV/div. The histogram shows a large peak at -10 mV, corresponding to the 1 p.e.-amplitude and a small peak at -20 mV, corresponding to the 2 p.e.-amplitude, i.e. crosstalk. The large difference between two peak heights indicates the low crosstalk probability of this device.

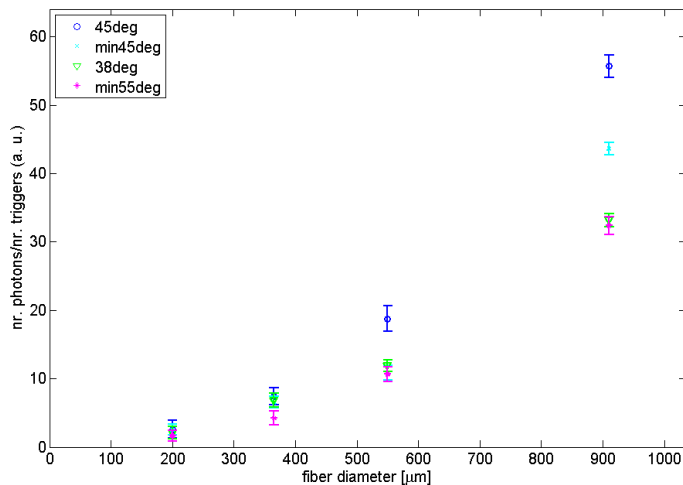


Figure 6.14: Measured data points for four different fiber diameters (200 μm , 365 μm , 550 μm and 910 μm) and four different settings. The data points belonging to the same data set (i.e. measured at the same setting) are displayed by a particular color. Only statistical errors are presented.

7 Cherenkov Fibers BLM for the CLIC Two Beam Modules

In the CLIC conceptual design report [9], ionization chambers, similar to the ones used at the LHC, are specified as the baseline choice for the BLM system in all CLIC machine subsystems, except for the damping and pre-damping rings. However, for the drive beam decelerators a very large number (≈ 50.000) of such BLMs would be required. To reduce the costs, alternative technologies, such as Cherenkov fibers [16] [18] [17] and long ionization chambers [14] [50] are considered. The specific application of Cherenkov fibers as a BLM for CLIC is discussed in this chapter.

The general benefits and drawbacks of the use of Cherenkov light in combination with quartz fibers for beam loss monitoring are (cf. [51, 25]):

1. Cherenkov radiation is an intrinsically very fast process with a typical time constant of less than 1 ns. This is very useful with regard to the fact that the limits on the longitudinal resolution of the beam loss position are a result of the possible timing resolution of the created signal.
2. Cherenkov light is only emitted by charged, relativistic particles. This has important consequences:
 - Slow (MeV-type) neutrons generated at a beam loss or synchrotron radiation do not produce signals in this type of BLM
 - A Cherenkov fiber BLM is largely insensitive to the effects of induced radioactivity of the beam line components.
 - Mainly ($> 95\%$) electrons and positrons produced in electromagnetic shower development give rise to an appreciable shower signal.
3. The high radiation resistance of quartz [28].
4. The sensor, i.e. the fiber, is immune to external electro-magnetic fields.
5. High precision external magnetic fields will not be disturbed.
6. Environmental conditions, e.g. temperature or vacuum, are usually no major problem.
7. A fiber sensor is capable of monitoring extended areas and is thereby extremely small with diameters of less than 1 mm.

Potential drawbacks of the design are:

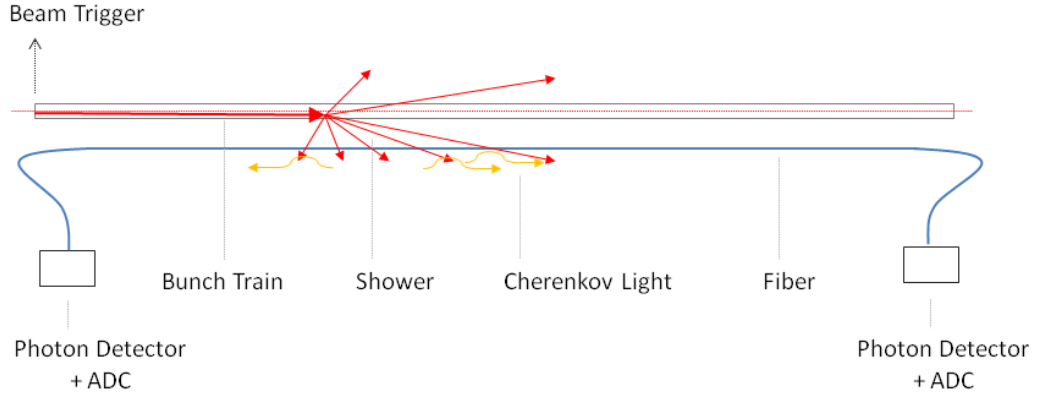


Figure 7.1: Schematic drawing of the principle of a Cherenkov Fiber BLM system.

1. The non-uniform, angular dependent response as discussed in Section 5.2.1.
2. The low trapped light yield. Only a few percent of the produced photons reaches the fiber end face (cf. Section 5.2.1.2).
3. Local radiation induced attenuation. It can lead to deceptive results for the signal amplitude.

Compared to Cherenkov fibers, the main advantage of long ionization chambers [15] is their uniform sensitivity. However, the achievable longitudinal resolution is only in the order of several meters.

The basic concept of a BLM system based on Cherenkov fibers is presented in Figure 7.1. A fiber is placed in parallel to the beam line and the particle shower, created by a lost bunch, generates Cherenkov light within the fiber. This light can be detected at either one or both ends of the fiber. By a measurement of the arrival time of the light pulse with respect to a trigger signal, which indicates the passing of the bunch at the upstream end of the fiber, the loss position can be determined. The longitudinal resolution is mainly limited by the sampling frequency of the employed digitizer (ADC). Neglecting dispersion and assuming that the beam is relativistic, the arrival time difference Δt at the downstream fiber end of two loss signals, created by a single bunch at the positions x_1 and $x_2 > x_1$, is given by:

$$\Delta t_{d,s} \approx \frac{(x_2 - x_1)}{c}(1 - n_{co}) = \frac{\Delta x}{c}(1 - n_{co}). \quad (7.1)$$

The according result for the upstream fiber end can be expressed as:

$$\Delta t_{u,s} \approx \frac{\Delta x}{c}(1 + n_{co}) \quad (7.2)$$

Note that, considering the refractive index n_{co} of the fiber core is approximately 1.46, the result for the downstream fiber end, $\Delta t_{d,s}$, is negative, meaning that the loss signal, generated at a further downstream position x_2 , will be detected before a signal created at x_1 . This is due to the fact that the bunch is traveling at a velocity $\approx c$, whereas the loss signal is only

propagating with a velocity $\approx c/n_{co}$. Furthermore, it follows from Equations (7.1) and (7.2) that the temporal separation of the signal at the downstream end is smaller by a factor

$$\epsilon_{sep} = \frac{\Delta t_{u,s}}{\Delta t_{d,s}} = \frac{(1 + n_{co})}{(1 - n_{co})} \stackrel{n_{co} \approx 1.46}{\approx} 5.5 \quad (7.3)$$

compared to the upstream fiber end. For example, for a distance $\Delta x = 1$ m between the loss locations $\Delta t_{d,s}$ is approximately 1.6 ns, whereas $\Delta t_{u,s}$ is approximately 8.2 ns.

Using a digitizer with a sampling frequency $f_S = 1/\Delta t$, the potential position resolution for the downstream fiber end is given by

$$\Delta x_{d,s} \approx \frac{c}{f_S |1 - n_{co}|} \quad (7.4)$$

and for the upstream end

$$\Delta x_{u,s} \approx \frac{c}{f_S |1 + n_{co}|}. \quad (7.5)$$

Assuming a sampling rate of 1 GS/s, this means a resolution limit of about 12 cm for the upstream fiber end, whereas only about 65 cm for the downstream end. For a sampling frequency of 250 MHz, as for example used at FERMI [18], these numbers have to be multiplied by a factor 4. Consequently, a detection of the Cherenkov light signal at the upstream end of the fiber is preferable.

The fiber BLM concept can be extended from single-bunch losses to multi-bunch trains as used in CLIC. For this application, however, there is an ambiguity for signals resulting from different loss scenarios. Thereby, the feasible resolution of the determination of the loss location and of the part of the train that generated the loss, is affected. The total length of the fiber can always give a rough estimate of the loss location. Methods to enhance the resolution of the loss location are discussed in Section 7.4.

To decide about the feasibility of a Cherenkov fiber BLM for CLIC, all its fundamental features have to be analysed and related to the CLIC requirements. Eventually, besides the radiation resistance and the related expected life time of quartz fibers, about the following points must be considered:

- Dimension of the optical fiber (diameter, NA).
- Required sensitivity and dynamic range of photon detector.
- Crosstalk between signals from both sides of the TBM.
- Achievable time resolution and, accordingly, the longitudinal resolution.

Therefore loss shower distributions, the resulting Cherenkov signals and their temporal distributions have to be estimated for different simulated loss scenarios.

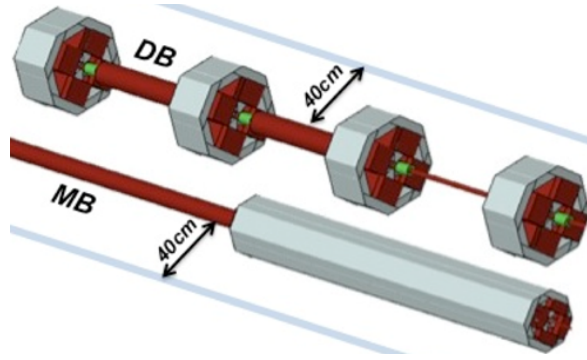


Figure 7.2: FLUKA representation of two the beam module [52]. The blue areas indicate the boundaries used for scoring shower particles.

7.1 Considerations on the TBM Radiation Levels

Conservative estimates for the annual absorbed dose at a position close to the accelerator are discussed in Section 3.3.7. The highest expected value is 10^5 Gy/year, which is obtained both at the DB at 2.4 GeV and the MB at 1500 GeV. In Section 4.2 it is shown that, for the application of Quartz Fiber Calorimeters, fibers were tested that showed no, or only a little degeneration after a total delivered dose of 2.2 Grad, which corresponds to 22 MGy. This result would imply an expected lifetime of 220 years, which is by far larger than the expected lifetime of CLIC. However, as also discussed in Section 4.2, there can be a great difference in radiation response between fibers due to the large number of influence parameters. Therefore, this test result can not be generalized and dedicated radiation hardness tests are necessary.

Of particular importance is here the effect of radiation induced attenuation (RIA) and its dependency on the wavelength of the transmitted light. The fact that, in general, RIA is higher for lower wavelength should be considered for the choice of the photodetector and its spectral response.

Additional difficulties related to RIA could arise if there would exist particular hotspots of loss positions along the beam line, where losses occur more often than at other positions. This would lead to a locally higher RIA and subsequently to deceptive results on the amplitude of loss signals that are created at positions that are, seen from the photodetector, further away than the hotspot. As a result, the calibration of the BLM would become difficult.

7.2 Simulation of Beam Losses in the CLIC Two Beam Modules

In order to determine the secondary relativistic particle shower caused by a beam loss in the CLIC two beam modules, simulations using the Monte Carlo code FLUKA [3, 4] were performed. Therefore, a pre-existing FLUKA model [9, 12], including a detailed representation of the beam line geometry of the TBM, was extended for Cherenkov fiber studies. These extensions are discussed in detail Section 7.2.1.

Due to the fact that many loss scenarios are possible, the following decisive cases for the dynamic range and the sensitivity, respectively, (cf. Section 3.3) were considered:

- Destructive losses at a single aperture restriction immediately upstream of a quadrupole. The impact is represented in the horizontal plane, and the loss angle determined by the maximum grazing angle possible between a defocusing and focusing quadrupole.
- Losses distributed at several points along the aperture before each quadrupole. The losses are represented by electrons travelling in the direction of the beam, generated in a circular distribution just inside the aperture.

To be able to do a comprehensive analysis on the required dynamic range, sensitivity and signal crosstalk between the two beam lines, both scenarios have to be simulated both for the main and the drive beam at energies corresponding to the maximum and minimum in each beam line, i.e. 0.24 GeV and 2.4 GeV for the DB and 9 GeV and 1500 GeV for the MB.

The FLUKA model [52] includes main beam line components such as the quadrupoles, Power Extraction and Transport Structures (PETS) and the Accelerating Structures (AS) (cf. Figure 7.2). The aperture restriction in the DB is modelled at the end of each PETS with a diameter of 23 mm, equal to the aperture of the DB quadrupole. In the MB, the decreasing aperture of the 24 cells within the AS is modelled in fewer but thicker steps, with a final diameter of 4.7 mm. The vacuum chamber within in the MB quadrupole is modelled with a diameter of 10 mm.

From the model developed in Section 5.2.1, and in particular from Equation (5.20), it follows that the impact angle, α , and the relative particle velocity, β , are the decisive variables for the creation and trapping process of Cherenkov light within the fiber.

The spatial distributions of the e^+e^- fluence can give a first idea of the angular distribution of the shower. In Figures 7.3 and 7.4 the simulated spatial distribution of the e^+e^- fluence per primary due to an accidental loss is presented for four scenarios (DB at 0.24 GeV, DB at 2.4 GeV, MB at 9 GeV and MB at 1500 GeV). In each of the loss scenarios, the impact position of the beam is assumed to be the last aperture restriction of the AS immediately upstream of a quadrupole.

Figure 7.3a shows the distribution due to an accidental loss at the DB at 0.24 GeV. The shower has its largest intensity at a longitudinal position close to the loss position, and therefore at an angle α close to 90° . Furthermore, the shower is forward directed. Due to the directionality of the Cherenkov effect, the signal traveling to the downstream end of the fiber is expected to be larger than the signal traveling to the upstream fiber end.

Figure 7.3b shows the e^+e^- fluence distribution due to an accidental loss at the DB at 2.4 GeV. The spatial shower is very similar to the one for 0.24 GeV at the DB. This can be explained by the fact that the geometry of the beam line is exactly the same for both energies. However, at a horizontal distance of 40 cm beside the beam line, the e^+e^- fluence for a loss at the DB at 0.24 GeV is only approximately 1 % of the level due to a loss at the DB at 2.4 GeV.

Due to the spatial similarity of the distributions for both energies, the ratio between the resulting downstream and upstream signal is expected to be similar. However, the signal

amplitude is expected to be substantially lower for a loss at 0.24 GeV.

Figure 7.4a shows the e^+e^- fluence distribution due to an accidental loss at the MB at 9 GeV. Even though the actual impact position of the beam is the last aperture restriction immediately upstream of a quadrupole, i.e. at 599 cm, the shower develops at a position further downstream, with the shower core at around 730 cm. This is due to the fact that the final aperture of the MB AS just upstream of the quadrupole is only 4.7 mm, whereas the diameter of the vacuum chamber within in the MB quadrupole 10 mm. Subsequent to the quadrupole is the next AS, in which the aperture gradually decreases back to 4.7 mm. The forward directed loss shower particles therefore continue traveling in the vacuum chamber until they imping upon the decreasing aperture of the AS.

In contrary to the MB situation, the diameter of the vacuum pipe within the DB quadrupole is equal to the one of the last aperture upstream of the quadrupole. Therefore the shower starts developing directly in the quadrupole material.

The spatial shower distribution around the shower core shows no prominent forward-directionality for the MB loss. Therefore there is no significant difference expected between the magnitude of the upstream signal and the downstream signal.

Figure 7.4b shows the e^+e^- fluence distribution due to an accidental loss at the MB at 1500 GeV. The actual impact position of the beam is at 1599 cm. Similar to the case of the MB at 9 GeV, and due to similar reasons, the shower starts developing at a position further downstream, with the shower core at around 2000 cm. The larger distance between the impact position of the beam and the shower core can be explained by the fact that the length of the quadrupoles in the TBM is adjusted according to the beam energy (cf. Section 3.1). As for the for MB at 9 GeV, the simulated shower distribution around the shower core shows no prominent forward-directionality and consequently there is no significant difference expected between the magnitude of the upstream signal and the downstream signal.

However, regarding all four examples, it has to be kept in mind that the plots contain no specific information about the angular and velocity distributions of the particles and cannot be used to predict the actual Cherenkov light signal.

7.2.1 Quantitative Determination of the Photon Yield

For a quantitative determination of the photon yield resulting from each simulated loss, the energy, particle type and crossing angle α of the secondary shower particles at the position of the fiber have to be known. Therefore, two scoring boundaries representing the fibers at the DB and MB side of the beam line (cf. Figure 7.2) were added to the pre-existing FLUKA model [9, 12]. These scoring boundaries are placed parallel to each beam, at a horizontal distance of 40 cm from the beam line. At first, all charged particles above the Cherenkov production threshold were binned according to their energy, particle type and crossing angle. For the following calculations only electrons and positrons in the secondary particle shower are considered. Whilst other charged shower particles are produced, especially for losses at 1.5 TeV, they still account for less than 5% of the particle shower.

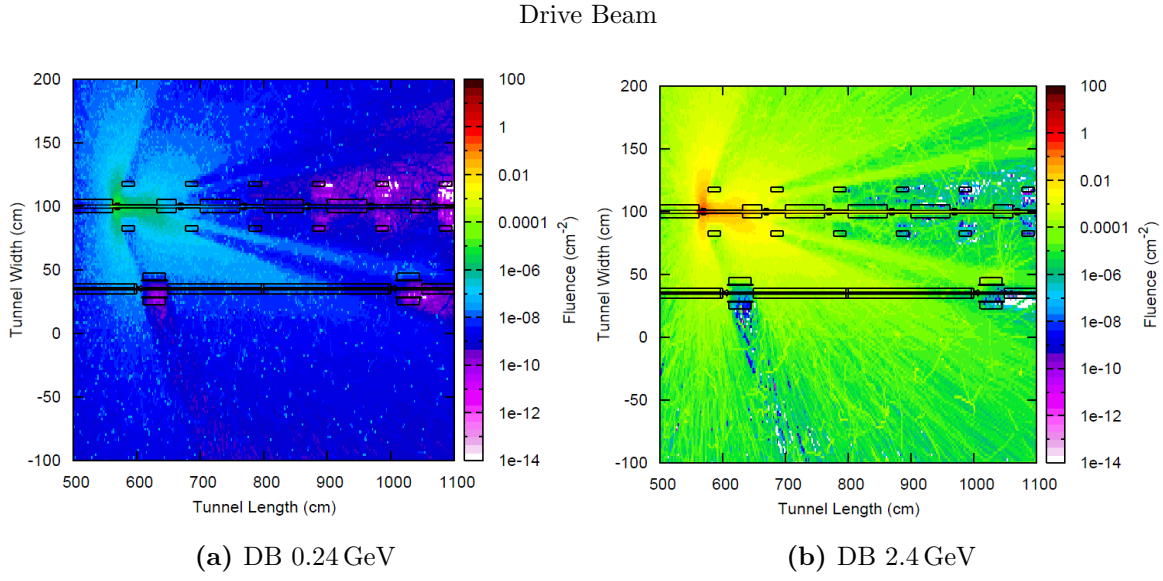


Figure 7.3: Spatial distributions of the e^+e^- fluence due to a destructive loss at the DB at (a) 0.24 GeV and (b) 2.4 GeV. The fluences are averaged over a depth of 20 cm, centered on the beam line. Only electrons and positrons with an energy above the Cherenkov threshold are shown. The simulated loss position is the last aperture restriction in the AS immediately upstream of the quadrupole, i.e. at 558 cm for both cases [53].

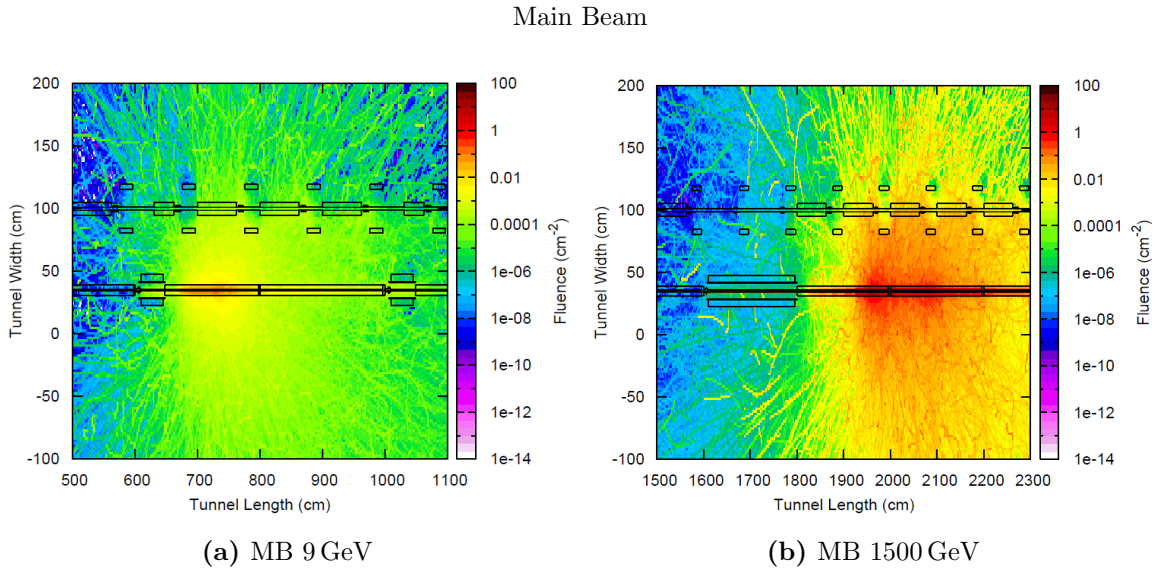


Figure 7.4: Spatial distributions of the e^+e^- fluence due to a destructive loss at the MB at (a) 9 GeV and (b) 1500 GeV. Only electrons and positrons with an energy above the Cherenkov threshold are shown. The fluences are averaged over a depth of 20 cm, centered on the beam line. The simulated loss position is the last aperture restriction in the AS immediately upstream of the quadrupole, i.e. at 599 cm and 1599 cm for the 9 GeV and 1500 GeV respectively [53].

For the electrons and positrons a linear binning system with 36 bins for the relative velocity β (from $\beta = \beta_{th}$ up to $\beta = 1$), and 36 bins for the impact angle α (from 0° up to 180°) was developed. Due to the fact that the quantity β is not directly scoreable with FLUKA, the energies corresponding to each center of the linear β -bins were calculated using Equation (5.5). The results are normalized to one lost electron and scaled for a boundary height of $365\mu\text{m}$ to match the diameter of a typical Cherenkov fiber used for BLM.

Figure 7.5a shows the binned distribution of electrons and positrons, crossing the scoring boundary parallel to the beam line at the DB side, for an accidental loss at the DB at 0.24 GeV. As already indicated in Figure 7.3a for the spatial distribution of the e^+e^- fluence, the shower has its largest intensity at an angle α close to 90° , and a forward directed part with a peak at around 20° . The major part of the shower particles have a β close to 1.

From this distribution, the number of transmitted Cherenkov photons that exit the fiber within the nominal exit cone is calculated by multiplying the central value from each bin by the corresponding values in Figure 5.10. The resulting binned distribution for the generated photons is presented in Figure 7.6a. The photons generated within a range $0^\circ \leq \alpha \leq 90^\circ$ travel to the downstream fiber end, whereas the photons generated within a range $90^\circ \leq \alpha \leq 180^\circ$ travel to the upstream end. Due to the asymmetry in the shower distribution, there are fewer photons transmitted upstream.

Figure 7.7a shows the binned distribution of electrons and positrons, crossing the scoring boundary parallel to the beam line at the DB side, for an accidental loss at the DB at 2.4 GeV. As expected from the e^+e^- fluence plots presented Figure 7.3, the angular distribution is very similar to the one for the loss at the DB at 0.24 GeV. The resulting binned distribution for the generated photons is presented in Figure 7.8a.

The estimated total number of photons that will exit the fiber within the nominal exit cone for the accidental scenarios discussed above, scaled to a destructive level ($N_{e^-,dam} = 1.54 \cdot 10^{12}$, cf. Table 3.3), are presented in Table 7.1.

	Destructive loss signal ($N_{ph}/train$)*		Ratio DS/US
	Downstream (DS)	Upstream (US)	
DB - 240 MeV	$4.3 \cdot 10^7$	$2.8 \cdot 10^7$	1.54
DB - 2.4 GeV	$5.4 \cdot 10^8$	$3.7 \cdot 10^8$	1.46

Table 7.1: Estimated number of photons ($N_{ph}/train$) that will exit the fiber ($d = 365\mu\text{m}$) within the nominal exit cone, due to a destructive loss at the DB at 0.24 GeV and 2.4 GeV, respectively. *The duration of the DB bunch train, τ_{train} , is 240 ns (cf. Section 3.3).

For a fiber with a diameter of $365\mu\text{m}$ and a dangerous loss at the DB at 0.24 GeV, the estimated number of photons is of the order of 10^7 for both the downstream and the upstream end. For a dangerous loss at the DB at 2.4 GeV, the corresponding number is approximately a factor 10 larger. This is contrary to the expectation from the e^+e^- fluence levels, where the results for the two energies differ by a factor 100.

Due to the similarity of the angular distribution of the loss shower for both simulated energies, the ratios between the magnitude of the downstream and upstream signal are comparable and both in the range of 1.5.

The largest signal is obtained at the downstream fiber end for the loss at the DB at 2.4 GeV. Considering that the duration of the bunch train is 240 ns in the DB, the maximum average arrival rate is approximately $2.3 \cdot 10^6$ photons/ns. This result can be utilized to estimate the required upper limit of the dynamic range of the photodetector for the DB side, which is defined as 10 % of the signal produced by a destructive loss (cf. Section 3.3). Consequently, for the given fiber diameter, the PD should have a linear response up to an arrival rate of $2.3 \cdot 10^5$ photons/ns.

The two examples presented above for the accidental losses at energies corresponding to the maximum and minimum in the DB are used to demonstrate the use of the model developed in Section 5.2.1 with a dedicated binning system for α and β introduced into the TBM FLUKA model.

For the estimation of the required sensitivity of the photodetector at the DB side, and to determine that a sufficient number of photons are produced in a fiber of reasonable diameter, simulations were performed for the loss scenarios corresponding to the lower limit of the dynamic range, e.g. losses were distributed along the aperture rather than a single loss location.

Whilst, based on these simulations, it can be concluded that a fiber with core diameter of $365 \mu\text{m}$ will produce a sufficient number of photons to detect such losses on the DB side, due to the insufficient statistics the values for sensitivity are not presented in this work.

Similarly, preliminary simulations corresponding both loss scenarios at the MB side were performed, however it was observed that very large CPU times were required to obtain sufficient statistics. Due to the fact that for more precise simulations further details have to be added to existing FLUKA model, e.g. the magnetic fields of the magnets along the beam line, the tunnel walls, etc., the simulations were not pursued. Moreover, results on the ongoing beam dynamics related analysis of failure scenarios will also help to enhance the loss scenarios.

Crosstalk The 'signal to crosstalk ratio' for a beam loss monitor is the ratio of the magnitude of the wanted signal to the magnitude of the unwanted signal. In the CLIC TBM a significant contribution to the unwanted signal could arise from the neighbouring beam. The analysis regarding the power of the cross-talk signal has to be done by considering dangerous loss scenarios, and comparing the estimated number of propagated photons produced in a fiber from the near and far beams.

However, due to the shielding effects of the neighbouring beam line and its components, the required CPU time to obtain sufficient statistics at the scoring boundary representing the fiber at the side of the far beam is substantially higher than for the boundary at the side of the near beam. Therefore, also these simulations were not pursued until a more detailed FLUKA for the TBM is available.

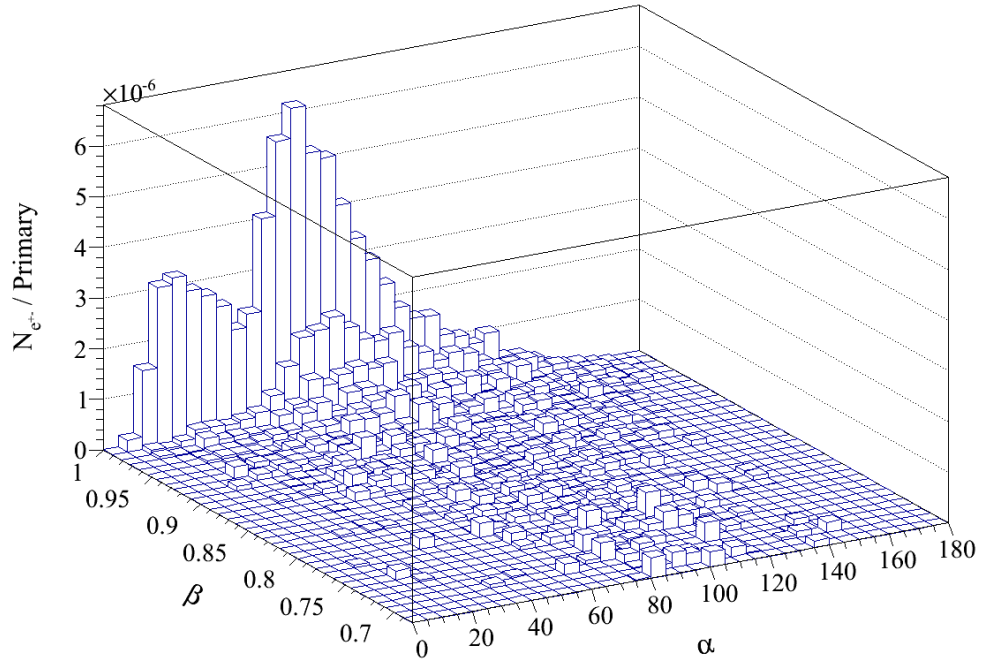


Figure 7.5: Number of e^+/e^- per one lost electron due to a destructive loss at the DB at 0.24 GeV. The numbers shown are calculated for a fiber with a diameter of $d = 365\mu m$, located at a horizontal distance of 40 cm from the beam line.

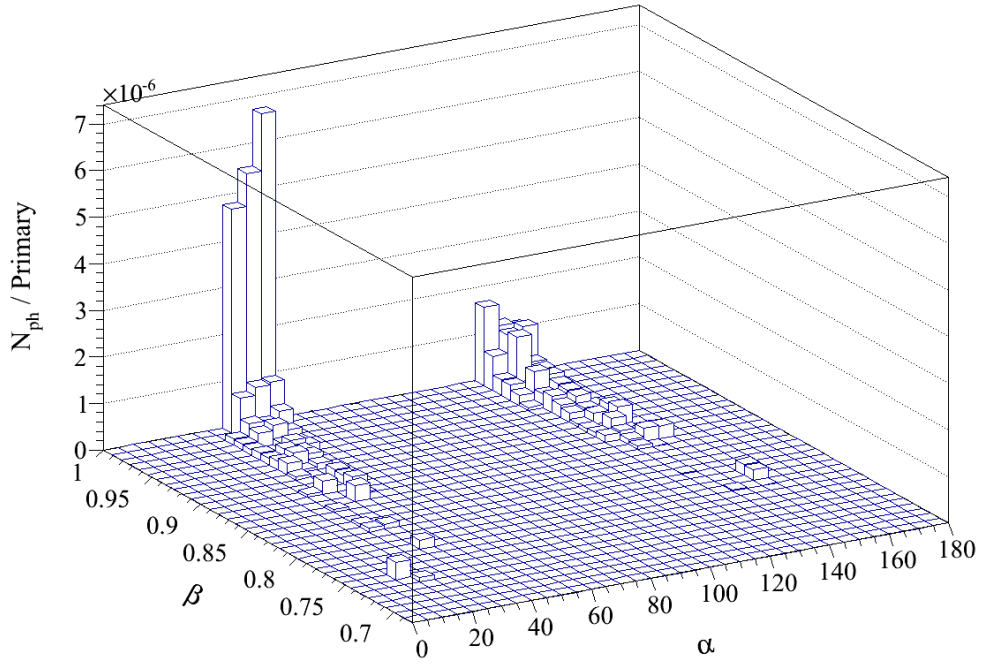


Figure 7.6: Number of trapped photons per one lost electron due to a destructive loss at the DB at 0.24 GeV. The numbers shown are calculated for a fiber with a diameter of $d = 365\mu m$, located at a horizontal distance of 40 cm from the beam line.

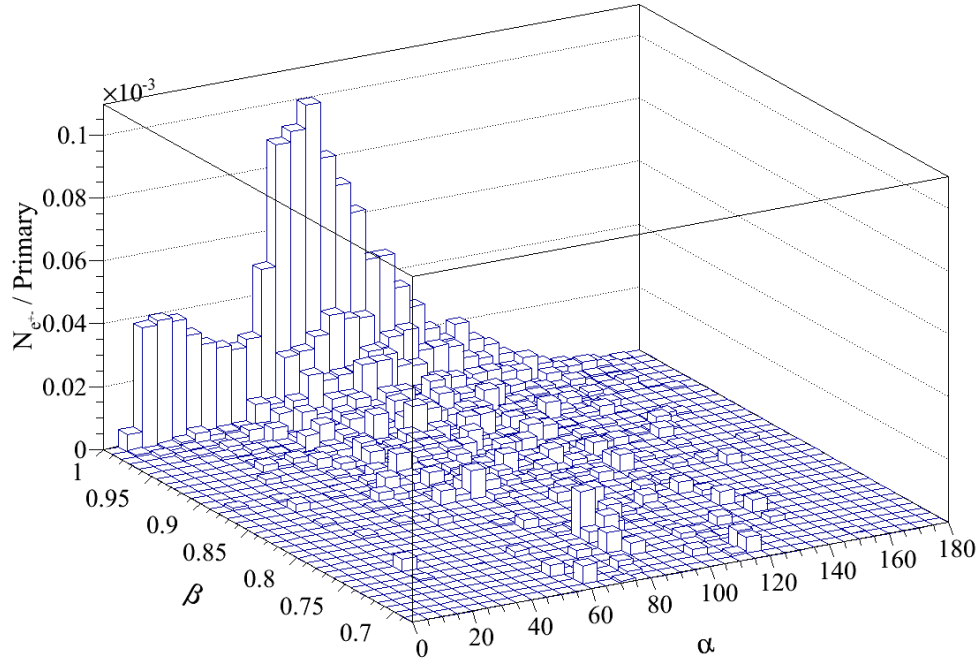


Figure 7.7: Number of e^+/e^- per one lost electron due to a destructive loss at the DB at 2.4 GeV. The numbers shown are calculated for a fiber with a diameter of $d = 365\mu m$, located at a horizontal distance of 40 cm from the beam line.

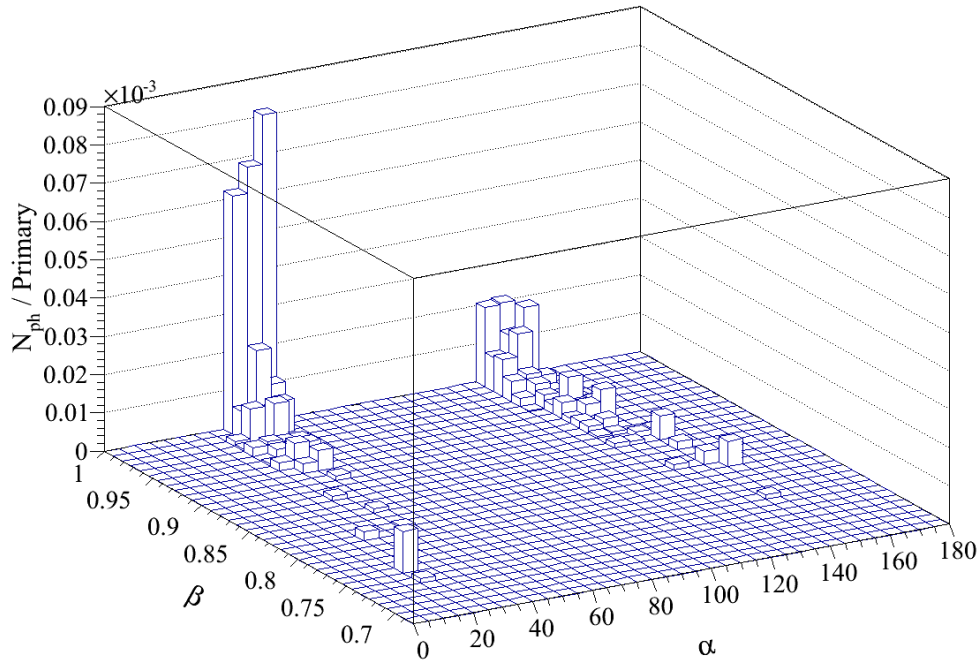


Figure 7.8: Number of trapped photons per one lost electron due to a destructive loss at the DB at 2.4 GeV. The numbers shown are calculated for a fiber with a diameter of $d = 365\mu m$, located at a horizontal distance of 40 cm from the beam line.

7.3 Longitudinal Resolution for Single-bunch Losses

The longitudinal position resolution limits for a single lost bunch are studied by analysing the signal resulting from different loss scenarios.

In particular, the distributions of the longitudinal photon propagation velocity and of the impact position x of the shower particles onto the fiber are considered. Furthermore, different loss locations along the fiber are analysed. For these studies, the fiber length is set to 100 m, a compromise between cost effectiveness on the one hand, and limits due to attenuation and dispersion effects on the other. The signal dispersion can be deduced from the photon arrival time distribution at either end of the fiber. It is derived according to the following considerations:

- Using the model discussed in Section 5.2.1, the photon propagation velocity distribution can be calculated for particular loss scenarios. Pairs of variables (α, β) are picked according to the distribution of the simulated loss scenario (cf. Figure 7.6a or 7.8a). For each pair, a random variable b for the impact parameter is created, and the generated number of photons is calculated according to the path length L within the fiber (cf. Equations (5.9) and (5.10)). Subsequently, for each of the photons, the variables ρ and ω are randomly created, and the trapping and exit conditions in Equations (5.11), (5.14) and (5.16) are checked. If the conditions are met, the longitudinal propagation angle ψ is computed. The cosine of ψ is the ratio between the length of the shortest possible photon propagation path, parallel to the fiber axis, and the length of the path taken by the photon in question. Consequently, $\cos \psi$ is also the ratio between the highest possible photon propagation velocity, $v_{prop,max} = c/n_{co}$, and the propagation velocity, $v_{prop,j}$, of a photon with a particular ψ_j :

$$v_{prop,j} = \frac{c \cdot \cos \psi_j}{n_{co}} = v_{prop,max} \cdot \cos \psi_j \quad (7.6)$$

- A simplified geometry (cf. Figure 7.9) was used to model the impact of the beam loss shower onto the fiber. The impact position x in relation to the actual beam loss position x_0 is determined by the distance d between the beam line and the fiber, and the impact angle α by $x = d/\tan \alpha$. Until the charged particle crosses the fiber, it travels a distance $L = d/|\sin \alpha|$ with a velocity $\beta \cdot c$. After the Cherenkov photons are created at the position $x_0 + x$ within the fiber, they travel each with a velocity $c/n_{co} \cdot \cos \psi_j$, corresponding to their longitudinal propagation angle ψ_j .

For the arrival time $\Delta t_{i,j}$ of a Cherenkov photon j , with respect to a trigger signal indicating the bunch passing the upstream fiber end, generated by a shower particle i , two cases have to be distinguished:

1. $\cos \psi_j$ is positive, thus the produced photon travels to the downstream fiber end.

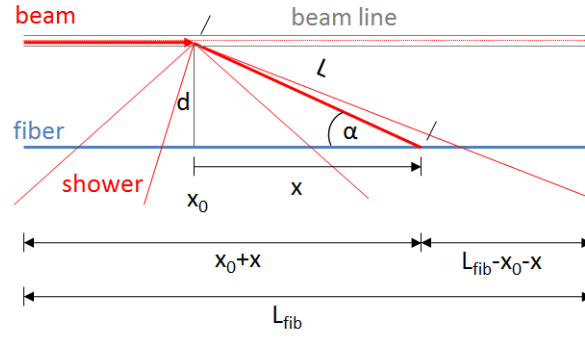


Figure 7.9: Schematic drawing of the geometry of the beam loss shower impact onto a fiber parallel to the beam line.

The arrival time $\Delta t_{d,i,j}$ is given by:

$$\begin{aligned}\Delta t_{d,i,j} &\approx \frac{x_0}{c} + \frac{d}{|\sin \alpha_i| \beta_i c} + \frac{(L_{fib} - (x_0 + d/\tan \alpha_i))}{c/n_{co} \cos \psi_j} = \\ &= \frac{x_0}{c} + \frac{L_i}{\beta_i c} + \frac{(L_{fib} - (x_0 + x_i))}{c/n_{co} \cos \psi_j}\end{aligned}\quad (7.7)$$

2. $\cos \psi_j$ is negative, thus the produced photon travels to the upstream fiber end.

The arrival time $\Delta t_{u,i,j}$ can be expressed as:

$$\Delta t_{u,i,j} \approx \frac{x_0}{c} + \frac{L_i}{\beta_i c} + \frac{(x_0 + x_i)}{c/n_{co} |\cos \psi_j|}\quad (7.8)$$

Figure 7.10 presents the photon propagation velocity distribution for a destructive loss at the DB at 2.4 GeV. Like in Section 5.2.1.7, a positive velocity represents photons propagating to the downstream fiber end, whereas a negative velocity represents photons traveling to the upstream end. The enveloping curve shows the distribution for all trapped photons. The cyan line shows the distribution of the photons that are trapped and later exit the fiber at the respective end face, whereas the magenta line shows the distribution for photons that are trapped and exit the fiber within the nominal exit cone. It shows that more photons propagate to the forward fiber end. This is a consequence of the spatial asymmetry of the loss shower for this loss scenario (see Figure 7.7a). Subject to the correct normalization, the integral over the magenta curve in Figure 7.10 over the region where $v_{prop} > 0$ is directly comparable to the integral over the distribution presented in Figure 7.8a over the region where $\alpha < 90^\circ$. In the same way, calculations can be performed for photons traveling to the backward fiber end.

As explained in Section 5.2.1.2, the condition for an exit of the photon at the fiber end face, as well as the condition for the exit within the nominal exit cone, is defined by the longitudinal propagation angle ψ . Since the longitudinal propagation velocity of a photon is also defined by ψ (cf. Equation (7.6)), these conditions directly imply constraints on the velocities of the photons for both cases. Consequently, it follows from Equations (5.14) and

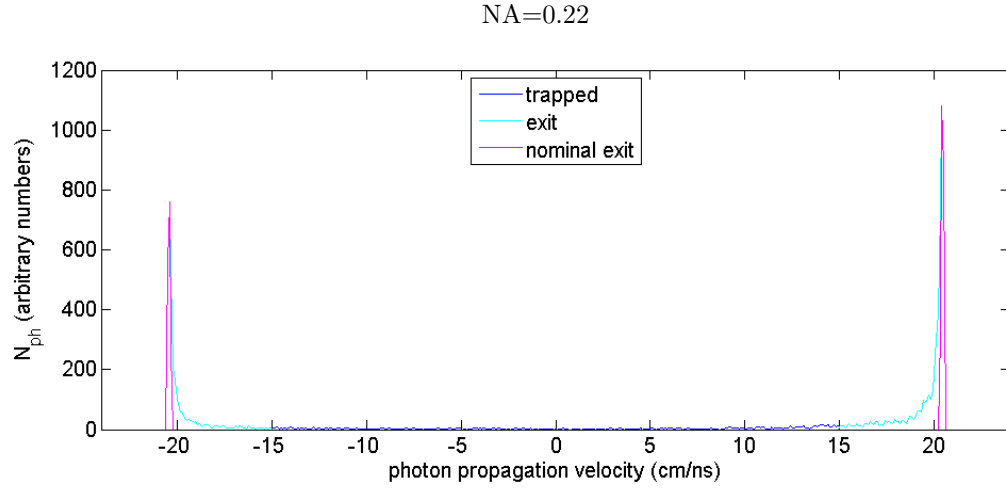


Figure 7.10: Photon propagation velocity distribution for a simulated destructive loss at the DB at 2.4 GeV, for a fiber with $d = 365 \mu\text{m}$ and $\text{NA} = 0.22$. Photons with positive velocity travel to the downstream fiber end, whereas photons with negative velocity propagate to the upstream end. The enveloping line shows the distribution for all trapped photons. The cyan line shows the distribution for the photons that are trapped and later exit the fiber at the respective end face. The magenta curve shows the according distribution for photons that are trapped and exit the fiber within the nominal exit cone.

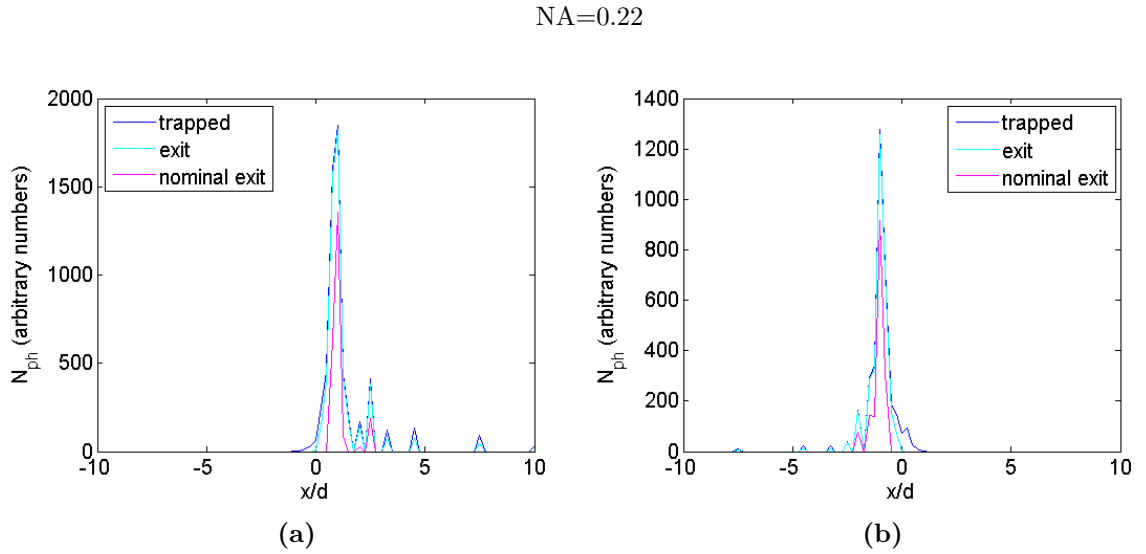


Figure 7.11: Distribution of the position of photon generation, normalized to the distance d between fiber and beam line. The x -value zero corresponds to the actual longitudinal loss position x_0 along the fiber. The outer, dark blue line shows the distribution of the position x where trapped photons are generated. The cyan line shows the distribution of the position where photons are produced that are trapped and later exit the fiber. The inner, magenta curve shows the according distribution for photons that are trapped and exit the fiber within the nominal exit cone. **(a)** Distribution for photons traveling to the forward fiber end, and **(b)** traveling to the backward end.

NA=0.22

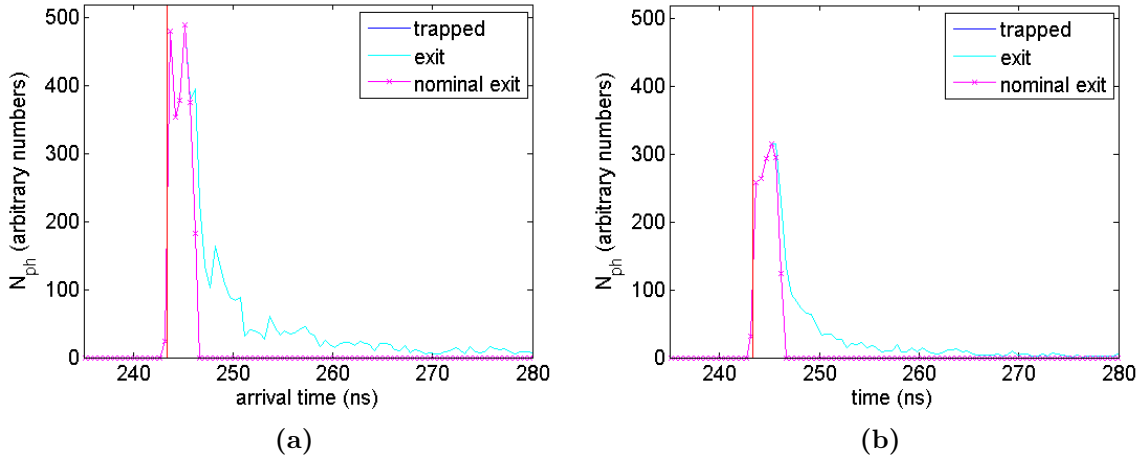


Figure 7.12: Photon arrival time distribution resulting for a simulated destructive loss at the DB at 2.4 GeV, for a fiber with $d = 365 \mu\text{m}$ and $\text{NA} = 0.22$. The loss position, x_0 , is set to $L_{fib}/2 = 50 \text{ m}$ and the distance between fiber and beam line is set to 40 cm. The enveloping line shows the distribution for all trapped photons. The cyan line shows the distribution for the photons that are trapped and later exit the fiber at the respective end face. The magenta curve shows the distribution for photons that are trapped and exit the fiber within the nominal exit cone. The period between the data points, indicated by a \times , is 0.5 ns. **(a)** Arrival time distribution at the forward fiber end. **(b)** Arrival time distribution at the backward fiber end.

NA=0.37

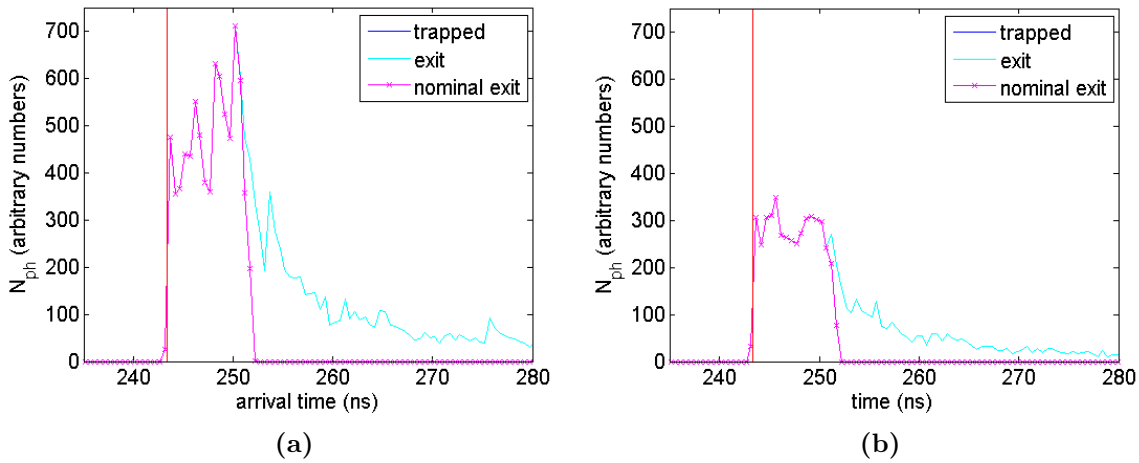


Figure 7.13: Photon arrival time distribution resulting for a simulated destructive loss at the DB at 2.4 GeV, for a fiber with $d = 365 \mu\text{m}$ and $\text{NA} = 0.37$. **(a)** Arrival time distribution at the forward fiber end. **(b)** Arrival time distribution at the backward fiber end.

For a comprehensive explanation of the graphs, see Figure 7.12

(5.16) that the propagation velocity limits for the photons which are able to exit the fiber is given by

$$\frac{c}{n_{co}} \geq v_{prop,e} \geq \frac{c}{n_{co}} \cdot \cos \psi_{c,e} \quad (7.9)$$

and for the photons exiting the fiber within the nominal exit cone can be expressed as:

$$\frac{c}{n_{co}} \geq v_{prop,e,nom} \geq \frac{c}{n_{co}} \cdot \cos \psi_{c,e,nom} = \frac{c}{n_{co}} \cdot \frac{n_{cl}}{n_{co}} = \frac{c}{n_{co}} \cdot \sqrt{1 - \frac{NA^2}{n_{co}^2}}. \quad (7.10)$$

Constraints on the propagation velocity have a direct impact on the dispersion. Hence, the equation above shows that the velocity range and the dispersion for 'nominal exit' photons can be reduced by choosing a fiber with a low numerical aperture.

Figure 7.11 shows the distribution of the position of creation of trapped photons, normalized to the distance between fiber and beam line. The three curves shown represent the three cases trapped (dark blue), trapped and exit (cyan), and trapped and exit within the nominal exit cone (magenta). The value zero on the x-axis corresponds to the actual loss location x_0 along the fiber.

As a direct result of the limited angular acceptance of the trapping process of produced Cherenkov light within a fiber as discussed in Section 5.2.1.2, the range along the fiber in which the generated light is trapped is also limited. This limit is, as the angular one, most significant for the photons exiting the fiber within the nominal exit cone. The maxima of the distributions in Figure 7.11a and 7.11b are found at $x/d \approx 1$ and $x/d \approx -1$, respectively. This is a consequence of the fact that the loss shower for the most part consists of particles with $\beta \approx 1$, for which $\theta_C \approx 45^\circ$ (in quartz), and that α is $\approx 45^\circ$ when $x/d \approx 1$. The spiky form of the curves is mainly a result of the fact that the variable pairs (α, β) are picked from a binned distribution (cf. Figure 7.5a).

Photon arrival time distribution

The Cherenkov photon arrival time distributions at either fiber end provide information about the intrinsic signal dispersion and accordingly the achievable position resolution. For a precise relation between the timing information of the signal and the position of the generation of this signal, a distinctive part of the signal has to be related to a particular velocity. One option is to utilize the velocity $v_{prop,max} = c/n_{co}$, since Figure 7.10 indicates that the major part of the photons is traveling along the fiber with a velocity close to the maximum possible. The part of the signal to correlate this velocity to would be its rising edge.

The drawback of this approach is that it is assumed that the photons are created at x_0 , which is not true in practice. As previously discussed, a particular charged particle covers the distance L_i before crossing the fiber and creating photons at position x . The corresponding arrival time of the photons is given by Equation (7.7) or (7.8). Whereas the velocity of the charged particle ranges from $\beta_{th} \cdot c \approx 2/3 \cdot c$ up to $\approx c$, the photon propagation velocity theoretically ranges from zero up to $v_{prop,max} = c/n_{co} \approx 2/3 \cdot c$. On the other hand, the distance L is larger than the distance x , which is inherent to the approach. In particular for $\alpha \approx 45^\circ$, the angle at which most photons are produced in quartz fibers (cf. Figure 7.11),

$L \approx 1.41 \cdot x$ and the longer distance nearly exactly compensates for the higher velocity range. As a result, even though the validity of the correlation between the rising edge of the signal and the velocity $v_{prop,max} = c/n_{co}$ as stated above is not obvious, it may provide a sufficient resolution. Therefore, the validity of the method is tested for all simulated loss scenarios by a variation of:

- The loss position, x_0 , along the fiber.
- The distance, d , between fiber and beam line.
- The numerical aperture, NA, of the fiber.

Assuming the correlation is valid, the expected arrival time Δt_0 for a loss at position x_0 , is

$$\Delta t_0 = \frac{x_0}{v_{prop,max}} = \frac{x_0 n_{co}}{c} \quad (7.11)$$

Moreover, an intrinsic limit on the resolution with this approach would be formed by the total signal rise time Δt_{rise} , which is mainly caused by

- the variation in the positions of photon generation due to the spatial shower distribution and
- the variation of the photon propagation velocities.

Figure 7.12 shows the arrival time distributions at both fiber ends for an accidental loss at the DB at 2.4 GeV and a fiber with $d = 365 \mu m$ and $NA = 0.22$. The loss location is set to $L_{fib}/2 = 50 m$ and the distance between fiber and beam line is set to 40 cm. The colors of the curves represent the same cases as in previously discussed figures, i.e. the magenta curve shows the distribution for the photons exiting the fiber within the nominal exit cone. The enveloping graph represents the distribution for all trapped photons. As for the graphs for the position of photon creation, the spiky form of the curve is mainly a result of the fact that the variable pairs (α, β) are picked from a binned distribution.

The additional vertical red line drawn in the graphs in Figure 7.12 signifies the expected arrival time Δt_0 for this example. It clearly lies within the rising edge of the signal for both the distributions for the downstream and upstream fiber end. Furthermore, the total rise time is less than 1 ns. Recalling Equations (7.4) and (7.5), this implies a potential resolution of better than 65 cm for the downstream fiber end and better than 12 cm for the upstream end.

Similar to Figure 7.12, Figure 7.13 presents the arrival time distribution at both fiber ends, the only difference is that the numerical aperture of the fiber is changed to $NA = 0.37$. Due to the larger NA, the distribution is wider and the number of arriving photons is larger. Despite the broadening of the distribution, the rise time Δt_{rise} is still less than 1 ns, and the red line depicting the expected Δt_0 still lies within it. Therefore, the resolution does not change compared to a fiber with $NA = 0.22$.

As mentioned above, further studies on this loss scenario were performed varying x_0 and d . It was observed, that the assumed arrival time Δt_0 lies within the rising edge of the signal for

all loss positions x_0 within the considered fiber length (100 m). The same result was found for the variation of d in the range between zero and 2 m. Furthermore, the signal rise time Δt_{rise} never exceeded 1 ns for all cases.

Similar studies were carried out for the accidental loss at the DB at 0.24 GeV. Due to the fact that the arrival time distribution is a result of the shower distribution, and the loss distribution as a function of α and β is, except the bin contents, very similar for the accidental loss scenarios for 0.24 and 2.4 GeV (compare Figure 7.5a and 7.7a), also the arrival time distributions is very similar. As a consequence, the potential resolution does not change compared to the loss scenario for 2.4 GeV.

Summarizing the performed studies for the accidental loss scenarios at the DB, the potential resolution for the loss location is better than 65 cm for the downstream fiber end and better than 12 cm for the upstream end. In practice, the resolution will be further limited by the sampling frequency of the digitizer (cf. Equations (7.1) and (7.2)). On the other hand, since the rise time of the signal lies in the range between 0.5 and 1 ns for all studied cases, a sampling frequency higher than 2 GS/s will provide no benefit.

For the MB loss scenarios similar studies have to be carried out. However, as discussed in the previous section, for these cases there are currently no simulation results with sufficient statistics for the FLUKA model including the dedicated binning system available. Despite the results for the DB, caution has to be exercised. The functioning of the method discussed above is, after all, subject to the spatial distribution of the shower particles. Would the distribution, e.g. conceivably at very high beam energies, not, or only marginally contain shower particles in the ranges $35^\circ \leq \alpha \leq 60^\circ$ or $120^\circ \leq \alpha \leq 145^\circ$, there would be only few photons produced with a propagation velocity greater than $c/n_{co} \cdot \cos \psi_{c,e,nom}$, the minimum propagation velocity of photons exiting the fiber within the nominal exit cone. As a result, the rising edge of the signal could no longer be related to $v_{prop,max}$.

7.4 Longitudinal Resolution for Multi-bunch Losses

For multi-bunch trains, there is an ambiguity for signals resulting from different loss locations and loss times. For example, the signal from losses of a small fraction of each bunch of the entire train at a single position and that from a portion of the bunches at more than one location can be similar. This leads to a limitation on the attainable longitudinal resolution. A graphical representation was developed [53] to visualize and to graphically analyse specific loss scenarios. Three kinds of likely loss scenarios can be distinguished for the CLIC main linac [54]:

1. A punctual loss due to an obstruction in the beam line.

Such an obstruction affects all bunches equally and the loss is homogeneous along the train. Figure 7.14a shows the space-time diagram representing the loss scenario. A bunch train with duration τ_{train} (blue lines) travels the distance L_{fib} along the beam

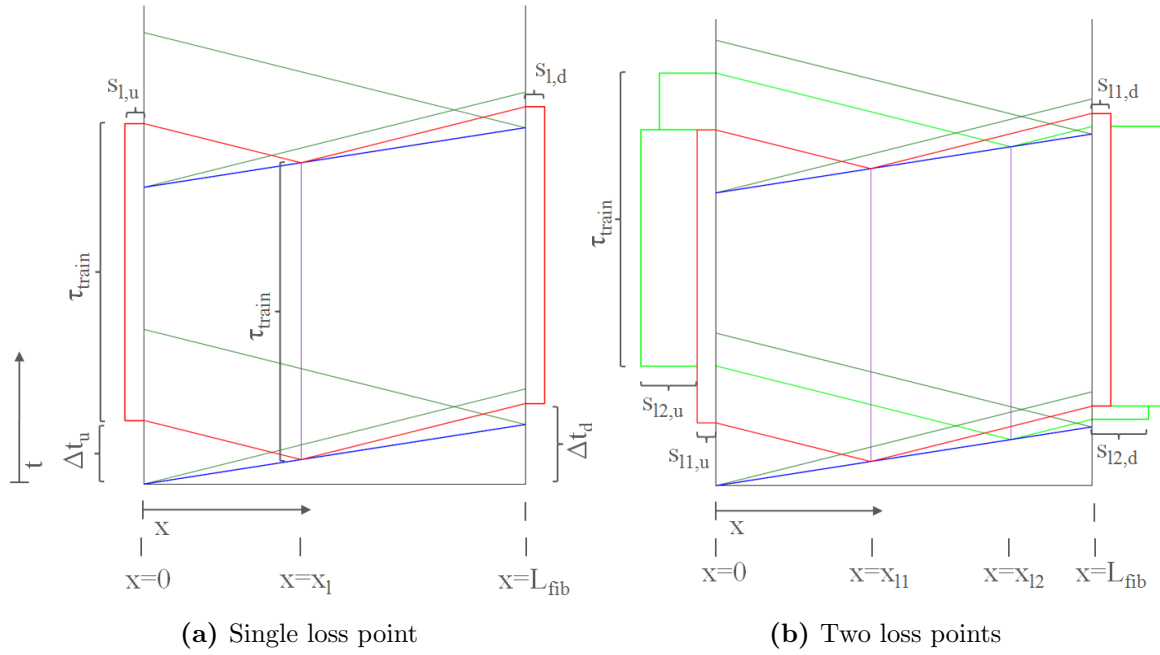


Figure 7.14: (a) Space-time diagram of a bunch train (blue lines) of length τ_{train} propagating along the beam line with a punctual loss at position $x = x_l$. The expected signal shape at the upstream and downstream fiber end is illustrated at left and right side, respectively, of the time axis. (b) Space-time diagram of a bunch train propagating along the beam line with two punctual losses at $x = x_{l1}$ and $x = x_{l2}$ [53]. For both presented diagrams, the bunch train duration, τ_{train} , is assumed to be approximately five times the traveling time of the train along the length of the fiber. This is the case for a MB bunch train ($\tau_{train} = 156$ ns) and $L_{fib} = 100$ m. Detailed explanation is given in the text.

line and experiences a loss at the position $x = x_l$. The loss signal, $s_l(t)$, is expected to be of an approximately rectangular form, with the same duration as the bunch train, τ_{train} , itself. The position of the loss can be determined by measuring the time, Δt_l , of the onset of the loss signal at either end of the fiber.

The achievable position resolution depends on the signal rise time. As discussed in the previous section, at the DB this is below 1 ns for single bunches and therefore a resolution of < 65 cm is expected for the drive beam line. Future studies on the single bunch resolution will determine the achievable resolution for bunch trains in the MB linac.

2. Several punctual losses due to obstructions in the beam line.

If the amplitude of the loss signal is approximately constant for the entire bunch train, it is also possible to resolve more than one loss position. This is illustrated in Figure 7.14b. It shows a space-time diagram of a bunch train (blue lines), traveling along the beam line, that interferes with two obstructions at the locations $x = x_{l1}$ and $x = x_{l2}$. The generated loss signals s_{l1} and s_{l2} propagate both to the downstream and the upstream end of the fiber, where they are detected as $s_{l1,u}(t)$ (red) and $s_{l2,u}(t)$ (light green) or $s_{l1,d}(t)$ and $s_{l2,d}(t)$, respectively.

At the upstream end, the leading edge of $s_{l1,u}(t)$ arrives at

$$t = \Delta t_{l1,u} \approx \frac{x_{l1}}{c} + \frac{x_{l1}}{c/n_{co}} = \frac{x_{l1}}{c}(1 + n_{co}) \quad (7.12)$$

and that of $s_{l2,u}(t)$ arrives at

$$t = \Delta t_{l2,u} \approx \frac{x_{l2}}{c}(1 + n_{co}) \quad (7.13)$$

The total loss signal is given by

$$s_{l,u}(t) = s_{l1,u}(t) + s_{l2,u}(t) \quad (7.14)$$

The time interval between the leading edges, $\Delta t_{l,u}$, can be expressed as

$$\Delta t_{l,u} = \Delta t_{l2,u} - \Delta t_{l1,u} \approx \frac{(x_{l2} - x_{l1})}{c}(1 + n_{co}). \quad (7.15)$$

$s_{l,u}(t)$ has rising edges at $t = \Delta t_{l1,u}$ and $t = \Delta t_{l2,u}$ and falling edges at $t = \Delta t_{l1,u} + \tau_{train}$ and $t = \Delta t_{l2,u} + \tau_{train}$. Therefore, by means of detecting the edges and a recognition of two edges, each with an interval of $\Delta t = \tau_{train}$, the different loss locations are resolvable. The achievable position resolution depends on the signal rise time and on the prominence of the edges within the signal amplitude. In theory, the resolution of each loss location is only limited by the possible resolution for single bunch losses. Consequently, a resolution of $\lesssim 65$ cm can be expected for the drive beam line.

The time structure of the signal resulting from losses of bunch trains at multiple positions is different for the downstream end and the upstream end of the fiber. At the downstream end, the leading edge of $s_{l1,d}(t)$ arrives at

$$t = \Delta t_{l1,d} \approx \frac{x_{l1}}{c} + \frac{L_{fib} - x_{l1}}{c/n_{co}} \quad (7.16)$$

and that of $s_{l2,d}(t)$ arrives at

$$t = \Delta t_{l2,d} \approx \frac{x_{l1}}{c} + \frac{L_{fib} - x_{l2}}{c/n_{co}} \quad (7.17)$$

The time interval between the leading edges of the downstream signal, Δt_d , are then given by

$$\Delta t_d = \Delta t_{l2,d} - \Delta t_{l1,d} \approx \frac{(x_{l2} - x_{l1})}{c}(1 - n_{co}). \quad (7.18)$$

Due to the fact that n_{co} is always greater than 1 for a quartz fiber, Δt_d is negative. Therefore at the downstream end, as also can be seen in Figure 7.14b, the Cherenkov loss signal, generated at a position $x_{l2} > x_{l1}$ arrives before a loss signal generated at x_{l1} . These results are similar to the ones obtained in Equations (7.1) and (7.2).

3. Losses along the train due to multi-bunch effects that build up in the linac itself.

Examples are long-range wake fields [55] or resistive-wall wake fields [56]. These effects develop along the bunch train and mainly affect its tail. The instabilities propagate

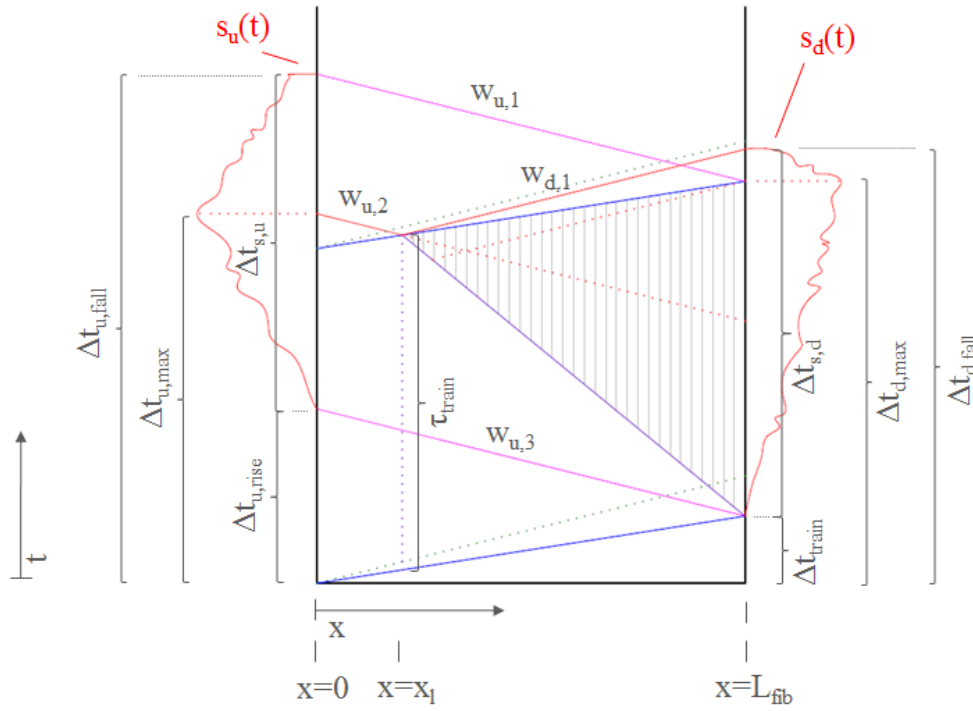


Figure 7.15: Space-time diagram of the generic loss scenario [54] for multi-bunch instabilities [53]. The expected signal shape at the upstream and downstream fiber end is illustrated at left and right side, respectively, of the time axis. For the presented case, the bunch train duration, τ_{train} , is assumed to be approximately five times the traveling time of the train along the length of the fiber. This is the case for a MB bunch train ($\tau_{train} = 156$ ns) and $L_{fib} = 100$ m. Detailed explanation is given in the text.

along the train and grow in transverse amplitude. Additional effects evolve due to the non uniform deceleration of all beam particles along the train in the drive beam decelerator. In general, the shape of the loss signal cannot be estimated a priori and consequently a detailed resolution is not possible.

Many scenarios are possible, so a generic case was considered to analyse the scheme. For the generic case, it is assumed that the instability causing visible losses starts at $x = x_l = L_{fib}/5$, with the last bunch of the train only. The unstable part then increases linearly along the bunch train, with the full train being unstable and experiencing losses at $x = L_{fib}$.

Figure 7.15 shows a space-time diagram of the generic loss scenario. The loss generates the total loss signals $s_u(t)$ at the upstream fiber end and $s_d(t)$ at the downstream end. The rising edge of the signal at the downstream fiber end arrives at

$$t = \Delta t_{d,rise} \approx \Delta t_{train} = \frac{L_{fib}}{c} \quad (7.19)$$

and the falling edge at

$$t = \Delta t_{d,fall} \approx \frac{x_l}{c} + \tau_{train} + \frac{L_{fib} - x_l}{c/n_{co}}. \quad (7.20)$$

Accordingly, at the upstream fiber end, the rising edge of the total signal arrives at

$$t = \Delta t_{u,rise} \approx \frac{L_{fib}}{c}(1 + n_{co}) \quad (7.21)$$

and the falling edge at

$$t = \Delta t_{u,fall} \approx \frac{L_{fib}}{c}(1 + n_{co}) + \tau_{train} \quad (7.22)$$

The upstream and downstream loss signals of the first lost bunch at position x_l have the world lines $w_{u,2}$ and $w_{d,1}$, respectively, in the diagram. The corresponding arrival times are

$$t = \Delta t_{d,l} \approx \frac{x_l}{c} + \tau_{train} + \frac{L_{fib} - x_l}{c/n_{co}} \quad (7.23)$$

and

$$t = \Delta t_{u,l} \approx \tau_{train} + \frac{x_l}{c}(1 + n_{co}) \quad (7.24)$$

At the upstream fiber end, this signal timewise lies within the edges of the total signal and cannot be detected separately. However, at the downstream fiber end, the signal arrival time $\Delta t_{u,l}$ corresponds to the the arrival time of the falling edge of the total signal, $\Delta t_{d,fall}$. The actual loss position can be calculated by intersecting the world line $w_{d,1}$ with the world line of the last bunch of the train (see Figure 7.15). The achievable position resolution depends on the fall time of the signal. This, in turn, depends on the fall time of the employed photodetector and the dispersion of the single bunches and has to be studies for a particular case each.

Furthermore, the position where the last bunch of the train initially experiences a visible loss, can be determined by the arrival time, $\Delta t_{u,max}$, of the maximum of the upstream signal. By measuring $\Delta t_{u,max}$ the world line $w_{u,2}$ is defined. Consequently, the loss position x_l can be found by an intersection of $w_{u,2}$ with the world line of the last bunch. However, due to the fact that the total signal is a convolution of all single bunch loss signals, the maximum will be smeared out to an extend that does not allow the resolution of a downstream measurement.

Further scenarios that can be considered are:

- Only a fraction of the bunch train, Δt_{train} , is visibly unstable at $x = L_{fib}$.

This fraction can be deduced by the arrival times of the rising edges of the total signals at either fiber end.

For the downstream end it follows that

$$\Delta t_{train} \approx \frac{\Delta t_{train} + \tau_{train} - \Delta t_{d,rise}}{\tau_{train}} \quad (7.25)$$

and accordingly for the upstream end

$$\Delta t_{train} \approx \frac{\Delta t_{u,fall} - \Delta t_{u,rise}}{\tau_{train}} \quad (7.26)$$

The determination of Δ_{train} by a measurement at the upstream fiber end is only reasonable as long as

$$\Delta_{train} > \frac{\Delta t_{train} + \tau_{train} - \left(\frac{x}{c} + \tau_{train} - \frac{L_{fib} - x}{c/n_{co}}\right)}{\tau_{train}} \quad (7.27)$$

If the condition above is not met, the arrival time of the loss signal generated by the last bunch which experiences losses does no longer correspond to the arrival time, $t = \Delta t_{u, rise}$, of the rising edge of the total loss signal. Therefore, a measurement at the downstream end has to be preferred.

- The full train is unstable and experiencing losses at a position $x < L_{fib}$.

This position x can only be determined from the arrival time of the rising edge of the total signal at the upstream end of the fiber. The corresponding world line has to be intersected with the world line of the first bunch of the train. The possible longitudinal resolution is < 65 cm.

Beyond the potentially precise measurements of the loss scenarios discussed above, an analysis of the signal only fiber by fiber, can give a first insight into the behaviour of the beam. Furthermore, other signals, like the transverse position of the bunches, will give additional information. The BLM system first serves as a trigger for protective actions and the total length of the fiber offers a first raw estimate for the loss location.

For example, for the CLIC main linac, the fiber length is envisaged to be 100 m or shorter. 100 m corresponds to $\approx 5\%$ of the total length of the main beam linac (21.02 km) and $\approx 11\%$ of the one drive beam decelerator (876 m). Whereas for the the main beam it has been evaluated [54] that this resolution is in principle sufficient, for the drive beam it is not. A better resolution can be obtained utilizing the previously explained methods (in items 1. - 3.). Moreover, as it is hardly possible to resolve the train profile at a bunch-to-bunch level, it is proposed to add a individual short BLMs with high time resolution (≈ 1 ns) in each fiber sector.

8 Conclusion and Outlook

The purpose of this work was to study the feasibility of Cherenkov fibers for the Beam Loss Monitoring system along the CLIC Two Beam Modules. In order to attain this goal different investigations have been performed.

Model - The work of pre-existing studies was extended to a model that provides a tool to calculate the number of photons reaching the photodetector at the end of the fiber, per crossing charged particle, and as a function of various properties of the fiber and the crossing particle. Moreover, it allows to calculate the longitudinal propagation velocity of every photon coupled into the fiber.

Due to the directionality of the Cherenkov effect and the angular acceptance of an optical fiber, the probability to trap the produced Cherenkov photons within the fiber is strongly dependent on the angle between the crossing particle and the fiber axis.

The result is a limited, angle-dependent response of Cherenkov fibers to shower particles. The acceptance range is approximately situated symmetrically around the Cherenkov emission angle and its width scales with the numerical aperture of the fiber. The directionality of the Cherenkov effect also causes a dependency of the photon propagation velocity distribution on the incident angle of the charged particles.

Both these dependencies on the incident angle of the charged particle lead to different signals for different spacial loss shower distributions. With regard to the angular acceptance, fibers with a larger NA are preferable. However, for fibers with a large NA the spread in the photon propagation velocities increases, causing a dispersion of the signal and therefore a worse longitudinal resolution.

The fundamental influence the wavelength dependency of attenuation on the Cherenkov light spectrum was analysed by considering Rayleigh scattering. It was shown that a focus on the detection of higher-wavelengths ($\gtrsim 550$ nm) would lead to less variation in the detected Cherenkov light yield for different fiber lengths (or different positions of signal creation), due to the lower influence of attenuation effects in this spectral range. On the other hand, the light yield would be substantially lower in this range, and a compensation by larger fiber diameters could be necessary. For particular fibers, the analysis can be improved by utilizing the nominal attenuation as a function of the wavelength.

The model would also allow to compute the angular distributions of photons exiting the fiber. With these distributions, the coupling efficiency between the fiber and the photodetector could be studied in detail.

Verification Measurements - The predictions of the model for the functional dependency of the Cherenkov light yield on the fiber diameter and the angle between the fiber axis and the trajectories of the crossing particles are experimentally verified. The measurement results are in very good agreement with the theory, not only in a relative comparison, but also in absolute values.

Application to the CLIC Two Beam Modules - The results of simulations, performed with the Monte Carlo code FLUKA [3, 4], on decisive loss scenarios in the TBM were utilized as an input for the developed model in order to estimate the magnitude and the time behaviour of the loss signals. The presented approach allows to estimate the sensitivity, dynamic range, the achievable resolution of the loss location, and the ability to distinguish losses originating from either beam of the TBM. However, due to the large CPU times required, currently only two loss scenarios for the drive beam can be presented. The simulations of the other loss scenarios will be pursued after an update of the FLUKA model for the TBM.

Longitudinal resolution for multi-bunch losses - The ambiguity for signals due to beam losses of multi-bunch trains at different loss locations and loss times generally leads to limitations on the attainable longitudinal resolution of the loss position. An analysis of the signal only fiber by fiber can give a first insight into the behaviour of the beam. Whereas it has been evaluated that the total length of the fibers (≤ 100 m) would provide a sufficient resolution of the loss location for the main beam, for the drive beam it does not. A method to graphically analyse multi-bunch beam loss scenarios is developed. By means of this method, three kinds of likely cases at the CLIC TBM are studied and their specific resolution limits, subject to a readout at the downstream or upstream fiber end, are presented.

Radiation hardness - One reason for immediate exclusion of a Cherenkov fiber BLM would be an insufficient radiation hardness of the main components. Whereas the photodetectors can be placed in shielded areas, the fibers have to withstand the harsh environment close to the accelerator for many years. Current estimates predict that the annual absorbed dose can be as high as 10^5 Gy/year. Presented tests show a radiation resistance of particular fibers up to 22 MGy. However, there can be a great difference in the radiation response, even between very similar fibers, due to the large number of influence parameters. Therefore, these tests can not be generalized and dedicated radiation hardness tests are necessary. As for the intrinsic absorption, also the effects of Radiation Induced Absorption are larger for smaller wavelengths and therefore also in this case a focus on larger wavelengths ($\gtrsim 550$ nm) would provide benefits.

Installations at CTF3 - Cherenkov fiber BLMs, among localized detectors (ACEMs), are currently under installation in CTF3, the CLIC Test Facility. In comparison with the results of the ACEMs, the Fiber-BLM measurements will provide valuable practical information about the achievable longitudinal resolution and the advantages and disadvantages of the utilization of 'downstream' photons, 'upstream' photons, or both. Moreover the suitability of SiPMs as the photodetector at the fibers can be studied in more detail.

Bibliography

- [1] B Povh, K Rith, C Scholz, and F Zetsche. *Teilchen und Kerne. Eine Einfuehrung in die physikalischen Konzepte*. Springer-Verlag GmbH, sixth edition, 2004.
- [2] K Wittenburg. Beam loss monitors, 2009. Presented at CAS - CERN Accelerator School: Course on Beam Diagnostics.
- [3] Battistoni, G and Cerutti, F and Fasso, A and Ferrari, A and Muraroi, S and Ranft, J and Roesler, S and Sala, P R. The FLUKA code: Description and benchmarking. *AIP Conf. Proc.*, 896(SLAC-REPRINT-2007-184):31–49. 19 p, 2007.
- [4] Ferrari, A and Sala, P R and Fasso, A and Ranft, J. *FLUKA: A multi-particle transport code (program version 2005)*. CERN, Geneva, 2005.
- [5] L Evans and P Bryant. LHC Machine. *Journal of Instrumentation*, 3(08):S08001, 2008.
- [6] D Brandt, H Burkhardt, M Lamont, S Myers, and J Wenninger. Accelerator physics at LEP. *Reports on Progress in Physics*, 63(6):939, 2000.
- [7] J. Hauptman. *Particle Physics Experiments at High Energy Colliders*. John Wiley & Sons, 2011.
- [8] ILC collaboration. ILC Reference Design Report. Technical Report arXiv:0712.1950, December 2007.
- [9] CLIC collaboration. A multi-TeV linear collider based on CLIC technology - CLIC Conceptual Design Report, Volume 1. Technical report, CERN, Geneva, 2012.
- [10] CLIC collaboration. <http://ctf3-tbts.web.cern.ch/ctf3-tbts/images/>.
- [11] M Jonker, EB Holzer, S Mallows, D Manglunki, G Morpurgo, T Otto, M Sapinski, F Tecker, and J Uythoven. The CLIC Machine Protection. In *IPAC proceedings*, 2010.
- [12] M Sapinski, B Dehning, EB Holzer, M Jonker, S Mallows, T Otto, and C Welsch. Requirements of CLIC Beam Loss Monitoring System. In *IPAC proceedings*, number CERN-ATS-2010-105, page 3 p, Jun 2010.
- [13] Mallows, S. Review of the Radiation Levels in the CLIC Tunnel. Presented on the CLIC TBM WG on 28 March 2012.
- [14] W K H Panofsky. The use of a long coaxial ion chamber along the accelerator. Technical Report TN-73-57, SLAC, 1963.

- [15] T N Constant, R W Zdarko, R H Simmons, and B M Bennett. LIONs at the stanford linear accelerator center. Technical Report SLAC-PUB-7691, SLAC, Stanford, CA, January 1998.
- [16] E Janata. Determination of location and intensity of radiation through detection of Cherenkov emission in optical fibers: Part 1. method and experimental. *Nuclear Instruments and Methods in Physics Research Section A: Accelerators, Spectrometers, Detectors and Associated Equipment*, 493(1):1 – 7, 2002.
- [17] T Itoga, Y Asano, and X-M Marechal. Fiber Beam Loss Monitor for the SPring-8 XFEL: A Numerical Study of its Design and Performance. 2010. 1st International Particle Accelerator Conference: IPAC'10, May 2010, Kyoto, Japan.
- [18] L Froehlich D Di Giovenale, L Catani. A read-out system for online monitoring of intensity and position of beam losses in electron linacs. *Nuclear Instruments and Methods in Physics Research Section A: Accelerators, Spectrometers, Detectors and Associated Equipment*, 665(0):33 – 39, 2011.
- [19] S Bettoni, E Adli, R Corsini, A Dabrowski, S Doeber, D Manglunki, P Skowronski, and F Tecker. Achievements in CTF3 and Commissioning status. (CERN-ATS-2009-082. CLIC-Note-785), October 2009.
- [20] B Saleh and M C Teich. *Fundamentals of Photonics; 2nd ed.* Wiley series in pure and applied optics. Wiley, New York, NY, 2007.
- [21] J M Senior. *Optical fiber communications: principles and practice.* Prentice-Hall Internat. Ser. in Optoelec. Prentice-Hall, Englewood Cliffs, NJ, 1985.
- [22] F Mitschke. *Fiber Optics: Physics and Technology.* Springer, Berlin, Heidelberg, 2010.
- [23] Dorf, R C. *The Electrical Engineering Handbook.* CRC Press, 2006.
- [24] Berghmans, F and Brichard, B and Fernandez, A F and Gusarov, A and Uffelen, M Van and Girard, S. An Introduction to Radiation Effects on Optical Components and Fiber Optic Sensors. In Wojtek J. Bock, Israel Gannot, and Stoyan Tanev, editors, *Optical Waveguide Sensing and Imaging*, NATO Science for Peace and Security Series B: Physics and Biophysics, pages 127–165. Springer Netherlands, 2008.
- [25] J Kuhnhehn. Fibre optic Sensors at Accelerators - Considerations and Pitfalls, December 2011. Presented at the 7th DITANET Topical Workshop on Beam Loss Monitoring.
- [26] Girard, S and Ouerdane, Y and Origlio, G and Marcandella, C and Boukenter, A and Richard, N and Baggio, J and Paillet, P and Cannas, M and Bisutti, J and Meunier, J-P and Boscaino, R. Radiation Effects on Silica-Based Preforms and Optical Fibers I: Experimental Study With Canonical Samples. *Nuclear Science, IEEE Transactions on*, 55(6):3473 –3482, December 2008.

- [27] F Berghmans. Ionizing Radiation Effects on Optical Components, October 2006. Presented at Optical Waveguide Sensing and Imaging in Medicine, Environment, Security and Defense.
- [28] P Gorodetzky, D Lazic, G Anzivino, E Chiavassa, A Contin, G Dellacasa, N Demarco, R de Salvo, M Gallio, P Guaita, K F Johnson, P Juillot, M Lundin, M Marino, A Musso, A Piccotti, E Scomparin, and E Vercellin. Quartz fiber calorimetry. *Nuclear Instruments and Methods in Physics Research A*, 361:161–179, 1995.
- [29] V Hagopian. Radiation Damage of Quartz Fibers. Technical Report CMS-CR-1999-002, CERN, Geneva, January 1999.
- [30] Girard, S and Marcandella, C. Transient and Steady State Radiation Responses of Solarization-Resistant Optical Fibers. *Nuclear Science, IEEE Transactions on*, 57(4):2049–2055, August 2010.
- [31] Goettmann, W and Koerfer, M and Wulf, F. Beam Profile Measurements with Optical Fiber Sensor at FLASH. In *IPAC proceedings*, 2007.
- [32] Hamamatsu Photonics K.K. Photomultiplier Tubes and Assemblies for Scintillation Counting and High Energy Physics, 2009.
- [33] Hamamatsu Photonics K.K. Photomultiplier Tubes: Basics and Applications, 2006.
- [34] W R Leo. *Techniques for nuclear and particle physics experiments: a how-to approach; 2nd ed.* Springer, Berlin, 1994.
- [35] Hamamatsu Photonics K.K. Metal Package Photomultiplier Tubes R7400 Series and Subminiature Photosensor Modules, 1998.
- [36] B Lutz. *Hadron Showers in a Highly Granular Calorimeter*. PhD thesis, UNiversitaet Hamburg, Hamburg, 2010. Presented on 31. August 2010.
- [37] <http://www.wikipedia.org/>.
- [38] P Buzhan, B Dolgoshein, A Ilyin, V Kantserov, V Kaplin, A Karakash, A Pleshko, E Popova, S Smirnov, Y Volkov. An Advanced Study of Silicon Photomultipliers. *IFCA Instrumentation Bulletin*, 23(28), 2001.
- [39] Hamamatsu Photonics K.K. MPPC - Multi-Pixel Photon Counter, technical information, 2009.
- [40] Y Musienko, February 2011. Presented at the CERN SiPM workshop.
- [41] Garutti, E. SiPM for HEP detectors. Presented on 14. March 2011.
- [42] J V Jelley. *Cherenkov radiation and its applications*. Pergamon, London, 1958.

- [43] J V Jelley. SPECIAL ARTICLE: Cerenkov radiation and its applications. *British Journal of Applied Physics*, 6:227–232, July 1955.
- [44] R Kitamura, L Pilon, and M Jonasz. Optical constants of silica glass from extreme ultraviolet to far infrared at near room temperature. *Appl. Opt.*, 46(33):8118–8133, November 2007.
- [45] N Akchurin and R Wigmans. Quartz fibers as active elements in detectors for particle physics. *Review of Scientific Instruments*, 74:2955–2972, June 2003.
- [46] S H Law, S C Fleming, N Suchowerska, and D R McKenzie. Optical fiber design and the trapping of Cerenkov radiation. *Appl. Opt.*, 45(36):9151–9159, December 2006.
- [47] S H Law, N Suchowerska, D R McKenzie, S C Fleming, and T Lin. Transmission of Cherenkov radiation in optical fibers. *Opt. Lett.*, 32(10):1205–1207, May 2007.
- [48] Y-C Wang, Y-W Shi, and H-T Jiang. Passive optical fibre sensor based on Cerenkov effect. volume 1572, pages 32–37. SPIE, 1991.
- [49] Holzer, E B and Hoorne, J van and Mallows, S. Cherenkov Fiber BLMs: Theory and Experimental. To be published.
- [50] M C Ross and D McCormick. A Coaxial Cable Beam Loss Monitor Ion Chamber System for High Power Multi-bunch Beams. 1998.
- [51] O Ganel and R Wigmans. Quartz fiber calorimetry for LHC experiments. *Nuclear Instruments and Methods in Physics Research Section A: Accelerators, Spectrometers, Detectors and Associated Equipment*, 365(1):104 – 116, 1995.
- [52] S Mallows, EB Holzer, J van Hoorne, A Mechev, and C Welsch. Requirements of a beam loss monitoring system for the CLIC two beam modules. In *IPAC proceedings*, number CERN-ATS-2011-066, Geneva, September 2011.
- [53] Holzer, E B and Hoorne, J van and Mallows, S. CLIC Cherenkov Fiber BLMs: Longitudinal Resolution for Multi-Bunch Trains. To be published.
- [54] A Latina B Jeanneret, March 2012. Private communication.
- [55] D Schulte. Multi-Bunch calculations in the CLIC Main LINAC. Technical Report CERN-ATS-2009-135. CLIC-Note-805, July 2009.
- [56] R Mutzner, G Rumolo, T Pieloni, and L Rivkin. *Multi-Bunch effect of resistive wall in the beam delivery system of the Compact Linear Collider*. PhD thesis, Lausanne, EPFL, Lausanne, 2010. Presented on 1. February 2010.